Saving Fuel for Heavy-Duty Vehicles Using Connectivity and Automation

by

Chaozhe He

A dissertation submitted in partial fulfillment
of the requirements for the degree of
Doctor of Philosophy
(Mechanical Engineering)
in the University of Michigan
2018

Doctoral Committee:

Professor A. Harvey Bell IV (Co-Chair)
Professor Gábor Orosz (Co-Chair)
Professor Necmiye Ozay
Professor Hamid Ossareh, University of Vermont
Professor Huei Peng

Chaozhe He
hchaozhe@umich.edu
ORCID iD: 0000-0002-0299-8412

To my grandfather, Prof. Zhenbang He
who always shared his bizzare ideas with me on changing the world

ACKNOWLEDGMENTS

I would like to express my upmost thanks to my advisor and mentor, Professor Gábor Orosz, who guided and supported me as I walked down the path to my doctoral degree. He invited me to the career of putting connected automated vehicles on the road, taught me solid knowledge and the academic ethics, and indulged me to explore wide range of topics in the area.

I would like to acknowledge the mentorship of all the faculties I have worked with. Thank you Professor Harvey Bell for mentoring on conducting research development in the industry. Thank you Professor Helmut Maurer for demonstrating the rigorous reasoning as a mathematician. Thank you Professor Necmiye Ozay, Professor Hamid Ossareh, and Professor Huei Peng, for all the insightful comments and constructive suggestions throughout the completion of my dissertation. Thank you Professor Christine Feak for showing me the power and fun of academic writing.

I would like to thank all my collaborators in both academia and industry. Discussions with my colleagues in Michigan, including Sergei Avedisov, Yuxiao Chen, Jin Ge, Nan Li, Ziheng Pan, Wubing Qin, Mehdi Sadeghpour, and Linjun Zhang, helped me to establish and solve research questions. Discussions with my colleagues at Navistar, Inc., including Matthew Hunkler, Teik Khoon Tan, Danial Kang, Eric Jiang, Jim Yan, and Dean Oppermann, made me understand the needs and constraints of my research from industrial perspectives.

Last but not least, I am thankful to my friends and families, especially my parents Shuguang He and Hong Xu, who always supported me unconditionally. I thank my dear wife, Yinyin Ye, who has always been supporting me with her helpful advice and positive thoughts and inputs. It is pleasant to be part of the each other's journey toward the doctoral degree.

TABLE OF CONTENTS

LIST OF FIGURES

LIST OF TABLES

LIST OF APPENDICES

LIST OF ABBREVIATIONS

CCC Connected Cruise Control

HDV Heavy-Duty Vehicles

AMT Automated Manual Transmission

AT Automatic Transmission

CAV Connected Automated Vehicle

V2V Vehicle-to-Vehicle

V2I Vehicle-to-Infrastructure

CACC Cooperative Adaptive Cruise Control

DSRC Dedicated Short-Range Communication

C-V2X Cellular Vehicle-to-Everything

RHOC Receding Horizon Optimal Control

5G Fifth Generation Of Cellular Mobile Communications

GPS Global Positioning System

PMP Pontryagin's Maximum Principle

ABSTRACT

The booming of e-commerce is placing an increasing burden on freight transport system by demanding faster and larger amount of delivery. Despite the variety in freight transport means, the dominant freight transport method is still ground transport, or specifically, transport by heavy-duty vehicles. Roughly one-third of the annual ground freight transport expense goes to fuel expenses. If fuel costs could be reduced, the finance of freight transport would be improved and may increase the transport volume without additional charge to average consumers. A further benefit of reducing fuel consumption would be the related environmental impact. The fuel consumption of the heavy-duty vehicles, despite being the minority of road vehicles, has a major influence on the whole transportation sector, which is a major contributor to greenhouse gas emissions. Thus, saving fuel for heavy-duty trucks would also reduce greenhouse gas emission, leading to environmental benefits.

For decades, researchers and engineers have been seeking to improve the fuel economy of heavy-duty vehicles by focusing on vehicles themselves, working on advancing the vehicle design in many aspects. More recently, attention has turned to improve fuel efficiency while driving in the dynamic traffic environment. Fuel savings effort may be realized due to advancements in connected and automated vehicle technologies, which provide more information for vehicle design and control. This dissertation presents state-of-the-art techniques that utilize connectivity and automation to improve the fuel economy of heavy-duty vehicles, while allowing them to stay safe in real-world traffic environments. These techniques focus on three different levels of vehicle control, and can result in significant fuel improvements at each level.

Starting at the powertrain level, a gear shift schedule design approach is proposed based on hybrid system theory. The resulting design improves fuel economy without comprising driveability. This new approach also unifies the gear shift logic design of human-driven and automated vehicles, and shows a large potential in fuel saving when enhanced with higher level connectivity and automation. With this potential in mind, at the vehicle level, a fuel-efficient predictive cruise control algorithm is presented. This mechanism takes into account road elevation, wind, and aggregated traffic information acquired via connectivity. Moreover, a systematic tool to tune the optimization parameters to prioritize different objectives is developed. While the algorithm and the tool are shown to be beneficial for heavy-duty vehicles when they are in mild traffic, such benefits may not be attainable when the traffic is dense. Thus, at the traffic level, when a heavy-duty vehicle needs to interact with surrounding vehicles in dense traffic, a connected cruise control algorithm is proposed. This algorithm utilizes beyond-line-of-sight information, acquired through vehicle-to-vehicle communication, to gain a better understanding of the surrounding traffic so that the vehicle can response to traffic in a fuel efficient way. These techniques can bring substantial fuel economy improvements when applied individually. In practice, it is important to integrate these three techniques at different levels in a safe manner, so as to acquire the overall benefits. To achieve this, a safety verification method is developed for the connected cruise control, to coordinate the algorithms at the vehicle level and the traffic level, maximizing the fuel benefits while staying safe.

CHAPTER 1

Introduction

Research is to see what everybody else has seen, and to think what nobody else has thought.

ALBERT SZENT-GYORGYI

1.1 Necessity for Fuel-efficient Freight Transport

A large percentage of freight transport is carried by heavy-duty vehicles (HDVs). According to data released in February 2015 for the 2012 commodity flow survey [2], HDVs provide around 70% of the domestic freight transport in the U.S., in terms of both value and weight (see Figure 1.1). This dominance has been consistent and, with the growing

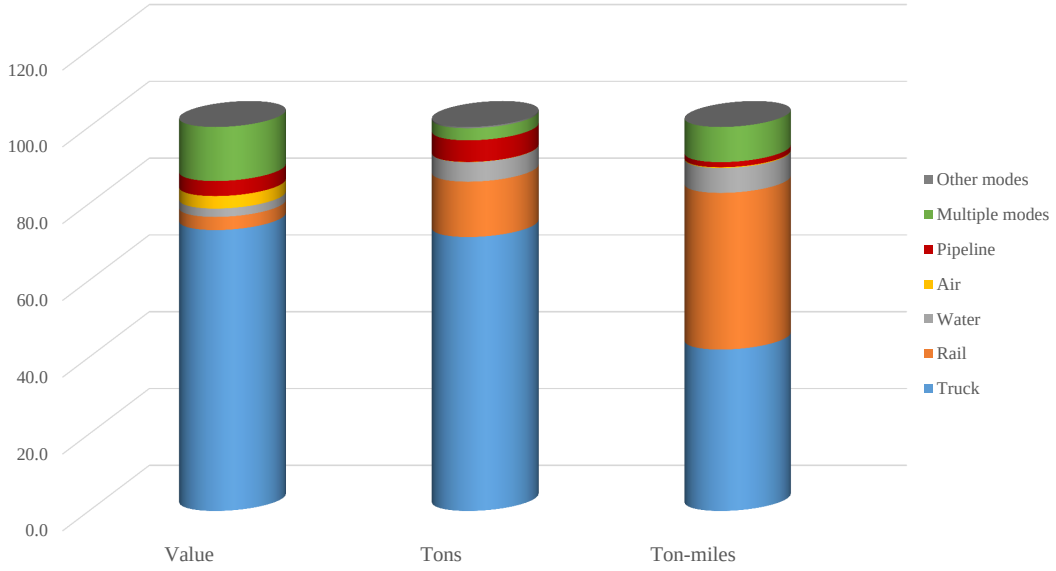

Figure 1.1: Domestic freight transport characteristics by mode of transportation. Source: 2012 commodity flow survey (released February 2015)

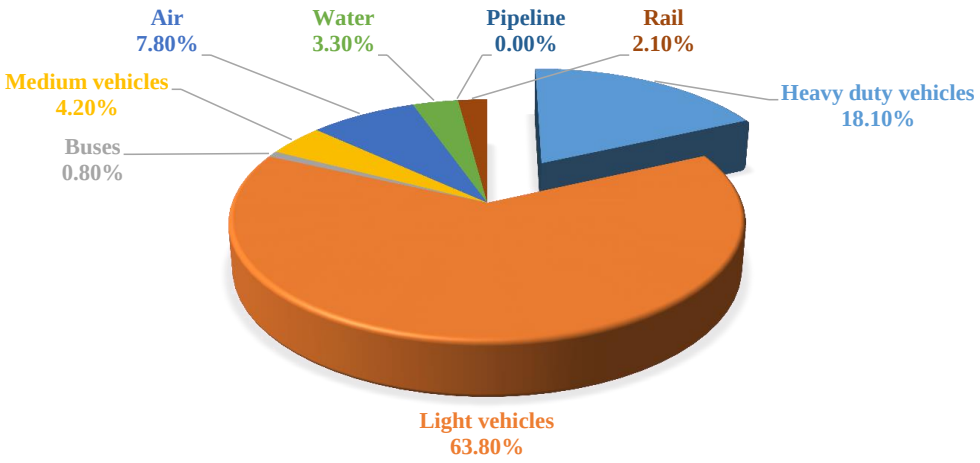

Figure 1.2: Petroleum consumption in the transportation sector. Data source: transportation energy data book edition 35, 2016

economy, is likely to increase. Given this dominance, HDV freight transport accounts for a significant portion of energy consumption. According to the U.S. Department of Energy [3], in 2016, more than 10 million HDVs were registered in the U.S. Although this amounts to less than 4% of all vehicles (249 million), HDVs are responsible for 18% of the petroleum consumption in the transportation sector (see Figure 1.2). Thus, more efficient freight transport would greatly contribute to the overall energy efficiency of the transportation sector and could yield large environmental benefits.

Looking at energy consumption from an operational perspective, fuel cost accounts for a large percentage of HDV fleet operation costs. According to a 2016 survey on trucking operational costs [4], fuel cost contributed one fourth of the annual operation cost of heavy duty trucks (see Figure 1.3). This percentage was 40% in 2012, when the fuel prices were at their highest. Given this high and fluctuating cost, improving fuel efficiency would improve the finances of the trucking industry and fleet operations.

In response to the need for better fuel efficiency, in 2009 the U.S. Department of Energy (DOE) launched the SuperTruck initiative with the goal of developing and demonstrating a 50 percent improvement in overall freight efficiency for class 8 heavy-duty trucks. The main goals of this initiative were to develop new technologies for engines and powertrains, to improve aerodynamics, to reduce weight and tire rolling resistance, and to optimize energy management systems. This initiative was led by four industry teams: Cummins/Peterbilt, Daimler, Volvo, and Navistar. In June 2016, DOE announced that all four teams have been successfully meeting or exceeding the 50 percent improvement goal, with some of the technologies close to being commercialized [5].

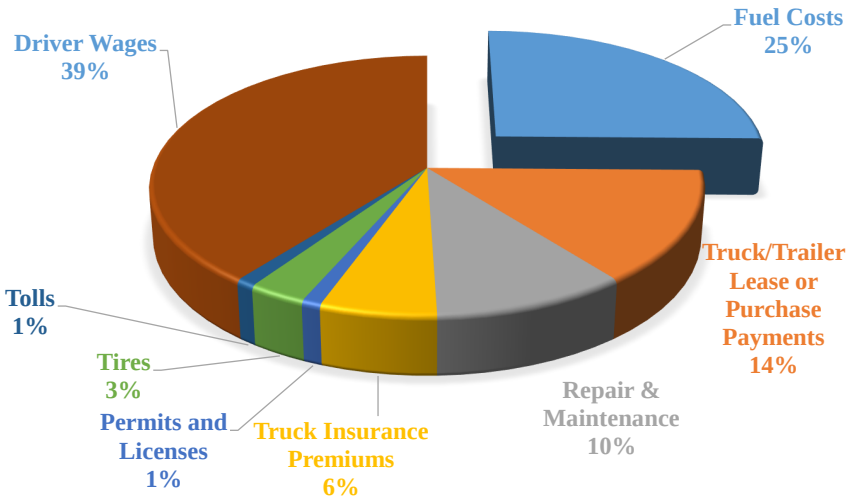

Figure 1.3: Share of annual operation cost for HDVs. Source: American Transportation Research Institute Analysis of the operational Costs of Trucking 2016

Despite the success of the program, challenges remain in the area of reducing technological costs as well as improving reliability. To address these challenges, in August 2014, DOE launched the SuperTruck II program to drive progress toward more specific products and closer-to-market commercialization. Besides the bold goal of achieving greater than 100 percent improvement in freight efficiency [6], the participants in the DOE initiative are required to develop technologies that can reach the market quickly, while saving money and delivering the same or better performance than that of the 18-wheelers of today.

Among many prospective technological directions for the SuperTruck I and II initiatives, the technology for optimizing energy management systems is of particular interest, because it can lead to applications beyond super trucks in the near future. This technology focuses on optimally utilizing the given powertrain systems, both for the well-designed powertrain system for the SuperTruck initiatives, and for the traditional ones used by current in-production vehicles. Thus, such technology could be used to improve fuel efficiency of currently operating fleets, bringing day-one benefits to the trucking industry and the whole transportation sector.

1.2 Eco-Driving: Fuel-Efficient Transport in Practice

The practice of optimally utilizing the given powertrain systems of automobiles and trucks has often been referred to as eco-driving, and has been studied over the past few decades. Indeed, many experiments have shown that given the same route, truck drivers have very different driving profiles (e.g., in terms of speed and gear engaged), resulting in a large

variation in fuel consumption [7]. This points to the large potential of eco-driving for fuel savings.

Since its early stage, considerable eco-driving research has been focused on driver education or online advice [8]. These studies generally offer empirically-based advice, such as driving at an economical cruise speed, and accelerating or decelerating less aggressively. Although this may lead to significant fuel efficiency improvements in the short term [9], degradation in the long term due to human behavior variations has remained an issue [10]. Thus, recently researchers have been relying on increasing levels of longitudinal automation, such as cruise control and adaptive cruise control.

Longitudinal automation, in particular, enables cooperative control of the engine and transmission, while taking the propulsion demand related to road elevation into consideration [11]. This may lead to fuel efficient driving profiles (including speed profiles and gear shift profiles). Since first studied, the problem of achieving fuel efficient driving profiles has been formulated as an optimal control problem. Over time, simple problems with simple linear vehicle dynamic models and elevation profiles models [12], [13] have developed into nonlinear, more complex, and more realistic models, which include detailed engine dynamics, gear shift dynamics, and aerodynamics [14]. To solve these complex optimal control problems in a reasonable amount of time (that enables real-time implementation), different techniques have been utilized, including analytical approaches [12, 15, 16], primitive sampling approaches [17, 18], direct "discrete and optimize" approaches [19], indirect necessary condition based approaches [20], dynamic programming based approaches [21] and stochastic dynamic programming approaches [22]. Typical improvements in fuel economy resulting from the these studies are around 10% over constant speed cruise control.

Improvements in fuel economy attributable to eco-driving design have been reported based on numerical studies on standard driving cycles, and/or real experiments carried out in isolated environments. Typically, the above solving techniques rely on many parameters that are tightly related to the testing scenario, and whose values may significantly affect the solutions. As a result, the parameters are extensively tuned for the testing scenarios. The resulting eco-driving designs with such parameters usually could not perform well for general scenarios because of such sensitivity on parameters. Thus, a real challenge in implementing the eco-driving design is to develop a systematic tools that allows the algorithms to be responsive to parameter changes. This issue will be revisited in Section 1.4.2.

Moreover, in the literature, the proposed eco-driving frameworks that incorporate engine and transmission control usually focus on fuel performance. For an automotive system, of equal, if not greater, importance are the safety and stability of the incorporated

system. These two aspects, however, tend to be overlooked, and no systematic and theoretical approach is available in the literature that provides safety and stability guarantees of the incorporated system. This issue will be revisited in Section 1.4.1.

1.3 Opportunities with Connected Automated Vehicle (CAV) Technology

While HDVs with eco-driving technologies can potentially gain as high as 10% fuel saving without traffic perturbations, the benefit may not be attainable in real traffic, where HDVs need to respond safely to their environment, including surrounding vehicles. In fact, studies designed to generate fuel efficient driving profiles have rarely considered road elevation information together with local dynamic traffic information, partially due the lack of technologies that can provide such traffic information in real time.

Recent developments in communication technologies [23], [24] can provide ground vehicles with increasing levels of connectivity. This connectivity enables more information sharing among the vehicles and the transportation infrastructure. Specifically, connectivity can be used to enhance automation by providing more information about local traffic environment. This may allow optimization of the vehicle powertrain for better fuel efficiency in a real, dynamic traffic environment. For example, vehicle-to-vehicle (V2V) and vehicle-to-infrastructure (V2I) communication may be used to obtain real-time traffic information to optimize speed profiles and gear changes. Such systems have a clear advantage compared to sensory systems that only provide information about the immediate surroundings of the vehicle [25] (e.g., about vehicle immediately ahead). V2V and V2I communication can also provide information with a relatively small latency compared to a service based on remote data aggregation (e.g., Google Maps). Specifically, V2V communication can provide data on the motion of multiple vehicles ahead, enabling unique beyond-line-of-site perception. Given these benefits, V2V communication devices that utilize various communication protocols (e.g., DSRC [26], C-V2X [27], 5G [28]) are starting to be available not only on new cars and new trucks, but also on existing ones [29]. Thus, traffic information acquired via connectivity is becoming increasingly available.

To utilize the information acquired from connectivity for safety and better fuel economy, some researchers have been focusing on designing centralized and cooperative controllers for platoons of automated vehicles [30]. For example, cooperative adaptive cruise control (CACC) establishes a fixed communication structure over a chain of automated vehicles following each others that share information within the group, and control their

motion cooperatively generating smoother driving patterns for all vehicles [31–33]. It has been demonstrated experimentally that such CACC system may bring fuel savings at the platoon level [34]. For HDVs, platoons formulated using CACC system may provide extra benefits; bringing trucks close to each other dramatically reduces the air resistance of the vehicles within the platoon [35, 36]. However, for platoons to be effective, the penetration rate of capable automated vehicles needs to be high [37]. Currently, the penetration rate is far from high enough.

Instead of relying on cooperation with other capable automated vehicles, over the past few years, to improve fuel economy, some researchers have focused on individual vehicles with communication capability that can incorporate forward traffic information acquired through connectivity. One popular approach has been optimizing fuel economy in a receding horizon optimal control (RHOC) framework (often called model predictive control or MPC) [38], [39], [40], [41], [42]. In the receding horizon approach, an optimization problem is formulated and solved to obtain fuel efficient actions, assuming the availability of perfect (or close to perfect) predictions about the motion of the vehicle immediately ahead. The advantage of this method is that multiple design objectives such as fuel economy, driving comfort, response to elevation, and safety can be explicitly incorporated. Fuel improvements resulting from the RHOC framework reported in the literature have been based on such accurate predictions over a long enough time horizon. In practice, however, a prediction is typically only available for a few seconds with limited accuracy [43]. Given the importance of accurate predictions, it is not clear how these RHOC-based methods would perform in terms of fuel economy in real traffic under inaccurate predictions, as fuel economy improvement may be compromised and safety hazards may occur. We will revisit this issue in Section 1.4.3.

To improve the fuel economy of an individual vehicle utilizing connectivity, it is also possible to directly include the motion information from multiple preceding vehicles in the feedback structure to obtain a connected cruise controller [44]. A vehicle driven by such a cruise controller is referred to as a connected automated vehicle (CAV) in the reminder of this dissertation. Recent studies have suggested that CAVs can improve traffic safety and efficiency, even for low penetration [45, 46]. More importantly, CAVs can achieve better fuel economy by tuning the feedback gains in a simple yet systematic manner [47], [48], [49]. Yet the question remains whether such a simple feedback controller can indeed save more fuel in real traffic. Further, it is unclear whether the performance is improved compared to the popular RHOC approach. Finally, there is the issue of safety concerns, as well as the matter of considering elevation information, both of which are nontrivial for such control frameworks and to date few studies have been presented along these directions.

We will also pick up these issues in Section 1.4.3.

1.4 Dissertation Contributions and Outline

Looking at the status of the research on fuel saving for heavy duty vehicles using connectivity and automation, this dissertation groups the potential issues found at three different levels as follows.

1. At the powertrain level, how to design the powertrain for an automated vehicle with engine and transmission control that is not only fuel efficient, but also safe and stable.

2. At the vehicle level, how to enable the application of fuel-efficient driving profile optimization based on elevation and traffic preview using connectivity, and how to efficiently carry out parameter analysis to maximize the benefit.

3. At the traffic level, how to utilize beyond line-of-sight information through connectivity to achieve safe and fuel-efficient longitudinal automation.

Correspondingly, this dissertation makes contributions by providing techniques to solve these issues at each level. The main contributions for each level are summarized as follows.

1.4.1 Powertrain level

In Chapter 3, the design of a safe, stable and fuel-efficient powertrain with internal combustion engine and discrete gearbox for an automated vehicle is studied. Particularly, we focus on the design of transmission gear shift schedule (see Figure 1.4).

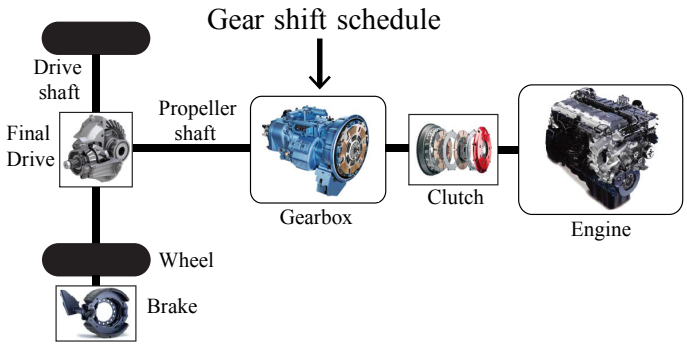

Figure 1.4: Powertain level: designing gear shift schedule

To design the gear shift schedules, the dynamics of an automated vehicle with engine and transmission control is first modeled as a hybrid system that contains dynamic variables of both discrete and continuous type. Using the theory of hybrid systems, Chapter 3 gives the rules by which a gear shift schedule design can ensure the safety and stability (in the sense of Lyapunov) of the integrated powertrain system. Based on these rules, a fuel-optimal gear shift schedule design is proposed and is compared with the current in-production design in terms of both fuel economy and towing ability.

1.4.2 Vehicle Level

Relying on the fuel efficient powertrain, Chapter 4 studies the design of eco-driving systems that generate fuel-efficient driving profile based on elevation and traffic preview using connectivity (see Figure 1.5). A design framework of eco-driving that incorporates general geographic information (e.g., elevation, wind), traffic information, and travel concerns (e.g., speed limit, travel time limit) is proposed, and formulated as a multi-objective optimal control problem. Also proposed is a systematic approach for analyzing the optimal trajectory for fuel efficient driving while varying parameters. Thus, such an approach enables quantification of the trade-offs among different objectives by setting parameters, and thus escalates industrial application of the eco-driving framework.

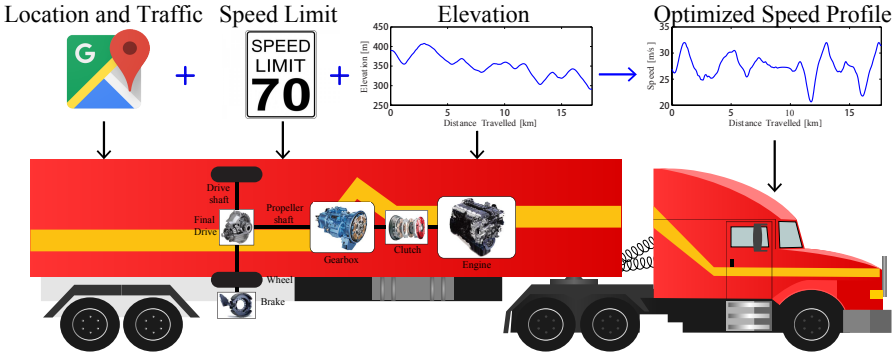

Figure 1.5: Vehicle level: optimizing speed profile while considering elevation and traffic information

1.4.3 Traffic level

Building upon the eco-driving framework, Chapter 5 and 6 propose safe and fuel efficient algorithm that can handle local dynamic traffic (see Figure 1.6). This enhancement would intervene only if the eco-driving framework fails to give safe commands.

Specifically, in Chapter 5, the source of fuel consumption reduction in traffic is first studied using a series of experiments. Based on these findings, the connected cruise controller is designed that directly feeds back the beyond line-of-sight information acquired through connectivity. Then, a data-driven optimization procedure is proposed which improves the fuel-economy while driving the vehicle in traffic. A comparison study between the proposed method and the RHOC approach is carried out to demonstrate the effectiveness of the proposed design.

In Chapter 6, the connected cruise controller is further enhanced with safety guaranteed features using the novel notion of the safety chart and the notion of minimal intervention. Such minimal intervention could maximize the usage of vehicle level fuel-saving which assumed sparse traffic.

Figure 1.6: Traffic level: safe and fuel efficient connected cruise control strategy that also responds to elevation.

1.5 Statement of Impact

This dissertation presents the state-of-the-art application of connectivity and automation in improving fuel economy. Specifically, this dissertation is one of the first few that deals with real experimental data collected using vehicle communication devices. This dissertation also presents the novel utilization of different theory in dynamics and control in automotive engineering, including classical and modern nonlinear control theory, hybrid control theory, optimal control theory, and analysis of dynamical system with delays.

1.6 Publications

The results in this dissertation can be also found in the following publications:

Journal Publication

5. **C. R. He**, J. I. Ge, and G. Orosz. Fuel Efficient Connected Cruise Control for Heavy-duty Trucks in Real Traffic. *IEEE Transactions on Control Systems Technology*, under review, 2018.

4. **C. R. He**, W. B. Qin, N. Ozay, and G. Orosz. Optimal Gear Shift Schedule Design for Autonomous Vehicles: Hybrid System Based Analytical Approach. *IEEE Transactions on Control Systems Technology*, 26(6):2078-2090, 2018.

3. J. I. Ge, S. S. Avedisov, **C. R. He**, W. B. Qin, M. Sadeghpour, and G. Orosz. Experimental validation of connected automated vehicle design among human-driven vehicles. *Transportation Research Part C*, 91:335-352, 2018.

2. G. Orosz, J. I. Ge, **C. R. He**, S. S. Avedisov, W. B. Qin, and L. Zhang. Seeing beyond the line of sight – controlling connected automated vehicles. *ASME Mechanical Engineering Magazine*, 139(12):S8-S12, 2017.

1. **C. R. He**, H. Maurer, G. Orosz. Fuel Consumption Optimization of Heavy Duty Vehicles with Grades, Wind, and Traffic Information. *ASME Journal of Computational and Nonlinear Dynamics*, 11(6):061011, 2016.

Refereed Proceedings

7. **C. R. He** and G. Orosz. Safety-guaranteed connected cruise control. *Proceedings of the 21st IEEE International Conference on Intelligent Transportation Systems*, 549-554, IEEE, 2018.

6. **C. R. He**, G. Orosz, and J. I. Ge. Fuel efficient connected cruise control for heavy duty vehicles. *Proceedings of the 14th International Symposium on Advanced Vehicle Control*, 2018.

5. **C. R. He**, J. I. Ge, and G. Orosz. Data-based fuel-economy optimization of connected automated trucks in traffic. *Proceedings of the American Control Conference*, 5576-5581, IEEE, 2018.

4. **C. R. He** and G. Orosz. Saving fuel using wireless vehicle-to-vehicle communication. *Proceedings of the American Control Conference*, 4946-4951, IEEE, 2017.

3. N. I. Li, **C. R. He** and G. Orosz. Sequential parametric optimization for connected cruise control with application to fuel economy optimization. *Proceedings of the Conference on Decision and Control*, 227-232, IEEE, 2016.

2. **C. R. He**, W. B. Qin, N. Ozay, G. Orosz, Hybrid System Based Analytical Approach For Optimal Gear Shifting Schedule Design. *Preceedings of the ASME Dynamic Systems and Control Conference*, no. DSCC2015-9943, pp. V003T41A003, ASME, 2015.

1. **C. R. He**, G. Orosz, Fuel Consumption Optimization of Heavy-Duty Vehicles: An Analytical Approach. *Preceedings of the ASME Dynamic Systems and Control Conference*, no. DSCC2014-6362, p. V002T20A006, ASME, 2014.

CHAPTER 2

Modeling

All models are wrong, but some are useful

GEORGE E. P. BOX

In this chapter we introduce the models that are involved in the connected automated truck design. The models presented in this chapter serve as the basis for analysis and control design in the following chapters. We start with formulating the longitudinal dynamics of the vehicle in Section 2.1. Then, we take a close look at the elevation modeling in Section 2.2, which is a major contribution to the external forces on the longitudinal dynamics of heavy duty vehicles. In Section 2.3 a simple powertrain model is presented to describe the internal forces that drive the vehicle, and we also characterize the corresponding energy consumption. In Section 2.4 a simulation model is introduced, which is used at the powertrain level and the vehicle level design evaluation. In Section 2.5 a high fidelity model is presented, which is used for evaluating the traffic level design. Finally, a summary in Section 2.6 concludes this chapter.

2.1 Vehicle Dynamics

The longitudinal dynamics of the HDV is derived using classical mechanics, with the assumption that no slip occurs on the wheels and that the flexibility of the tires and the suspension can be neglected. These assumptions are made typically for modeling oriented at fuel consumption optimization, and were shown valid and effective in the literature [35].

Based on the typical tractor and trailer configuration of the class 8 heavy duty truck, here we consider a model consist of 5 rigid bodies (1 driving axle , 2 front axle , 3 trailer chassis and body, 4 tractor chassis and body, and 5 rear axle) as shown in Figure 2.1, with the center of masses ($G_i, i = 1, \ldots, 5$) marked as black dots, and dimensions marked by grey. The masses and mass moment of inertias of these five parts are denoted by m_i and

J_{Gi}, $i = 1, \ldots, 5$, respectively. The truck is driving straight on a slope with inclination angle ϕ. The direction of gravity (g) is indicated by the purple arrow. An Euclidian frame is formulated with x along the slope surface while y perpendicular to the slope surface.

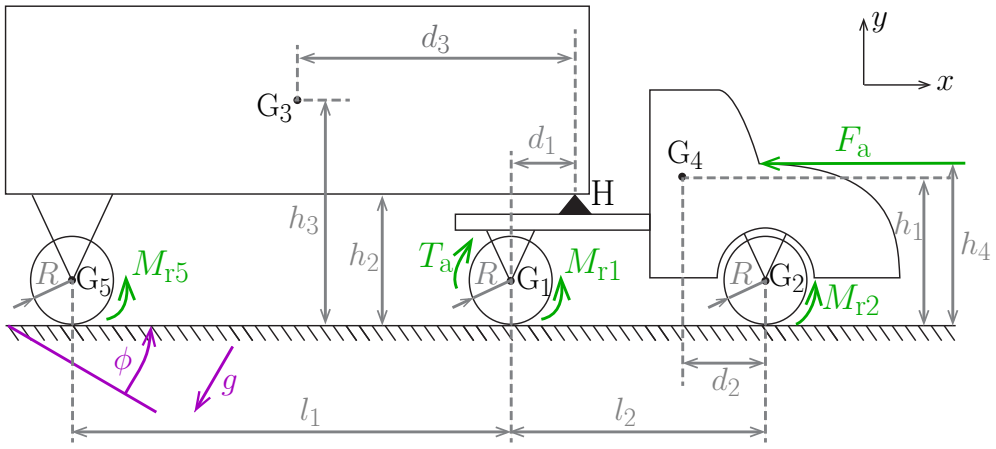

Figure 2.1: Conceptual figure of a heavy duty vehicle model, with five rigid bodies (1 driving axle, 2 front axle, 3 trailer chassis and body, 4 tractor chassis and body, and 5 rear axle).

All external forces and torques that are of interest are marked as green arrows in Figure 2.1. T_a denotes the axle torque on driving axle, which is the sum of the driving torque T_d, and braking torque T_b. The driving torque comes from the powertrain, while the braking torque comes from brake module, both of which will be introduced in Section 2.3. There are two types of resistance considered in the model, both are important contributors to the fuel consumption of heavy-duty trucks [35]. F_a is the air resistance force parallel to the ground surface at the height h_4 off the ground. The rolling resistance torque for each wheel is denoted as M_{ri}, $i = 1, 2, 5$. Their expressions will be introduced later in this section.

The free body diagrams for each rigid body are shown in Figure 2.2. In each free body diagram, the forces and torques are marked as green arrows. The speed and acceleration of the center of mass are marked as blue and red arrows, respectively. The reaction forces between rigid bodies are denoted as K_i, the normal forces from the ground to the wheels are denoted as N_i, while the traction and friction forces are denoated as C_i. With these diagrams, the Newton-Euler equations can be given for each rigid body.

Driving Axle (rigid body 1)

$$x: \quad C_1 - K_{1x} - m_1 g \sin\phi = m_1 a_1, \tag{2.1}$$

$$y: \quad N_1 - K_{1y} - m_1 g \cos\phi = 0, \tag{2.2}$$

$$z: \quad C_1 R + M_{r1} - T_a = J_{G1}\alpha_1, \tag{2.3}$$

Front Axle (rigid body 2)

$$x: \quad -C_2 - K_{2x} - m_2 g \sin\phi = m_2 a_2, \tag{2.4}$$

$$y: \quad N_2 - K_{2y} - m_2 g \cos\phi = 0, \tag{2.5}$$

$$z: \quad -C_2 R + M_{\mathrm{r}2} = J_{\mathrm{G}2}\alpha_2, \tag{2.6}$$

Trailer (rigid body 3)

$$x: \quad K_{4x} + K_{5x} - m_3 g \sin\phi = m_3 a_3, \tag{2.7}$$

$$y: \quad K_{4y} + K_{5y} - m_3 g \cos\phi = 0, \tag{2.8}$$

$$z: \quad K_{4y} d_3 + K_{4x}(h_3 - h_2) - K_{5y}(l_1 + d_1 - d_3) - K_{5x}(h_3 - R) = 0, \tag{2.9}$$

Tractor (rigid body 4)

$$x: \quad -F_{\mathrm{a}} - m_4 g \sin\phi + K_{1x} + K_{2x} - K_{4x} = m_4 a_4 \tag{2.10}$$

$$y: \quad K_{1y} + K_{2y} - K_{4y} - m_4 g \cos\phi = 0, \tag{2.11}$$

$$\begin{aligned} z: \quad & M_0 + F_{\mathrm{a}}(h_1 - h_4) + K_{4y}(l_2 - d_1 - d_2) - K_{4x}(h_4 - h_2) \\ & - K_{1y}(l_2 - d_2) + K_{1x}(h_4 - R) \\ & + K_{2y} d_2 + K_{2x}(h_4 - R) = 0. \end{aligned} \tag{2.12}$$

Rear Axle (rigid body 5)

$$x: \quad -C_5 - K_{5x} - m_5 g \sin\phi = m_5 a_5, \tag{2.13}$$

$$y: \quad N_5 - K_{5y} - m_5 g \cos\phi = 0, \tag{2.14}$$

$$z: \quad -C_5 R + M_{\mathrm{r}5} = J_{\mathrm{G}5}\alpha_2, \tag{2.15}$$

The rolling resistant for each wheel is given by

$$M_{\mathrm{r}i} = \gamma_0 R N_i, \quad i = 1, 2, 5. \tag{2.16}$$

where γ_0 is the rolling resistance coefficient and it is assumed to be the same for each wheel R is the wheel radius, while N_i are the normal forces. Since all the rigid bodies are traveling together and no suspension dynamics are considered, they should have the same

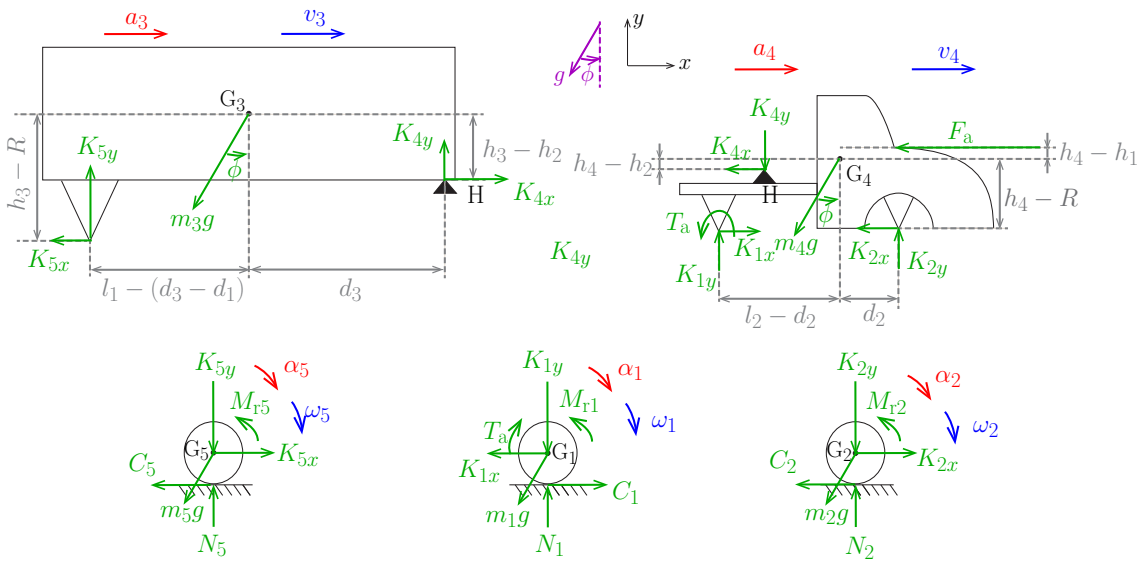

Figure 2.2: Free body diagrams

acceleration at the center of mass. That is,

$$a_i = a = \dot{v}, \quad i = 1, \ldots, 5, \tag{2.17}$$

where a and v are the longitudinal acceleration and speed of the truck. Since we assume that the wheels are all rolling without slipping, we have

$$\alpha_i = \alpha = \frac{a}{R}, \quad i = 1, 2, 5. \tag{2.18}$$

After substituting (2.17),(2.18) into (2.1)-(2.18), the 15 unknowns are

$$C_1, C_2, C_5, K_{1x}, K_{2x}, K_{4x}, K_{5x}, K_{1y}, K_{2y}, K_{4y}, K_{5y}, N_1, N_2, N_5, a. \tag{2.19}$$

First plugging (2.2),(2.5),(2.14),(2.8) into (2.11), one gets

$$\left(\sum_{i=1}^{5} m_i\right) g \cos\phi = N_1 + N_2 + N_5. \tag{2.20}$$

Then plugging (2.1),(2.4),(2.13),(2.7) into (2.10), one gets

$$\left(\sum_{i=1}^{5} m_i\right) a = C_1 - C_2 - C_5 - \left(\sum_{i=1}^{5} m_i\right) g \sin\phi - F_a. \tag{2.21}$$

Substituting C_1, C_2, C_5 with the expression generated from (2.3),(2.6),(2.15), and using

(2.20), one gets

$$\frac{T_{\mathrm{a}}}{R}-\gamma_0\Big(\sum_{i=1}^{5}m_i\Big)g\cos\phi-\frac{J_{\mathrm{G}_1}+J_{\mathrm{G}_2}+J_{\mathrm{G}_5}}{R^2}a-\Big(\sum_{i=1}^{5}m_i\Big)g\sin\phi-F_{\mathrm{a}}=\Big(\sum_{i=1}^{5}m_i\Big)a. \tag{2.22}$$

If we define

$$m=\sum_{i=1}^{5}m_i,\quad \text{and}\quad \bar{m}=m+\frac{J_{\mathrm{G}_1}+J_{\mathrm{G}_2}+J_{\mathrm{G}_5}}{R^2}, \tag{2.23}$$

the longitudinal dynamics are given by

$$\bar{m}a=-mg\sin\phi-\gamma_0 mg\cos\phi-F_{\mathrm{a}}+\frac{T_{\mathrm{a}}}{R}, \tag{2.24}$$

where T_{a} is the axle torque. Air resistance force is modeled as

$$F_{\mathrm{a}}=\frac{1}{2}\rho C_{\mathrm{d}}A(v+v_{\mathrm{w}})^2:=k(v+v_{\mathrm{w}})^2, \tag{2.25}$$

where C_{d} is air drag coefficient, ρ is the air density, A is the frontal area, and v_{w} is the headwind speed. Therefore, one has the longitudinal dynamics as

$$\bar{m}\dot{v}=-m\,g\sin\phi-\gamma_0\,m\,g\cos\phi-k(v+v_{\mathrm{w}})^2+\frac{T_{\mathrm{a}}}{R}. \tag{2.26}$$

Alternatively, one can use the power law and obtain the same longitudinal dynamics, see [44].

2.2 Elevation

Based on (2.26), the variation of elevation (often called the grade) is an important contributor to the external resistance forces. This is true especially for heavy duty vehicles considering their large mass and limited engine power.

The elevation h is available from GPS coordinates and can be converted to data in terms of either direct distance d or the distance travelled (arclength) s. This leads to a function $h(d)$ illustrated in Figure 2.3. Equivalently, $h(s)$ can be obtained using the arclength parametrization $d(s)$, for an alternative elevation description. Using the function $h(s)$, the inclination angle ϕ can be calculated as $h'(s)=\sin\phi$, that is, the $\sin\phi$ term in (2.26) can be substituted by $h'(s)$. One the other hand, for the road in the real world, ϕ is usually small ($|\phi|<0.05$ [rad]). Thus, the approximation $\cos\phi\approx 1$ is usually used in (2.26).

In practice, the $h(d)$ function would be available in discrete GPS data. Suppose we

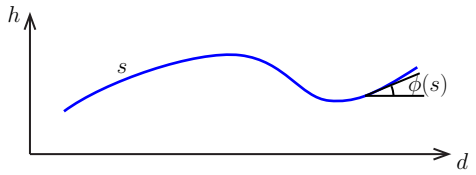

Figure 2.3: Elevation h as function of distance d and arc-lengths s.

have N pairs of such data, we use the following conversion to get a mesh for $h(s)$:

$$\begin{bmatrix} d_0 & d_1 & d_2 & \dots & d_N \\ h_0 & h_1 & h_2 & \dots & h_N \end{bmatrix} \begin{array}{c} \Delta s_i = \sqrt{(d_{i+1}-d_i)^2+(h_{i+1}-h_i)^2} \\ \Longleftrightarrow \\ s_{i+1} = s_i + \Delta s_i, \quad i=0,\dots,N \end{array} \begin{bmatrix} 0 & s_1 & s_2 & \dots & s_N \\ h_0 & h_1 & h_2 & \dots & h_N \end{bmatrix}. \tag{2.27}$$

We remark that the mesh for d may not be uniformly distributed, and thus, s would not be uniformly distributed either. Linear interpolation can be used to fill the gaps in $h'(s)$. Considering the scale of the route length versus the scale of GPS resolution, the error resulted from discretization and linear interpolation of the elevation profile may be ignored.

2.3 Vehicle Powertrain

The conceptual figure of a powertrain propelling a HDV is shown in Figure 2.4. It consists of an engine, a clutch, transmission shafts including gearbox, propeller shaft, final drive, and drive shaft, and wheels. General powertrain modeling can be carried out in various ways depending upon the purpose of study [50]. Our objective is to model the power flow from the engine to the drive shaft. Each component is described briefly in the reminder of this section and the powertrain model for the HDV is constructed. The notation for torques and angular speed used in this section is given in Figure 2.5, and will also be explained below.

Engine

The engine considered here is a diesel engine, a type of internal combustion engine where very highly compressed air and fuel are mixed in a combustion chamber, and the combustion resulted produces power [35]. The produced power drives the crankshaft and the clutch that connects to the flywheel at the end of crankshaft. Here, for simplicity, we do not consider the internal dynamics which characterizes the relation between the combustion, the injected fuel, and the power produced. Instead, a static fuel consumption map is used to describe the relation between the engine speed ω_{e}, the engine torque T_{e}, and the fuel consumption rate $q(\omega_{\mathrm{e}}, T_{\mathrm{e}})$. Considering the time scale of combustion versus the time scale

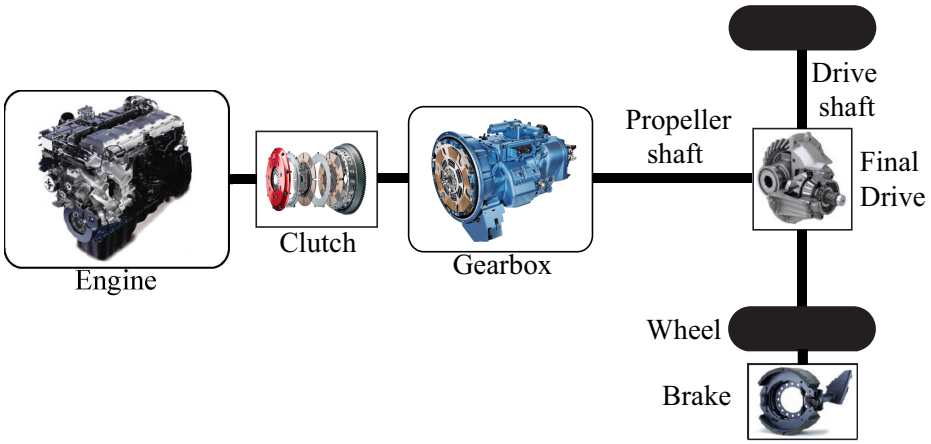

Figure 2.4: A conceptual plot of an HDV powertrain. (The pictures of the components are acquired online based on specification of a Navistar ProStar HDV)

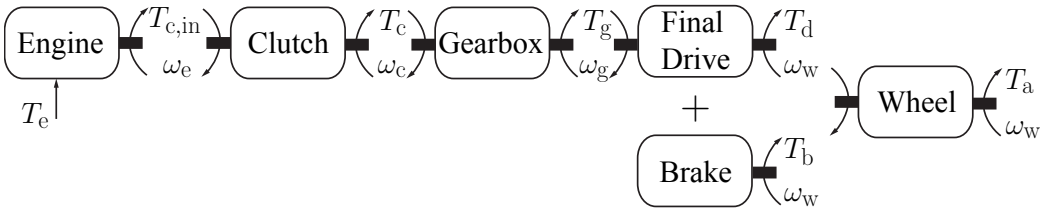

Figure 2.5: Components of the powertrain with notation for torques and angular velocities after each component.

of powertrain/vehicle speed control, such static model for fuel consumption is reasonable, and it is a common approach used in the literature [11]. Given a certain engine torque produced by combustion, the Newton-Euler equation of the angular motion lead to

$$J_e\dot{\omega}_e = T_e - T_{c,in}, \tag{2.28}$$

where T_e is the net engine torque output at the crankshaft, $T_{c,in}$ is load torque from the clutch, and J_e is the moment of inertia of the engine including the flywheel.

Dividing the fuel consumption rate with the engine power $P_e = T_e\omega_e$, we obtain the brake specific fuel consumption (BSFC):

$$\text{BSFC} = \frac{q(\omega_e, T_e)}{T_e\omega_e}. \tag{2.29}$$

that is used to evaluate the fuel economy of an engine, Small BSFC values typically imply good fuel economy [51] and it will be used in the fuel consumption design later.

Clutch

The clutch involves two frictional discs, one connects to the engine flywheel and the other to the gearbox's input shaft to enable gear shifts. Clutches are commonly found in vehicles equipped with manual gearbox (MT) or automated manual gearbox (AMT). When the two discs are pressed, the clutch is engaged. We assume negligible torque loss and speed difference at the connection point. Thus, we assume the connection between gearbox and the engine fly wheel through the clutch to be stiff, which can be modeled as

$$\begin{aligned} \omega_{\mathrm{e}} &= \omega_{\mathrm{c}}, \\ T_{\mathrm{c,in}} &= T_{\mathrm{c}}, \end{aligned} \tag{2.30}$$

where $T_{\mathrm{c,in}}$ and T_{in} are the input and output torque from the clutch respectively, and ω_c is the output angular speed from the clutch.

Gearbox

The gearbox uses gears (cogwheels) and gear trains to provide speed and torque conversions from a rotating power source to another device. In motor vehicles, gearbox connects the clutch and the propeller shaft. With a set of properly designed gears, the gearbox enables an engine to drive the vehicle at a large speed range. The speed conversion depends on which gear is engaged, and it is modeled as a ratio γ_{g} for each gear. For torque conversion, typically a slight drop arises when the gear is engaged due to frictional losses which are modeled as an efficiency η_{g} for each gear. Hence, at a given gear, the conversion due to gearbox is given as

$$\begin{aligned} T_{\mathrm{g}} &= \gamma_{\mathrm{g}}^{(i)} \eta_{\mathrm{g}}^{(i)} T_{\mathrm{c}}, \\ \gamma_{\mathrm{g}}^{(i)} \omega_{\mathrm{g}} &= \omega_{\mathrm{c}}, \end{aligned} \tag{2.31}$$

where T_{g} is the torque output and ω_{g} is the output angular speed from the gearbox, while index i corresponds to the gear index.

In this dissertation, gear shifts are assumed to happen instantaneously. Mathematically, such gear shift process is described as

$$\begin{aligned} T_{\mathrm{c}} &= \frac{T_{\mathrm{g}}^{(i)}}{\gamma_{\mathrm{g}}^{(i)} \eta_{\mathrm{g}}^{(i)}} = \frac{T_{\mathrm{g}}^{(j)}}{\gamma_{\mathrm{g}}^{(j)} \eta_{\mathrm{g}}^{(j)}}, \\ \omega_{\mathrm{c}} &= \gamma_{\mathrm{g}}^{(i)} \omega_{\mathrm{g}}^{(i)} = \gamma_{\mathrm{g}}^{(j)} \omega_{\mathrm{g}}^{(j)}, \end{aligned} \tag{2.32}$$

where index i, j corresponds to the gear indexes. Considering the time scale of the operation at vehicle level (few hundreds seconds) versus the gear shift duration (less than 1 second), such assumption is reasonable. For the design at powertrain level, such assumption facilitates the design and stability analysis, but neglects the fuel consumption during gear shift. Removing such assumption requires a more detailed modeling of dynamic processes during the gear shift (e.g. clutch engage and disengage process, fuel injection and torque generation for speed matching between engine flywheel and gearbox input shaft), and it is beyond the scope of this dissertation.

Final Drive

The final drive connects to the gearbox through the propeller shaft and to the wheels through the drive shaft. It is needed to change the torque direction so that the engine crankshaft can spin in a different direction than the driving axle (as indicated in Figure 2.4). Similar to the gearbox, the final drive is characterized by a conversion ratio γ_{f} and an efficiency η_{f}. The conversion ratio is designed such that the vehicle could travel at a reasonable fast speed while still get sufficient propulsion torque from the engine. Since the final drive is connected to the wheel directly, the output speed of the final drive is the wheel speed ω_{w}. Neglecting all inertia, and assuming negligible frictional losses in the propeller shaft and final shaft, the following relation between the torque and angular velocities at the input and the output of final drive can be given as:

$$\begin{aligned} T_{\mathrm{d}} &= \gamma_{\mathrm{f}} \eta_{\mathrm{f}} T_{\mathrm{g}}, \\ \gamma_{\mathrm{f}} \omega_{\mathrm{w}} &= \omega_{\mathrm{g}}. \end{aligned} \tag{2.33}$$

Brake

Typical brake system for HDVs is the S-cram drum brake that uses air brake chambers and an "S" shaped linkage to press the brake shoes against the surface of the brake drum. The brake system is located within the wheel such that the brake is applied directly to the driven wheels. Thus, the braking is modeled as a single torque T_{b} applied to the driving axle.

At the Driving Axle

To conclude this part of powertrain modeling, we combine (2.28),(2.30),(2.31) and (2.33) to obtain the driving torque produced by the powertrain:

$$T_{\mathrm{d}} = \gamma_{\mathrm{g}} \gamma_{\mathrm{f}} \eta_{\mathrm{f}} \eta_{\mathrm{g}} T_{\mathrm{e}} - J_{\mathrm{e}} \gamma_{\mathrm{g}}^2 \gamma_{\mathrm{f}}^2 \eta_{\mathrm{f}} \eta_{\mathrm{g}} \dot{\omega}_{\mathrm{w}}. \tag{2.34}$$

Thus, combining with the braking torque, the total axle torque in (2.26) is given by

$$T_{\mathrm{a}} = T_{\mathrm{d}} + T_{\mathrm{b}} = T_{\mathrm{b}} + \gamma_{\mathrm{g}}\gamma_{\mathrm{f}}\eta_{\mathrm{f}}\eta_{\mathrm{g}}T_{\mathrm{e}} - J_{\mathrm{e}}\gamma_{\mathrm{g}}^2\gamma_{\mathrm{f}}^2\eta_{\mathrm{f}}\eta_{\mathrm{g}}\dot{\omega}_{\mathrm{w}} \tag{2.35}$$

We define the total effective mass is given as

$$m_{\mathrm{eff}}(\eta) = \bar{m} + \frac{J_{\mathrm{e}}\gamma_{\mathrm{g}}^2\gamma_{\mathrm{f}}^2\eta_{\mathrm{f}}\eta_{\mathrm{g}}}{R^2}, \tag{2.36}$$

where $\eta = \gamma_{\mathrm{g}}\gamma_{\mathrm{f}}\eta_{\mathrm{f}}\eta_{\mathrm{g}}$ is defined to imply the the dependency of m_{eff} on gear. Combining (2.26) with model of powertrain, the longitudinal dynamics is given as

$$m_{\mathrm{eff}}(\eta)\dot{v} = -m\,g\sin\phi - \gamma_0\,m\,g\cos\phi - k(v+v_{\mathrm{w}})^2 + \frac{\eta T_{\mathrm{e}} + T_{\mathrm{b}}}{R}. \tag{2.37}$$

2.4 Simulation Model

Based on (2.37), a simulation model for the connected automated truck is built. The axle torque T_{a} is the control input in the simulation. When a particular gear is assigned, T_{e} and ω_{e} can be determined based on the current gear and torque required at the axles T_{a} at the current speed:

$$\omega_{\mathrm{e}} = \frac{\gamma_{\mathrm{g}}\gamma_{\mathrm{f}}}{R}v\,, \quad T_{\mathrm{e}} = \frac{T_{\mathrm{a}}}{\gamma_{\mathrm{g}}\gamma_{\mathrm{f}}\eta_{\mathrm{f}}\eta_{\mathrm{g}}}. \tag{2.38}$$

Then the fuel consumption can be calculated based on fuel consumption map $q(\omega_{\mathrm{e}}, T_{\mathrm{e}})$. Gearshifts are modeled to happen instantaneously along iso-power curves. That is, when shifting from i-th gear to i+1th gear (or $i+1$-th gear to ith) gear, we have

$$T_{\mathrm{e}}^{(i)}\omega_{\mathrm{e}}^{(i)} = T_{\mathrm{e}}^{(i+1)}\omega_{\mathrm{e}}^{(\mathrm{i}+1)}, \quad \frac{\omega_{\mathrm{e}}^{(i)}}{\gamma_{\mathrm{g}}^{(i)}} = \frac{\omega_{\mathrm{e}}^{(i+1)}}{\gamma_{\mathrm{g}}^{(i+1)}}, \quad T_{\mathrm{e}}^{(i)}\eta_{\mathrm{g}}^{(i)}\gamma_{\mathrm{g}}^{(i)} = T_{\mathrm{e}}^{(i+1)}\eta_{\mathrm{g}}^{(i+1)}\gamma_{\mathrm{g}}^{(i+1)}\,. \tag{2.39}$$

In practice, gearshift map is expressed as function of driver command CMD and the vehicle speed. Since axle torque demand is given at a given gear, the driver command is interpreted as

$$\mathrm{CMD} = \frac{T_{\mathrm{a}}}{T_{\mathrm{e,max}}(\omega_{\mathrm{e}})\eta}. \tag{2.40}$$

where $T_{\mathrm{e,max}}(\omega_{\mathrm{e}})$ is the maximum available engine torque as a function of engine speed. An in-production gear shift design is shown in Figure 2.6 [52]. The blue curves denote the upshift curves while the red dashed curves denote downshift curves. In the simulation, an upshift happens if the (v, CMD) pair crosses the upshift curve from left to the right while an down shift happens if the (v, CMD) pair crosses the downshift curve from right to the

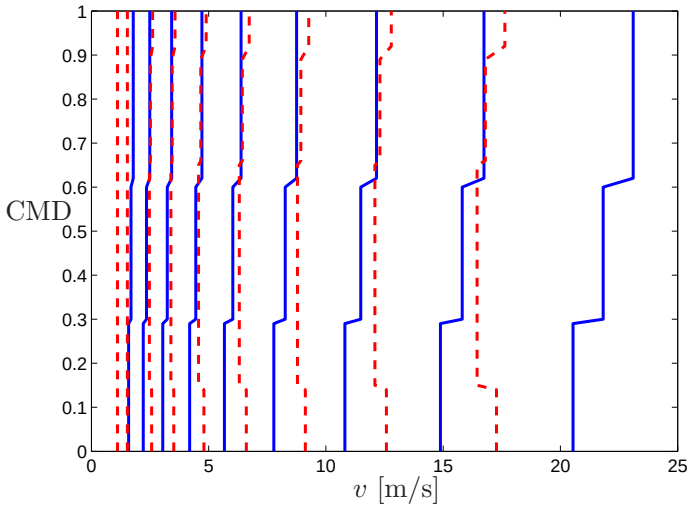

Figure 2.6: An in-production gear shift design of Navistar truck ProStar 2012, where the blue curves denote the upshift curves while the the red dashed curves denote downshift curves.

left.

The control of the automated truck that follows a reference speed profile $v_{\text{ref}}(t)$ can be achieved by a simple PI controller

$$\begin{aligned} T_{\text{a}} &= m_{\text{eff}}(\eta) R\big(K_{\text{P}}(v_{\text{ref}} - v) + K_{\text{I}} e\big), \\ \dot{e} &= v_{\text{ref}} - v, \end{aligned} \tag{2.41}$$

where K_{P} and K_{I} are the control gains. This PI controller will be used in the simulations for design validation at the powertrain level, where the truck is expected to follow a reference speed profile.

In the following chapters, we omit the dependency of m_{eff} on η in the design process by setting $J_{\text{e}} = 0$ for simplicity. Such assumption will not change the design principle and will not change the results qualitatively. In the simulation model, on the other hand, J_{e} is set to the real values. This simulation model is primarily used in Chapter 3 and 4.

The vehicle model (2.37) is only as good as the knowledge of all the vehicle parameters, which is summarized in Table 2.1. In fact, only the gearbox ratios and final drive ratio is known to be static. The inertias and efficiencies may vary based upon operating conditions which affect the lubrication. The wheel radius may vary based on air temperature and pressure as the tire is deforming while driving. The rolling resistance torque also depends nonlinearly on the vehicle speed. External factors such as road resistance and wind are hard to know accurately. However, considering daily operation of heavy duty vehicle, the dominant uncertainty is the vehicle mass (specifically m_3 in Figure 2.1) as the

Parameter	Value
Mass (fully loaded) (m)	29484 [kg]
frontal Area (A)	$10.68\mathrm{m}^2$
Tire Rolling Radius (R)	0.504 [m]
Tire Rolling Resistance Coefficient (γ)	0.006
Air Density (ρ)	1.20 [kg·m^{-3}]
Air Drag coefficient (C_{D})	0.6
$k = \frac{1}{2}\rho C_{\mathrm{D}} A$	3.84 [kg/m]
Maximum Acceleration ($a_{\max}$)	$2\ [\mathrm{m/s^2}]$
Rotational Element Inertia (J_{w})	39.9 [kg·m^2]
Engine Inertia (J_{e})	3.43 [kg·m^2]
Gravitational Constant (g)	9.81 [m/s^2]
Number of Forward Gears	10
1st Gear Ratio/Efficiency	12.94/0.97
2nd Gear Ratio/Efficiency	9.29/0.97
3rd Gear Ratio/Efficiency	6.75/0.97
4th Gear Ratio/Efficiency	4.9/0.97
5th Gear Ratio/Efficiency	3.62/0.97
6th Gear Ratio/Efficiency	2.64/0.97
7nd Gear Ratio/Efficiency	1.90/0.97
8rd Gear Ratio/Efficiency	1.38/0.98
9th Gear Ratio/Efficiency	1/0.99
10th Gear Ratio/Efficiency	0.74/0.98
Final Drive Ratio /Efficiency	3.73/0.96

Table 2.1: Nominal parameter values of a 2012 Navistar Prostar truck [1].

freight transport operations involve usually loading and unloading at multiple locations. The uncertainty on this mass is generally several orders of magnitude larger than the other parameters. Thus, we lump all the above uncertainties in the mass, which is a common approach in the literature [35].

2.5 High Fidelity Simulation Model with TruckSim

To evaluate the performance of a heavy-duty truck under higher-level controllers (e.g., connected cruise controller) in real traffic, we build a high-fidelity model in TruckSim based on a 2012 Navistar Prostar truck [1], and establish a co-simulation platform with MATLAB/Simulink. It captures primarily the longitudinal motion of the simulated heavy-duty truck. The configuration seen in Simulink is shown conceptually in Figure 2.7.

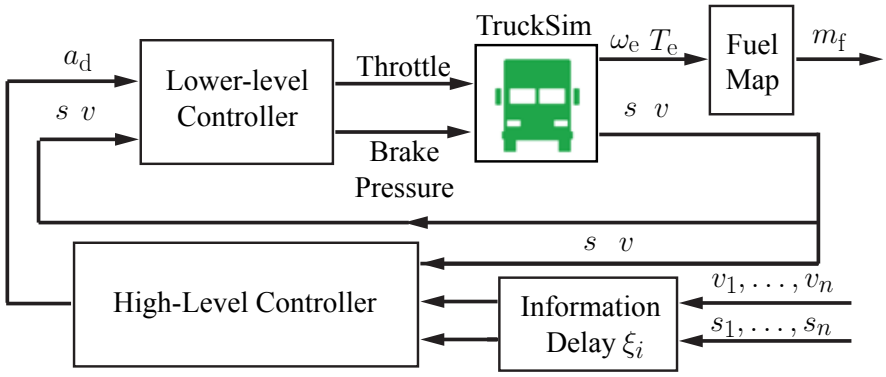

Figure 2.7: Structure of the high-fidelity simulation platform using TruckSim and MATLAB/Simulink to obtain the speed response and energy/fuel consumption of a truck responding to traffic perturbations.

The block "TruckSim" is a Simulink S-function that interacts with the high-fidelity model in TruckSim. The high-fidelity TruckSim model is built from the tractor-trailer model with the default class 8 sleeper cab tractor and a default trailer. The specifications of a Prostar 2012 shown in Table 2.1 are used for exterior, aero dynamics, and powertrain specifications. An engine throttle map based on the measurement of an in-production engine is integrated in the TruckSim model as well. For those dynamical specifications that do not appear in Table 2.1 (e.g., the brake actuator response curve), default data sets for the class 8 truck in TruckSim are used. As a result, this high-fidelity model takes throttle percentage and brake pressure as inputs, and reports the dynamic response of the truck with over a hundred states, including the longitudinal position s and speed v. With the states of engine speed (ω_{e}) and engine torque (T_{e}), the truck's fuel consumption can be obtained

using the same fuel map $q(\omega_{\mathrm{e}}, T_{\mathrm{e}})$ as in the simulation model. Compared to the simulation model in the previous section, the TruckSim model not only has a more detailed vehicle dynamic model, but also has a more detailed dynamic model about engine dynamics and clutch dynamics. Thus, the fuel consumption during gear shift is also estimated, providing a better fuel consumption estimation compared to the simulation model in the previous section.

The real traffic data collected using V2V devices are processed to describe the position $(s_1, \ldots s_n)$ and speed $(v_1, \ldots, v_n)$, of up to n preceding vehicles (n is adjustable) at a given time moment. An information delay block is applied to these position and velocity information before it goes to the controllers, simulating the real V2V communication behavior. In this co-simulation, the delay is set to be 0.1 second unless being specified otherwise. The higher level controller takes the host vehicle states (e.g., position s speed v) as well as the information about preceding vehicles, and command a desired acceleration a_{d}. Then, the acceleration command is converted by a lower-level controller into throttle and brake commands, based on the simple dynamics (2.37), and the throttle and brake maps used in the TruckSim model.

Once the control algorithm in the higher level controller block is specified, the co-simulation is capable of estimating the fuel performance when the heavy duty vehicle is driving in the real traffic. This model is primarily used in Chapter 5.

2.6 Summary

In this chapter, a series of models are presented to facilitate the control design and evaluation in the following chapters. First, a nonlinear model was derived that considered the external forces and powertrain mechanism. This model laid down the basis for the design and analysis in future chapters. Then, two simulation models were developed for different purposes. A simple simulation model was developed based on the derived nonlinear model while also taking into account idealized gear shift actions. This model is primarily used for the performance evaluation of the powertrain and of the vehicle level design. A high-fidelity model using TruckSim and MATLAB/Simulink co-simulation was also developed that takes into account more detailed powertrain and vehicle dynamics. This model is primarily used for the performance evaluation of the traffic level design.

CHAPTER 3

Fuel Efficient Gear Shift Schedule Design

Nothing is more practical than a good theory

KURT Z. LEWIN

In this chapter, the study at powertrain level is carried out. Hybrid system theory is applied to design a gear shift schedule that is fuel-efficient but can guarantee safety and stability of the powertrain.

Most ground vehicles are propelled by powertrains that use transmissions to match the vehicle state with the state of the engine. Transmissions enable reasonable sized engines to drive the vehicles in a wide range of speed. Ground vehicles driven on the US roads are typically equipped with automatic transmission (AT) or automated manual transmission (AMT) which shifts gear in response to driver command [53]. Designing the gear shift schedule appropriately allows one to improve the fuel economy, therefore it is a key component of transmission design. Traditional gear shift schedules are typically designed as a static map on the plane of the driver command (throttle/pedal position) and vehicle speed.

A recent trend in gear shift schedule design is to focus on better interpretation of the driver's intention and estimation of road environment [54–60]. However, including driver demand in the gear shift schedule design explicitly can make the design very challenging and optimality may be difficult to achieve. For connected and automated vehicles, axle torque demand is explicitly assigned, and thus can be met by setting the engine torque and the gears appropriately while bypassing the need for monitoring driver demand. The gear shift schedule design can be carried out based on torque demand and vehicle speed, while the design parameters have clear physical meanings and can be adjusted according to driving conditions; see Figure 3.1. With a properly designed pedal-torque map, the same gear shift schedule can also be used in human driven mode. Moreover, the automated vehicle may utilize traffic information to meet the torque demand while minimizing fuel consumption, so that the drivability and towing ability of the vehicle are not compromised. Meeting all these requirements in a reliable manner requires a rigorous mathematical approach.

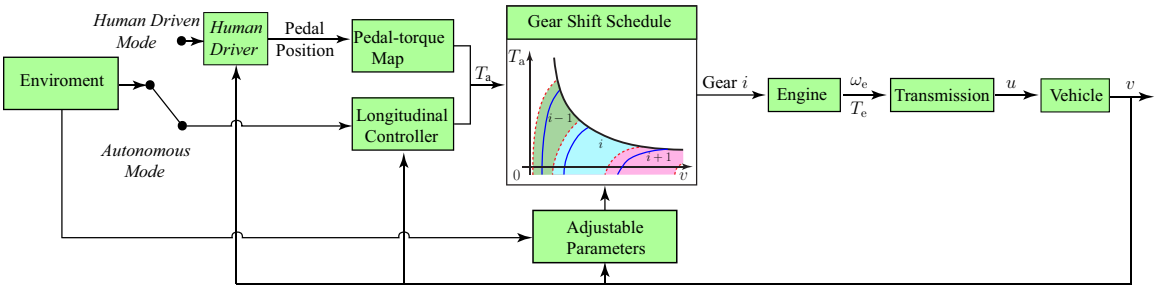

Figure 3.1: Gear shift schedule implementation for automated vehicles, where T_{a} is the required axle torque, v is the speed of the vehicle, T_{e} is the engine torque, ω_{e} is the engine speed, and u is the commanded acceleration of the vehicle.

The dynamics of an automated vehicle with AT/AMT can be modeled as a hybrid system which contains dynamic variables of both discrete and continuous types [61,62,63]. Analyzing the dynamics of these systems is challenging especially when the governing equations are nonlinear [64–66], and this is certainly the case for automobiles and trucks. Driver as an advanced controller can handle many complicated scenarios. Integrating controllers over a powertrain designed for a human driven vehicle may require a lot of efforts on testing and tuning in order to make a safe overall system for an automated vehicle. To bypass this, we take a simplified approach that is primarily tailored for automated vehicles as suggested by Figure 3.1. Specifically, we propose a framework for gear shift schedule design for AT/AMT, that is based on a first principle dynamic model and direct optimization. By using methods from hybrid systems we prove the stability of the gear shift design under state and input constraints. Based on our analysis, we improve the fuel economy of a class 8 heavy duty truck.

The remainder of this chapter is organized as follows. In Sections 3.1 we describe the modeling framework that leads to a hybrid system. Then we present the shift schedule design framework in Section 3.2 and prove that it can be used to achieve stable operating points in Section 3.3. In Section 3.4 we apply the proposed design to a heavy-duty vehicle and demonstrate the effectiveness of our proposed framework under different requirements. Finally, we summary this chapter.

3.1 Vehicle Dynamics With Gear Changes

In this section we describe the longitudinal dynamics of the vehicle with gear shift. We study forward driving only, therefore we develop the model for nonnegative vehicle speed. We then rewrite the equations using engine-based quantities to include the gear change explicitly. In order to make the problem analytically tractable, the longitudinal motion of

the vehicle is modeled by differential equations, the engine fuel consumption is calculated using a static map, and the gear shifts are considered to be instantaneous.

3.1.1 Modeling Vehicle Dynamics

Here we use the longitudinal vehicle model from [44,35]. Neglecting the flexibility of the suspension and the tires, Newton's second law yields

$$m_{\text{eff}}\dot{v} = -mg\sin\phi - \gamma_0 mg\cos\phi - k_0(v+v_{\text{w}})^2 + \frac{\eta T_{\text{e}} + T_{\text{b}}}{R}, \tag{3.1}$$

where $m_{\text{eff}} = m + J/R^2$ is the effective mass, containing the mass of vehicle m, the mass moment of inertia J of the rotating elements, and the wheel radius R. Also, g is the gravitational constant, ϕ is the inclination angle, γ_0 is the rolling resistance coefficient, k_0 is the air drag constant, v_{w} is the velocity of the head wind, η is the gear ratio. Since we assume the vehicle is traveling forward, we have $\eta > 0$. Finally, T_{e} is the engine torque, T_{b} is the braking torque, which are the control inputs that we need to design. For simplicity, we assume the vehicle is traveling on a flat road with no headwind, i.e., $\phi = 0$ and $v_{\text{w}} = 0$. Thus, we have

$$\dot{v} = -\gamma\,\text{g} - k\,v^2 + u, \tag{3.2}$$

where

$$\gamma = \frac{m}{m_{\text{eff}}}\gamma_0, \qquad k = \frac{k_0}{m_{\text{eff}}}, \qquad u = \frac{\eta T_{\text{e}} + T_{\text{b}}}{m_{\text{eff}} R}, \tag{3.3}$$

and the input u has unit $[\text{m/s}^2]$, so it can be considered as the commanded acceleration.

In general, the control may lead to $v < 0$. Here we design a controller that ensures the invariance of the region $v \geq 0$. In particular, we specify the control law at $v = 0$ such that, if $u \geq \gamma g$, $\dot{v}$ is still given by (3.2), while if $u < \gamma g$, we select u such that $\dot{v} = 0$. This is equivalent to

$$\dot{v} = -f(v) + u, \tag{3.4}$$

where

$$f(v) = \begin{cases} \gamma g + kv^2\,, & v > 0\,, \\ \min\{\gamma g, u|_{v=0}\}\,, & v = 0\,. \end{cases} \tag{3.5}$$

In order to start the vehicle at $v = 0$, one needs $u > \gamma g$ to obtain $\dot{v} > 0$, otherwise the vehicle remains stand still. On the other hand, when $v = 0$, for $u < \gamma g$, $f(0)$ could take values such that $\dot{v} = 0$, which makes the graph of $f(0)$ a line section instead of a single point.

For simplicity, the control input u is given by the PI controller

$$\begin{aligned} u &= K_{\mathrm{P}}\dot{w} + K_{\mathrm{I}}w\,, \\ \dot{w} &= v_{\mathrm{r}} - v\,. \end{aligned} \tag{3.6}$$

Thus, equations (3.4,3.5,3.6) give the closed-loop dynamics

$$\begin{aligned} \dot{v} &= -f(v) + K_{\mathrm{P}}(v_{\mathrm{r}} - v) + K_{\mathrm{I}}w, \\ \dot{w} &= v_{\mathrm{r}} - v\,, \end{aligned} \tag{3.7}$$

that can be rewritten in terms of the variables v and u as

$$\begin{aligned} \dot{v} &= -f(v) + u, \\ \dot{u} &= -K_{\mathrm{P}}\big(- f(v) + u - \dot{v}_{\mathrm{r}}\big) - K_{\mathrm{I}}\,(v - v_{\mathrm{r}})\,. \end{aligned} \tag{3.8}$$

When considering constant reference speed $v_{\mathrm{r}}(t) \equiv v_{\mathrm{r}}^* > 0$, system (3.8) possesses the equilibrium

$$\begin{aligned} v^* &= v_{\mathrm{r}}^*, \\ u^* &= f(v_{\mathrm{r}}^*)\,. \end{aligned} \tag{3.9}$$

Remark 1. *All the analyses in this chapter can be extended to $f(v)$ that satisfies*

$$f(v) > 0, \quad \frac{\mathrm{d}f}{\mathrm{d}v} > 0, \quad \frac{\mathrm{d}^2 f}{\mathrm{d}v^2} > 0, \quad \forall\, v\, > 0, \tag{3.10}$$

as no analysis uses explicitly the detailed form of f.

3.1.2 Introducing Gear Change

Assume that the transmission system has N gears, i.e., $\eta \in \{\eta_i \,|\, i \in \{1\,, 2\,, \cdots\,, N\}\}$. Then with i-th gear applied, the angular speed of the engine and the engine torque are given by

$$\omega_{\mathrm{e}} = \frac{\eta_i}{R} v\,, \quad T_{\mathrm{e}} = \frac{m_{\mathrm{eff}} R}{\eta_i}\, u, \tag{3.11}$$

that defines a linear transformation from the (v, u)-space to the $(\omega_{\mathrm{e}}, T_{\mathrm{e}})$-space. Henceforth, the closed-loop dynamics (3.8) can be rewritten as

$$\begin{aligned}\dot{\omega}_{\mathrm{e}} =& \tfrac{\eta_i}{R} f\left(\tfrac{R}{\eta_i}\omega_{\mathrm{e}}\right) + \tfrac{\eta_i^2}{m_{\mathrm{eff}}R^2} T_{\mathrm{e}},\\ \dot{T}_{\mathrm{e}} =& -\tfrac{m_{\mathrm{eff}}RK_{\mathrm{P}}}{\eta_i}\left(-f\left(\tfrac{R}{\eta_i}\omega_{\mathrm{e}}\right) + \tfrac{\eta_i}{m_{\mathrm{eff}}R} T_{\mathrm{e}} - \dot{v}_{\mathrm{r}}\right)\\ & -\tfrac{m_{\mathrm{eff}}RK_{\mathrm{I}}}{\eta_i}\left(\tfrac{R}{\eta_i}\omega_{\mathrm{e}} - v_{\mathrm{r}}\right).\end{aligned} \tag{3.12}$$

With gear change, this can be written into the compact form

$$\begin{aligned}&\begin{bmatrix}\dot{\omega}_{\mathrm{e}}(t)\\ \dot{T}_{\mathrm{e}}(t)\end{bmatrix} = F_i\big(\omega_{\mathrm{e}}(t), T_{\mathrm{e}}(t), v_{\mathrm{r}}(t)\big), && \text{if} \quad [\dot{\omega}_{\mathrm{e}}(t), \dot{T}_{\mathrm{e}}(t)] \in \mathcal{X}_i,\\ &\begin{bmatrix}\omega_{\mathrm{e}}(t^+)\\ T_{\mathrm{e}}(t^+)\\ i(t^+)\end{bmatrix} = S\big(\omega_{\mathrm{e}}(t^-), T_{\mathrm{e}}(t^-), i(t^-)\big), && \text{if} \quad [\omega_{\mathrm{e}}(t^-), T_{\mathrm{e}}(t^-)] \in \partial\mathcal{X}_{i(t^-)},\end{aligned} \tag{3.13}$$

for $i \in \{1, \cdots, N\}$. The function F_i represents the right hand side of (3.12) and it describes the continuous time dynamics for gear i when the state evolves inside the set $\mathcal{X}_i$. Moreover, S represents the gear shift schedule to be designed and describes the switches at the boundary of the set $\mathcal{X}_i$ (denoted by $\partial\mathcal{X}_i$) while t^- and t^+ denote the moment right before and right after a gear shift, respectively. In Section 3.2, we design the gear shift schedule to achieve optimal fuel consumption while in Section 3.3 we formally prove that the proposed design guarantees the stability of the overall hybrid system (3.13), that is, the stability of the equilibrium (3.9) of system (3.8) under gear change.

3.2 Gear Shift Schedule Design

In this section we explain the gear shift design process. For simplicity, we assume that the efficiency coefficients of torque delivery at different gears are the same. As shown by the numbers in Table 2.1, this is a very good approximation.

3.2.1 Design Process

The goal of gear shift schedule design is to select the gear that minimizes the fuel consumption while allowing the transmission to deliver the acquired torque/power. The fuel consumption can be quantified by measuring the mass flow rate of fuel $\dot{m}_{\mathrm{f}} = q(\omega_{\mathrm{e}}, T_{\mathrm{e}})$ as a function of the engine speed ω_{e} and engine torque T_{e}. To determine how efficiently

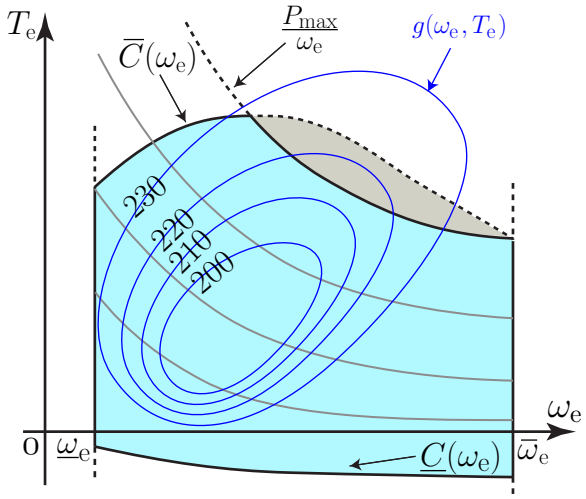

Figure 3.2: Conceptual BSFC map. The blue contours correspond to the constant levels of BSFC $g(\omega_e, T_e) = c$, the grey curves represent the iso-power curves and the black curves represent the limitation of the engine. Since the grey region is only accessible in certain gears, the blue region is considered as the engine operating region.

the engine uses fuel while producing power $P = \omega_e T_e$, one can use the brake specific fuel consumption (BSFC) defined by

$$\text{BSFC} = g(\omega_e, T_e) = \frac{\dot{m}_f}{P} = \frac{q(\omega_e, T_e)}{\omega_e T_e}, \tag{3.14}$$

see [51]. Therefore, minimizing BSFC increases fuel efficiency. In practice, the function $g(\omega_e, T_e)$ is nonlinear and does not have an analytical expression, but it may be acquired experimentally and one may use interpolation to obtain the value of g for combination of (ω_e, T_e) where measurements are not available.

In Figure 3.2, the contours of a conceptual BSFC map are plotted as blue curves, together with the maximum and minimum constraints on the engine torque and engine speed, i.e., $\underline{C}(\omega_e) \leq T_e \leq \overline{C}(\omega_e)$ and $\underline{\omega}_e \leq \omega_e \leq \overline{\omega}_e$. Note that the grey region is only accessible in certain gears (i.e., a gear change would lead to a working point where the engine limitation is exceeded) and it is typically very small in practice. Thus, to simplify the derivation, we use the iso-power curve corresponding to P_{max} to bound the blue operating region that is given by

$$\omega_e \in [\underline{\omega}_e, \overline{\omega}_e], \quad T_e \in [\underline{C}(\omega_e), \overline{C}(\omega_e)], \quad T_e \omega_e \leq P_{max}. \tag{3.15}$$

We assume that $g(\omega_e, T_e)$ has a minimum in the operating region (3.15).

Also note that an engine can output negative torque, but the maximum absolute value of the negative torque is much smaller than that of the positive torque. As fuel consumption

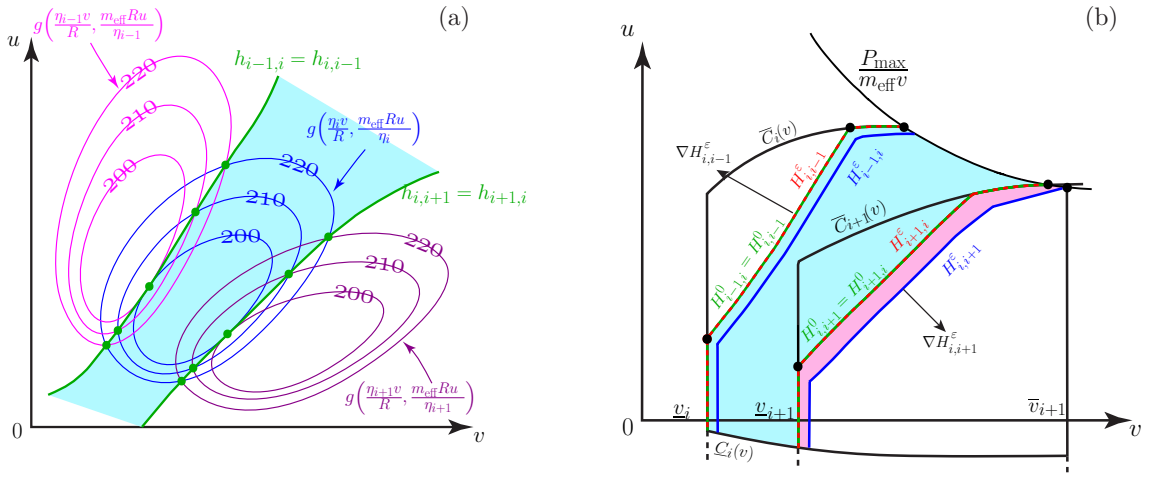

Figure 3.3: Gear shift concept. (a) Magenta contours, blue contours and purple contours represent the BSFC level sets as functions of the vehicle speed v and commanded acceleration u at the $(i-1)$-st, i-th and $(i+1)$-st gear, respectively. Connecting the intersections of BSFC contours results in the ideal shift curves $h_{i-1,i} = h_{i,i-1}$ and $h_{i,i+1} = h_{i+1,i}$ shown as green curves that bound the ideal working region for i-th gear highlighted as blue. (b) Capping the ideal shift curves with constraints due to engine limitations (cf. (3.15)). The resulting constrained working region for the i-th gear is bounded by the green curves $H^0_{i-1,i} = H^0_{i,i-1}$ and $H^0_{i,i+1} = H^0_{i+1,i}$, and is shaded as blue. Moving the upshift curves to $H^{\varepsilon}_{i,i+1}$ and $H^{\varepsilon}_{i-1,i}$, as shown by the blue curves, while leaving the downshift curves intact, i.e., having $H^{\varepsilon}_{i,i-1} = H^0_{i,i-1}$ and $H^{\varepsilon}_{i+1,i} = H^0_{i+1,i}$ to the right, as shown by the red dashed curves, generate overlap regions between adjacent gears. The union of the blue and the red shading is the actual working region for the i-th gear denoted by $\mathcal{X}_i$.

measurements are typically available for positive torque values only, we assume that the fuel consumption is zero along the minimum torque curve $\underline{\mathrm{C}}(\omega_{\mathrm{e}})$ and use interpolation to obtain the fuel consumption for negative torque values. Still, for $T_{\mathrm{e}} \leq 0$ we use the strategy designed for small $T_{\mathrm{e}} > 0$ in order to avoid difficulties due to singularity of the BSFC at $T_{\mathrm{e}} = 0$; cf. (3.14).

We assume that the gear ratio is monotonically decreasing and no gear skipping is possible, that is,

$$\begin{aligned} &\eta_1 > \eta_2 > \cdots > \eta_N, \\ &i(t^+) \in \{i(t^-) - 1, i(t^-) + 1\}, \end{aligned} \tag{3.16}$$

for $i \in \{1, \cdots, N\}$ and $k = 1, 2, \ldots$ We also assume that shifting happens instantaneously along the iso-power curves shown as light grey curves in Figure 3.2. Mathematically, such gear shift process is described as

$$m_{\mathrm{eff}}\, u\, v = T_{\mathrm{e},i}\omega_{\mathrm{e},i}, \quad \frac{\omega_{\mathrm{e},i}}{\eta_i} = \frac{\omega_{\mathrm{e},i+1}}{\eta_{i+1}}, \quad T_{\mathrm{e},i}\eta_i = T_{\mathrm{e},i+1}\eta_{i+1}\,, \tag{3.17}$$

for $i \in \{1, \cdots, N-1\}$.

Our gear change strategy is to choose the gear with smallest BSFC value, which is shown graphically in (v, u)-space in Figure 3.3a. The blue contours correspond to $g\big(\frac{\eta_i v}{R}, \frac{m_{\mathrm{eff}} R u}{\eta_i}\big) = g\big(\omega_{\mathrm{e},i}, T_{\mathrm{e},i}\big) = c$, the purple contours correspond to $\big(\omega_{\mathrm{e},i+1}, T_{\mathrm{e},i+1}\big) = g\big(\frac{\eta_{i+1} v}{R}, \frac{m_{\mathrm{eff}} R u}{\eta_{i+1}}\big) = c$, while the magenta contours correspond to $g\big(\omega_{\mathrm{e},i-1}, T_{\mathrm{e},i-1}\big) = g\big(\frac{\eta_{i-1} v}{R}, \frac{m_{\mathrm{eff}} R u}{\eta_{i-1}}\big) = c$. The ideal upshift curve $h_{i,i+1}(v)$ from gear i to gear $i+1$ is determined by the solution of

$$g\left(\frac{\eta_i v}{R}, \frac{m_{\mathrm{eff}} R h_{i,i+1}(v)}{\eta_i}\right) = g\left(\frac{\eta_{i+1} v}{R}, \frac{m_{\mathrm{eff}} R h_{i,i+1}(v)}{\eta_{i+1}}\right), \tag{3.18}$$

that is visualized in Figure 3.3a by the green curves obtained from intersections of blue and purple contours (green dots). To be able to solve (3.18) for the function $h_{i,i+1}(v)$, the conditions for implicit function theorem are assumed to hold. Crossing this curve to the right, i.e., shifting one gear up, shall give a smaller BSFC value. Note that this is also the ideal downshift curve from gear $i+1$ to gear i, that is, $h_{i+1,i}(v) = h_{i,i+1}(v)$. Similarly, between the i-th and $(i-1)$-st gear, we can construct $h_{i-1,i}(v) = h_{i,i-1}(v)$ and define the operating region for the i-th gear, which is shown as the shaded blue in Figure 3.3a.

The ideal curves should be further tuned to satisfy the constraints given by the engine (cf. (3.15)), as indicated in Figure 3.3b. These constraints include minimum and maximum speed constraints ($\underline{v}_i = \underline{\omega}_{\mathrm{e}} R/\eta_i$ and $\overline{v}_i = \overline{\omega}_{\mathrm{e}} R/\eta_i$), engine maximum torque and minimum torque ($\overline{C}_i(v)$ and $\underline{C}_i(v)$), and maximum power $P_{\max}$. The modified curves are denoted by

$H^0_{i,i+1} = H^0_{i+1,i}$ and $H^0_{i-1,i} = H^0_{i,i-1}$, where the superscripts refer to the fact that the curves are given in the form $H^0_{j,k}(v,u) = 0$. These green curves bound the new ideal working region of the i-th gear, indicated by blue shading in Figure 3.3b. Note that depending on the engine specification, some of the constraints above may not be part of the boundary of the working region.

The above ideal working regions will lead to ambiguity in gear selection for (v,u) pairs that sit exactly on the curve $H^0_{i,i+1} = H^0_{i+1,i}$. To avoid this, we introduce hysteresis by generating a small overlap region between the gears by splitting the curves to $H^\varepsilon_{i,i+1} \neq H^\varepsilon_{i+1,i}$. For example, between the i-th and $(i+1)$-st gears, we move the upshift curve to the right (that is, $H^\varepsilon_{i,i+1} \neq H^0_{i+1,i}$) as shown by the blue solid curve in Figure 3.3b, while keep the downshift curves at the ideal curve (that is, $H^\varepsilon_{i+1,i} = H^0_{i+1,i}$) as shown by the red dashed curve in Figure 3.3b. The same strategy is applied between the $(i-1)$-st and the i-th gears. We can now define the actual working region $\mathcal{X}_i$ for the i-th gear, which is the union of the blue and the red regions in Figure 3.3b, while $\partial\mathcal{X}_i$ is given by the blue solid curves on the right and the red dashed curve on the left. Thus, the gear shift schedule (3.13) can be formally written as

$$\begin{aligned} \begin{bmatrix} \omega_{\mathrm{e}}(t^+) \\ T_{\mathrm{e}}(t^+) \\ i(t^+) \end{bmatrix} &= \begin{bmatrix} \omega_{\mathrm{e}}(t^-)\frac{\eta_{i(t^-)+1}}{\eta_{i(t^-)}} \\ T_{\mathrm{e}}(t^-)\frac{\eta_{i(t^-)}}{\eta_{i(t^-)+1}} \\ i(t^-)+1 \end{bmatrix}, \\ \text{if} \quad H^\varepsilon_{i,i+1}\left(\omega_{\mathrm{e}}(t^-)\tfrac{R}{\eta_{i(t^-)}}, T_{\mathrm{e}}(t^-)\tfrac{\eta_{i(t^-)}}{m_{\mathrm{eff}}R}\right) &= 0, \\ \nabla H^\varepsilon_{i,i+1}|_{t=t^-} \cdot \begin{bmatrix} \dot\omega_{\mathrm{e}}(t^-)\frac{R}{\eta_{i(t^-)}} \\ \dot T_{\mathrm{e}}(t^-)\frac{\eta_{i(t^-)}}{m_{\mathrm{eff}}R} \end{bmatrix} &> 0, \end{aligned} \tag{3.19}$$

and

$$\begin{aligned} \begin{bmatrix} \omega_{\mathrm{e}}(t^+) \\ T_{\mathrm{e}}(t^+) \\ i(t^+) \end{bmatrix} &= \begin{bmatrix} \omega_{\mathrm{e}}(t^-)\frac{\eta_{i(t^-)-1}}{\eta_{i(t^-)}} \\ T_{\mathrm{e}}(t^-)\frac{\eta_{i(t^-)}}{\eta_{i(t^-)-1}} \\ i(t^-)-1 \end{bmatrix}, \\ \text{if} \quad H^\varepsilon_{i,i-1}\left(\omega_{\mathrm{e}}(t^-)\tfrac{R}{\eta_{i(t^-)}}, T_{\mathrm{e}}(t^-)\tfrac{\eta_{i(t^-)}}{m_{\mathrm{eff}}R}\right) &= 0, \\ \nabla H^\varepsilon_{i,i-1}|_{t=t^-} \cdot \begin{bmatrix} \dot\omega_{\mathrm{e}}(t^-)\frac{R}{\eta_{i(t^-)}} \\ \dot T_{\mathrm{e}}(t^-)\frac{\eta_{i(t^-)}}{m_{\mathrm{eff}}R} \end{bmatrix} &> 0, \end{aligned} \tag{3.20}$$

where ∇ is the gradient operator for multi-variable functions (see the vectors in Figure 3.3b), cf. (3.17,3.18).

In Section 3.3, we will show that having overlap regions between gears is crucial for the stability of system (3.13). The size of the overlap region will affect the performance of the gear shift schedule as will be demonstrated through a case study on a heavy duty vehicle in Section 3.4.

3.3 Stability With Gear Changes

In this section, we prove that the hybrid system (3.13) is stable in the sense of Lyapunov with the proposed gear shift schedule (3.19,3.20). Before stating the main results of the section, we present some useful definitions, all of which are visualized graphically in Figure 3.4.

Definition 1. *A partition of a compact set $\mathcal{X} \subseteq \mathbb{R}^2$ is a collection of subsets $\{P_i\}_{i=1}^k$, $P_i \subseteq \mathcal{X}, P_i \neq \emptyset$, such that $\bigcup_{i=1}^k P_i = \mathcal{X}$ and $P_i \bigcap P_j = \emptyset$, $\forall\, i \neq j$.*

As shown in Figure 3.4a, the partition means that the P_i-s cover the set $\mathcal{X}$ and that there is no intersection between the P_i-s.

Definition 2. *Given a partition $\{P_i^{\mathrm{N}}\}_{i=1}^k$ of a compact set $\mathcal{X} \subseteq \mathbb{R}^2$, let $N_i = \{j \in \mathbb{N}^+ \mid \partial P_i^{\mathrm{N}} \cap \partial P_j^{\mathrm{N}} \neq \emptyset, i \neq j\}$. Then, $\{P_i^{\mathrm{N}}\}_{i=1}^k$ is called a 2-neighbor partition if $|N_i| \leq 2$.*

Here $|S|$ denotes the number of element of the set S and ∂S denotes the boundary of the set S. The superscript "N" stands for neighbor. The definition means that the P_i^{N}-s cover the set $\mathcal{X}$ and that each P_i^{N} has at most two neighbors; see Figure 3.4(b).

Definition 3. *Given a partition $\{P_i\}_{i=1}^k$, an ε-partition of a compact set $\mathcal{X} \in \mathbb{R}^2$ is a collection of subsets $\{P_i^\varepsilon\}_{i=1}^k$, $P_i^\varepsilon \subseteq \mathcal{X}, P_i^\varepsilon \neq \emptyset$, such that $\bigcup_{i=1}^k P_i^\varepsilon = \mathcal{X}$ and $P_i^\varepsilon \setminus P_j^\varepsilon \neq \emptyset$, $\forall\, i \neq j$, where $\varepsilon = \inf\{\rho > 0 \mid P_i^\varepsilon \subseteq (P_i \bigoplus B_\rho) \cap \mathcal{X}, \forall\, i\}$.*

Here, B_ρ denotes a ball with radius ρ around the origin and $\bigoplus$ denotes the Minkowski sum defined by $A \bigoplus B = \{z = x + y | x \in A, y \in B\}$. This definition means that the P_i^ε-s cover the set $\mathcal{X}$ and that each P_i^ε overlaps with its neighbors, while ε is the smallest radius for the ball that allows us to cover the overlap regions; see Figure 3.4(c). It is clear that as $\varepsilon \to 0$, an ε-partition $\{P_i^\varepsilon\}_{i=1}^k$ converges to a partition $\{P_i\}_{i=1}^k$.

Definition 4. *A 2-neighbor ε-partition of a compact set $\mathcal{X}$ is an ε-partition $\{P_i^{\mathrm{N}\varepsilon}\}_{i=1}^k$ of that set such that $|N_i| \leq 2$, $\forall i$ and $Q_{i,j}^{\mathrm{N}\varepsilon} \bigcap Q_{i,l}^{\mathrm{N}\varepsilon} = \emptyset$, $\forall j, l \in N_i$ where $N_i = \{j \in \mathbb{N}^+ | P_i^{\mathrm{N}\varepsilon} \bigcap P_j^{\mathrm{N}\varepsilon} \neq \emptyset, i \neq j\}$ and $Q_{i,j}^{\mathrm{N}\varepsilon} = P_i^{\mathrm{N}\varepsilon} \bigcap P_j^{\mathrm{N}\varepsilon}$.*

This definition means that the $P_i^{\mathrm{N}\varepsilon}$-s cover the set $\mathcal{X}$ and each $P_i^{\mathrm{N}\varepsilon}$ overlaps with its neighbors but there will be at most two neighbors for each $P_i^{\mathrm{N}\varepsilon}$; see Figure 3.4(d).

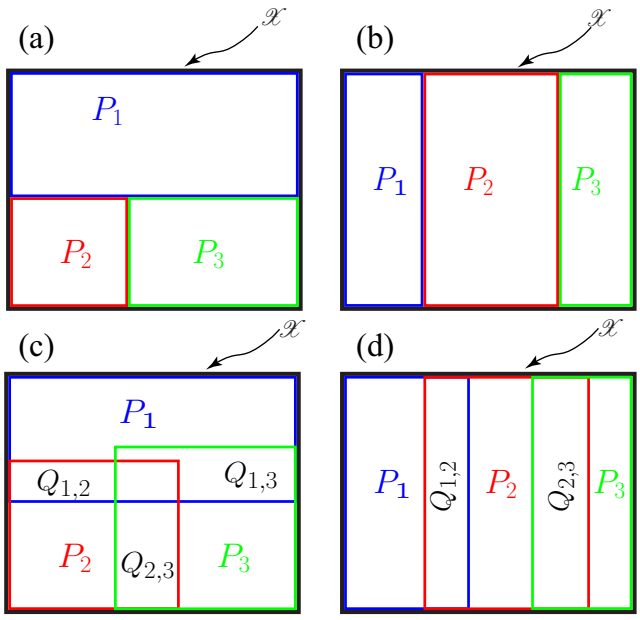

Figure 3.4: Visualization of definitions: (a) Partition. (b) 2-neighbor partition. (c) ε-partition. (d) 2-neighbor ε-partition.

Lemma 1. *Given a 2-neighbor ε-partition of a set $\mathcal{X}$, $\{P_i^{\mathrm{N}\varepsilon} \backslash (\bigcup_{j\in N_i} Q_{i,j}^{\mathrm{N}\varepsilon})\}_{i=1}^k \bigcup \{\bigcup_{j\in N_i} Q_{i,j}^{\mathrm{N}\varepsilon}\}_{i=1}^k$ gives a partition of the set $\mathcal{X}$.*

Proof. This is trivial since there is no intersection between any two intersections of any two of the partition elements $Q_{i,j}^{\mathrm{N}\varepsilon} = P_i^{\mathrm{N}\varepsilon} \bigcap P_j^{\mathrm{N}\varepsilon}$. □

Lemma 2. *A full-rank affine transformation preserves partition (or ε-partition or 2-neighbor partition or 2-neighbor ε-partition) of a set $\mathcal{X} \subseteq \mathbb{R}^2$.*

Proof. We prove this by contradiction. Suppose that the image of a partition is not a partition any more. It could be that $\bigcup_{i=1}^k P_i \neq \mathcal{X}$ or $\exists\, i \neq j$, $P_i \bigcap P_j \neq \emptyset$. Both cases imply that $\exists\, Q \in \mathrm{Im}(\mathcal{X})$, $Q \neq \emptyset$ such that $\mathrm{Pre}(Q) = \emptyset$, that is, the affine transformation maps a point to a nonempty set, which cannot be true for a full-rank affine transformation. □

Using Lemma 2, we can conclude that if the shift schedule (3.19,3.20) gives a 2-neighbor ε-partition, it maps all the equilibria of the system (3.8) that are not located in an overlap region to a unique equilibrium of the switched system (3.13). If an equilibrium of (3.8) is located in the overlap region, the shift schedule (3.19,3.20) will not map it to a unique equilibrium of (3.13). We will deal with this issue in Theorem 1.

Next, we define the working region of (3.8) on the (v, u)-plane. In particular, the power limit of the engine results in

$$u \leq \frac{P_{\max}}{m_{\mathrm{eff}} v}. \tag{3.21}$$

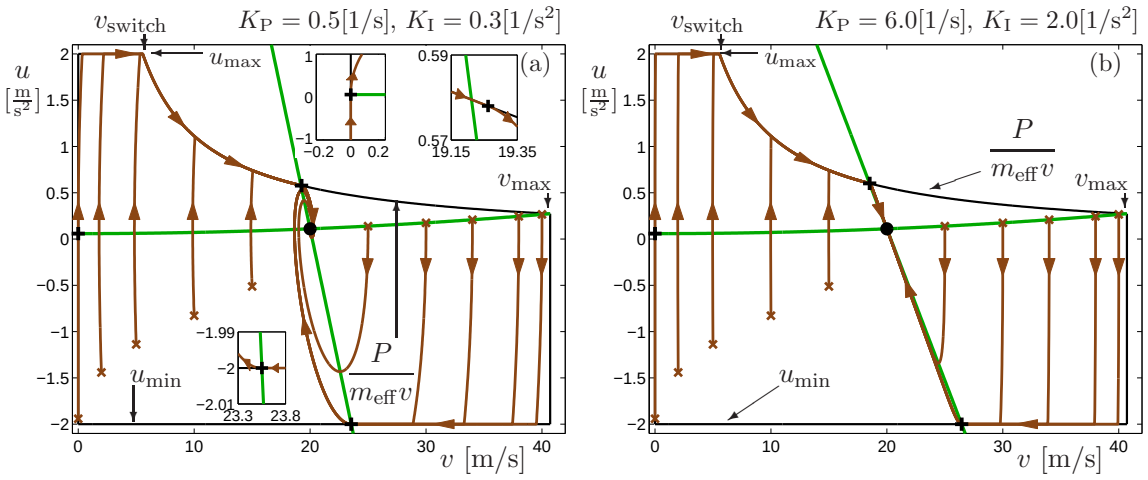

Figure 3.5: Phase plane dynamics of system (3.8) with constraints (3.26) for different control parameters as indicated. Trajectories starting from different initial points are marked as brown curves. The green curves denote the nullclines $u = f(v)$, and $u = \frac{K_{\text{I}}}{K_{\text{P}}}(v - v^*) + f(v)$ and they intersect at the equilibrium denoted by the black dot. The black solid pluses denote the exit points of trajectories along boundary arcs.

Besides this, we also impose the maximum and minimum constraints

$$u_{\min} \leq u \leq u_{\max}, \tag{3.22}$$

where $u_{\min}$ comes from braking torque limit, and it can only be applied when $v > 0$, while $u_{\max}$ is an upper bound due to the torque limitation of the engine (e.g., $\overline{C}(\omega_{\text{e}})$), and other physical limits at low vehicle speed. The speed where (3.21) starts to become active and (3.22) starts to become inactive is given by

$$v_{\text{switch}} = \frac{P_{\max}}{m_{\text{eff}} u_{\max}}. \tag{3.23}$$

Note that due to the relation between w and u given by (3.6), equations (3.21) and (3.22) impose constraints on w as well. This saturation, in fact, may lead to an anti-windup mechanism that improves the performance of the PI controller [67]. Recall that according to (3.5), $u_{\max} > \gamma g$ is needed to start a stationary vehicle. Finally, we restrict ourselves to the speed range

$$0 \leq v \leq v_{\max}, \tag{3.24}$$

where $v_{\max}$ is chosen to be the maximum steady state speed given by

$$P_{\max} - m_{\text{eff}} f(v_{\max}) v_{\max} = 0. \tag{3.25}$$

Since f is monotonically increasing for positive speed, $v_{\max}$ is unique.

Therefore, the constrained working region is given by

$$\left\{(v,u)|v\in[0,v_{\max}],\ u\in\left[u_{\min},\min\left(u_{\max},\frac{P_{\max}}{m_{\text{eff}}v}\right)\right]\right\}, \tag{3.26}$$

that is enclosed by the black curves in Figure 3.5. The following lemma states the stability conditions for an equilibrium of (3.8) within this domain.

Lemma 3. *If condition* (3.10) *holds, by choosing the feedback gains as*

$$K_{\mathrm{P}}>\frac{P_{\max}}{m_{\text{eff}}v_{\text{switch}}^2},\quad K_{\mathrm{I}}>K_{\mathrm{P}}f'(v_{\max}) \tag{3.27}$$

the equilibrium (3.9) *of system* (3.8) *is asymptotically stable and* (3.26) *is the region of attraction.*

The details of the proof are given in Section 3.3.1 where we propose a Lyapunov function and first show asymptotic stability of the equilibrium without constraints. Then, we show that the trajectories join and leave the boundaries of (3.26) at particular points (see the inlets in Figure 3.5a) and that the value of the Lyapunov function decreases while traveling along the boundaries. We remark that the conditions on K_{P} and K_{I} in Lemma 3 are easy to satisfy, as $f'(v_{\max})>0$ is usually small.

In Figure 3.5 we show trajectories as brown curves starting from multiple initial conditions (marked by brown crosses), for reference speed $v^*=20[\mathrm{m/s}]$, for two different sets of control parameters as indicated above. The conditions in Lemma 3 are satisfied in both cases. Indeed, all trajectories in Figure 3.5 converge to the equilibrium denoted by black dots. In Figure 3.5a the equilibrium appears as a focus while in Figure 3.5b it appears as a node. The green curves denote the nullclines $u=f(v)$ and $u=\frac{K_{\mathrm{I}}}{K_{\mathrm{P}}}(v-v^*)+f(v)$ (cf. (3.8)) that intersect at the equilibrium. The nullclines are utilized in the proof in Appendix 3.3.1. The black solid pluses denote the points along boundary arcs where the trajectories leave the arcs as highlighted by the inlets. These can be calculated analytically; see (3.36) in Appendix 3.3.1.

Before presenting the main theorem, we require one more assumption that should be satisfied when designing the shift schedule.

Assumption 1. *The gear shift schedule (3.19,3.20) gives a 2-neighbor ε-partition in the (v,u)-space. If $\varepsilon=0$ the gear shift schedule gives 2-neighbor partitions in the (v,u)-space.*

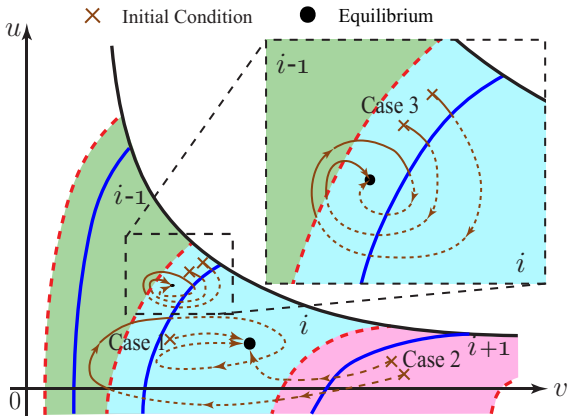

Figure 3.6: Sketch of the proof of Theorem 1. Trajectories associated with different cases, with part of the figures zoomed in. In cases 1 and 2, the equilibrium is in the non-overlap region and the trajectory evolves either without gear change (case 1) or with finitely many gear changes (case 2). In case 3 the equilibrium is in the overlap region, and the gear at the equilibrium depends on the initial states.

In practice, the BSFC map is usually close to a quadratic function with one minimum point, and it can be checked that for a quadratic BSFC function Assumption 1 holds. As will be shown below, this assumption is essential to prove the stability of a gear switch schedule, so one shall generate a 2-neighbor ε-partition in the (v, u)-plane even when the BSFC is more complicated. Based on all definitions, lemmas and assumptions, we are now ready to present the main theorem.

Theorem 1. *If Assumption 1 and Lemmas 1, 2, 3 hold, the trajectories will approach the equilibrium while having finitely many gear changes.*

The details of the proof are given in Section 3.3.2. The idea behind the proof is to categorize all different cases and show stability of the system (3.13), respectively. All the three different possibilities are shown in Figure 3.6, where initial conditions are denoted by brown crosses, the equilibrium is denoted by black dot, and different line styles of the trajectories indicate different gears. We emphasize again that the stability of system (3.13) requires implicitly the fact the gear shift schedule (3.19,3.20) gives a 2-neighbor ε-partition in the (v, u)-space.

We remark that stability of system (3.13) with certain gear shift schedule does not require specific structure of the controller. The proof of Theorem 1 relies only on the fact that the equilibrium of the controlled system in (v, u)-space is stable. Therefore, the gear shift schedule design may be generalized to more general and nonlinear controllers, such as those presented in [44] [52].

3.3.1 Proof of Lemma 3

We will prove the lemma in two steps. First, we show that without constraints the equilibrium (3.9) is stable. Second we show that adding (3.21,3.22,3.24), the constrained working region (3.26) is still invariant and the equilibrium (3.9) is still stable. Note that for a given v^*, equilibrium (3.9) is unique.

Defining the perturbations

$$\begin{aligned} \tilde{v} &= v - v^*, \\ \tilde{u} &= u - u^*, \end{aligned} \tag{3.28}$$

(3.8) can be re-written as

$$\begin{aligned} \dot{\tilde{v}} &= -f(\tilde{v} + v^*) + \tilde{u} + u^*, \\ \dot{\tilde{u}} &= -K_{\mathrm{P}}\big(- f(\tilde{v} + v^*) + \tilde{u} + u^*\big) - K_{\mathrm{I}}\tilde{v}\,. \end{aligned} \tag{3.29}$$

Choosing the Lyapunov function

$$V(\tilde{v}, \tilde{u}) = \frac{1}{2}K_{\mathrm{I}}\tilde{v}^2 + \frac{1}{2}(\tilde{u} + K_{\mathrm{P}}\,\tilde{v})^2\,, \tag{3.30}$$

with $K_{\mathrm{I}} > 0$, $K_{\mathrm{P}} > 0$, we obtain the Lie derivative

$$\begin{aligned} \dot{V}(\tilde{v}, \tilde{u}) &= K_{\mathrm{I}}\tilde{v}\dot{\tilde{v}} + (\tilde{u} + K_{\mathrm{P}}\tilde{v})(\dot{\tilde{u}} + K_{\mathrm{P}}\dot{\tilde{v}}) \\ &= K_{\mathrm{I}}\big(- f(\tilde{v} + v^*) + f(v^*)\big)\tilde{v} - K_{\mathrm{I}}K_{\mathrm{P}}\tilde{v}^2 \\ &= K_{\mathrm{I}}\big(- f'(\xi) - K_{\mathrm{P}}\big)\tilde{v}^2\,. \end{aligned} \tag{3.31}$$

In the last step, the mean value theorem is applied to f assuming $v > 0$, which ensures that there exists ξ satisfying

$$f(\tilde{v} + v^*) - f(v^*) = f'(\xi)\tilde{v}, \tag{3.32}$$

where $\xi = \xi(\tilde{v}) > 0$. Thus, (3.31) is negative semi-definite when $v > 0$. Applying the LaSalle-Krasovskii invariance principle, it can be shown that the largest invariant set within $\dot{V} = 0$ is $(\tilde{v}, \tilde{u}) = (0, 0)$. Therefore, the equilibrium is asymptotically stable.

Next we show that in the presence of state constraints (3.24) and control constraints (3.21,3.22), the stability of the equilibrium can still be guaranteed. We show that the dynamics can be maintained along boundaries $v = 0$, $u = u_{\min}$, $u = u_{\max}$, and $m_{\mathrm{eff}}uv = P$, and that when a trajectory enters one of these boundaries (at time t_{en}) and leaves it (at time t_{ex}), then the Lyapunov function decreases between t_{in} and t_{ex}. We first determine the dynamics along the boundaries and determine the exit points $(v(t_{\mathrm{ex}}), u(t_{\mathrm{ex}}))$. Then we show

that the Lyapunov function (3.30) decreases while traveling along the boundary arcs, by comparing $v(t_{\rm ex}) - v^*$ with $v(t_{\rm en}) - v^*$, and $u(t_{\rm ex}) - u^*$ with $u(t_{\rm en}) - u^*$.

3.3.1.1 Along $v = 0$

Below the nullcline $u = f(v)$ we have $\dot{v} < 0$ while above it we have $\dot{v} > 0$; see Figure 3.5. Corresponding to this, a trajectory can only enter the $v = 0$ boundary below the point where the nullcline intersects it (marked as a black plus in Figure 3.5), i.e., $u(t_{\rm en}) < f(0) = \gamma g$. Along this section, we have $\dot{v} = 0$ and $\dot{u} = K_{\rm I} v^* > 0$ according to the dynamics (3.8). That is, the trajectory keeps traveling upward on $v = 0$ until it reaches the nullcline at $t_{\rm ex}$ where $u(t_{\rm ex}) = f(0) = \gamma g$. Comparing the states at $t_{\rm en}$ and $t_{\rm ex}$, we have $v(t_{\rm en}) = v(t_{\rm ex}) = 0$ and $u(t_{\rm en}) < u(t_{\rm ex}) < u^*$, which imply

$$\begin{aligned} &|v(t_{\rm ex}) - v^*| = |v(t_{\rm en}) - v^*|, \\ &|u(t_{\rm ex}) - u^*| < |u(t_{\rm en}) - u^*|, \\ &(u(t_{\rm ex}) - u^*)\,(v(t_{\rm ex}) - v^*) < (v(t_{\rm en}) - v^*)\,(u(t_{\rm en}) - u^*)\,. \end{aligned} \tag{3.33}$$

Substituting these into the Lyapunov function (3.30), we obtain

$$V(\tilde{v}(t_{\rm ex}), \tilde{u}(t_{\rm ex})) < V(\tilde{v}(t_{\rm en}), \tilde{u}(t_{\rm en})), \tag{3.34}$$

that is, the Lyapunov function decreases while the trajectory travels along the $v = 0$ boundary.

3.3.1.2 Along $v = v_{\max}$

According to the definition (3.25), the $v = v_{\max}$ boundary is located below the $u = f(v)$ nullcline, yielding $\dot{v} < 0$. This means that no trajectory enters this boundary.

Before discussing the remaining three boundaries we remark that according to the control constraints (3.21,3.22) and the monotonicity condition (3.10), we have

$$u_{\min} < f\,(v) < \min\left\{u_{\max}, \frac{P_{\max}}{v}\right\}, \tag{3.35}$$

in the domain $0 < v < v_{\max}$; cf. (3.24).

3.3.1.3 Along $u = u_{\min}$

On the right side of the nullcline $u = \frac{K_{\rm I}}{K_{\rm P}}(v - v^*) + f(v)$, we have $\dot{u} < 0$ while on the left side of it we have $\dot{u} > 0$. That is, a trajectory can enter the $u = u_{\min}$ boundary on

the right side of the nullcline. After traveling left along the boundary, it exits where the nullcline intersects the boundary; cf. see black plus in Figure 3.5. Consequently, we have $v(t_{\text{ex}}) < v(t_{\text{en}})$ and $u(t_{\text{ex}}) = u(t_{\text{en}}) = u_{\min}$.

However, in order to show that the Lyapunov function decreases while traveling along the boundary, additional arguments are needed. The normal unit vector to this boundary (pointing outbound) is given by $\mathbf{n}_{\min} = [0, -1]^{\mathrm{T}}$. According to (3.8), when $u \equiv u_{\min}$, the vector field is given by $\mathbf{t}_{\min} = [-f(v) + u_{\min},\ -K_{\mathrm{P}}(-f(v) + u_{\min}) + K_{\mathrm{I}}(v^* - v)]^{\mathrm{T}}$. Then staying on the boundary corresponds to

$$\mathbf{t}_{\min} \cdot \mathbf{n}_{\min} = K_{\mathrm{P}}\left(-f(v) + u_{\min}\right) + K_{\mathrm{I}}(v - v^*) > 0, \tag{3.36}$$

which holds on the right of the point where nullcline intersects the boundary, and it becomes zero at the intersection point. That is, using (3.35,3.36), we have $v(t_{\text{ex}}) > v^*$. Moreover, using $u \equiv u_{\min} \Rightarrow \tilde{u} < 0 \Rightarrow \dot{u} = \dot{\tilde{u}} = 0$, $\dot{v} = \dot{\tilde{v}} < 0$ and (3.10,3.28,3.35,3.36) in (3.31) we obtain the Lie derivative

$$\dot{V}(\tilde{v}, \tilde{u}) = \dot{v}\big((K_{\mathrm{I}} + K_{\mathrm{P}}^2)\tilde{v} + K_{\mathrm{P}}\tilde{u}\big). \tag{3.37}$$

Using the fact that $\dot{v} < 0, \tilde{v} > 0, K_{\mathrm{P}} > 0$ and $\tilde{u} = -f(v^*) + u_{\min} > -f(v) + u_{\min}$, we have

$$\begin{aligned} \dot{V}(\tilde{v}, \tilde{u}) &< \dot{v}\big(K_{\mathrm{I}}\tilde{v} + K_{\mathrm{P}}(-f(v^*) + u_{\min})\big) \\ &< \dot{v}\big(K_{\mathrm{I}}\tilde{v} + K_{\mathrm{P}}(-f(v) + u_{\min})\big) = \dot{v}\left(\mathbf{t}_{\min} \cdot \mathbf{n}_{\min}\right) < 0. \end{aligned} \tag{3.38}$$

That is, the Lyapunov function decreases along the $u = u_{\min}$ boundary.

Note that it is possible that the nullcline intersects the $u = u_{\min}$ boundary at $v > v_{\max}$. In such case, no trajectory enters the boundary $u = u_{\min}$.

3.3.1.4 Along $u = u_{\max}$

This boundary can be handled similar to the $u = u_{\min}$ boundary. A trajectory may enter the boundary on the left side of the nullcline, and after traveling right, it exits where the nullcline intersects the boundary; cf. black plus in Figure 3.5. Consequently, we have $v(t_{\text{ex}}) > v(t_{\text{en}})$ and $u(t_{\text{ex}}) = u(t_{\text{en}}) = u_{\max}$.

Similar to the $u = u_{\min}$ boundary, it can be shown that the Lyapunov function decreases when the trajectory travels along the boundary. The normal unit vector to this boundary (pointing outbound) is given by $\mathbf{n}_{\max} = [0, 1]^{\mathrm{T}}$. According to (3.8), along the $u = u_{\max}$ boundary, the vector field is given by $\mathbf{t}_{\max} = [-f(v) + u_{\max}, -K_{\mathrm{P}}(-f(v) + u_{\max}) +$

$K_{\mathrm{I}}(v^* - v)]^{\mathrm{T}}$, yielding

$$\mathbf{t}_{\max} \cdot \mathbf{n}_{\max} = -K_{\mathrm{P}} \left(-f(v) + u_{\max}\right) - K_{\mathrm{I}}(v - v^*) > 0. \tag{3.39}$$

This holds only on the left of the point where nullcline intersects the boundary, and it becomes zero at the intersection point. That is, using (3.35,3.39), we have $v^* > v(t_{\mathrm{ex}}) > v(t_{\mathrm{en}})$ and $u(t_{\mathrm{ex}}) = u(t_{\mathrm{en}}) = u_{\max}$. When traveling along the boundary, the Lie derivative is same as (3.38) and again using (3.10,3.28,3.35,3.39) one can show that it is negative, i.e., the Lyapunov function decreases along the $u = u_{\min}$ boundary.

Note that it is possible that the nullcline intersects the $u = u_{\max}$ boundary at $v > v_{\mathrm{switch}}$ (cf. (3.23)) or $v < 0$. In the former case, the no trajectory enters the $u = u_{\max}$ boundary. The later case implies that no trajectory exits within $[0, v_{\mathrm{switch}}]$, but continues to travel along the boundary $m_{\mathrm{eff}}uv = P_{\max}$, which will be handled below.

3.3.1.5 Along $m_{\mathrm{eff}}uv = P_{\max}$

This boundary can only be entered when $v \geq v_{\mathrm{switch}}$ (cf. (3.23)), and we have $\dot{v} > 0$ since this boundary is above the nullcline $u = f(v)$. We denote $\bar{P} = \frac{P_{\max}}{m_{\mathrm{eff}}}$ in the rest of proof for compact description. Note that this boundary is neither horizontal nor vertical. Consequently, one cannot use the nullcline to determine where this trajectory exits the boundary. The normal vector to this boundary pointing outbound is given by $\mathbf{n}_P = [\frac{\bar{P}}{v^2}, 1]^{\mathrm{T}}$, while vector field is given by $\mathbf{t}_P = [-f(v) + \bar{P}/v, -K_{\mathrm{P}}(-f(v) + \bar{P}/v) + K_{\mathrm{I}}(v^* - v)]^{\mathrm{T}}$; cf. (3.8). In order to stay along the boundary, we need

$$(\mathbf{t}_P \cdot \mathbf{n}_P)(v) = \left(\frac{\bar{P}}{v^2} - K_{\mathrm{P}}\right)\left(-f(v) + \frac{\bar{P}}{v}\right) - K_{\mathrm{I}}(v - v^*) > 0. \tag{3.40}$$

This requires that $v_{\mathrm{switch}} < v < v^*$, otherwise, due to (3.27) and (3.35), both terms in (3.40) are negative. Indeed, to enter the boundary, we need $(\mathbf{t}_P \cdot \mathbf{n}_P)\big(v(t_{\mathrm{en}})\big) > 0$ while at the exit point $(\mathbf{t}_P \cdot \mathbf{n}_P)\big(v(t_{\mathrm{ex}})\big) = 0$.

In fact, if K_{P}, K_{I} satisfy (3.27), there exists $\bar{v} \in (0, v_{\mathrm{switch}})$ such that $K_{\mathrm{P}}\bar{v}^2 - \bar{P} = 0$, so $(\mathbf{t}_P \cdot \mathbf{n}_P)(\bar{v}) = K_{\mathrm{I}}(v^* - \bar{v}) > 0$. On the other hand, due to (3.27) and (3.35), $(\mathbf{t}_P \cdot \mathbf{n}_P)\big(v\big) < 0$ for all $v \geq v^*$. Thus, there exists $v \in (\bar{v}, v^*)$ such that $(\mathbf{t}_P \cdot \mathbf{n}_P)(v) = 0$; cf. the black plus on the curve $uv = \bar{P}$ in Figure 3.5. Recall that v is increasing along the boundary. Using (3.10,3.35) we have $v(t_{\mathrm{en}}) < v(t_{\mathrm{ex}}) < v^*$. Using (3.10,3.28) in (3.31), the Lie derivative becomes

$$\dot{V}(\tilde{v}, \tilde{u}) = K_{\mathrm{I}}\tilde{v}\left(-f(v) + u^*\right) - K_{\mathrm{P}}K_{\mathrm{I}}\tilde{v}^2 < -K_{\mathrm{P}}K_{\mathrm{I}}\tilde{v}^2 < 0. \tag{3.41}$$

That is, the Lyapunov function decreases along the $uv = \bar{P}$ boundary.

Note that $(\mathbf{t}_P \cdot \mathbf{n}_P)\big(v(t_{\text{ex}})\big) = 0$ may occur for $v(t_{\text{ex}}) < v_{\text{switch}}$. In this case the trajectory does not enter the $uv = \bar{P}$ boundary.

Therefore, we can conclude that if we choose $K_{\text{P}}, K_{\text{I}}$ according to (3.27), when traveling along boundary arcs, the value of the Lyapunov function decreases. This, together with that the Lyapunov function decreases along the trajectories in the interior, the equilibrium (3.9) is asymptotically stable.

3.3.2 Proof of Theorem 1

Recall (3.28) and let us denote working region of engine in $(\tilde{v}, \tilde{u})$-space as $\mathcal{X}$ (cf. (3.26)). Using Lemma 2 and Assumption 1, a 2-neighbor ε-partition is generated by gear change as $\bigcup_{i=1}^{N} P^{\text{N}\varepsilon}$ over $(\tilde{v}, \tilde{u})$-space. We define $Q_{i,j}^{\text{N}\varepsilon} = P_i^{\text{N}\varepsilon} \bigcap P_j^{\text{N}\varepsilon}$. The initial states are $(\tilde{v}_0, \tilde{u}_0)$ at $t = 0$. According to Lemma 3, the trivial equilibrium of (3.29) is asymptotically stable. Define the domain $D_\delta = \{(\tilde{v}, \tilde{u}) \,|V(\tilde{v}, \tilde{u}) \leq \delta\} \bigcap \mathcal{X}$, where V is the Lyapunov function (3.30). Below we use the abbreviated notation $D_{V(\tilde{v}_0, \tilde{u}_0)}$, by which we mean D_δ with $\delta = V(\tilde{v}_0, \tilde{u}_0)$. Without loss of generality, we assume that the equilibrium (v^*, u^*) is located in $P_i^{\text{N}\varepsilon}$, while the initial state $(\tilde{v}_0, \tilde{u}_0)$ can be in any gear. Then there are three possibilities. The trajectories of all the possibilities are illustrated in Figure 3.6 by brown curves with gear engaged implied by line styles, where initial conditions are denoted by brown crosses while equilibrium is denoted by black dots.

1. The equilibrium is located in a non-overlap region (i.e., $(v^*, a_{\text{d}}^*) \notin Q_{i,j}^{\text{N}\varepsilon}, \forall\, j \neq i$), and the initial state $(\tilde{v}_0, \tilde{u}_0) \in D_{V(\tilde{v}_0, \tilde{u}_0)} \subseteq P_i^{\text{N}\varepsilon}$. If $(\tilde{v}_0, \tilde{u}_0) \in P_i^{\text{N}\varepsilon} \bigcap P_j^{\text{N}\varepsilon}$ where $j \in N_i$, and the system starts in the j-th gear, then one gear change will happen and the trajectory settles to the i-th gear, yielding a stable equilibrium. If, instead, the system starts in the i-th gear, then no gear change will happen while the trajectory approaches the equilibrium. The corresponding trajectory is shown in Figure 3.6, denoted by case 1.

2. The equilibrium is located in an non-overlap region, but the trajectory travels through different regions, that is $D_{V(\tilde{v}_0, \tilde{u}_0)} \bigcap P_j^{\text{N}\varepsilon} \backslash Q_{i,j}^{\text{N}\varepsilon} \neq \emptyset$, $\exists j \neq i$. In this case multiple gear shifts may occur. By Assumption 1 there is a non-zero dwell time between two consecutive gear shifts. Then $\exists\, T > 0$ such that $\forall\, t > T$, $D_{V(\tilde{v}(t), \tilde{u}(t))} \subseteq P_i^{\text{N}\varepsilon}$. Since T is finite, it will enter and leave $P_j^{\text{N}\varepsilon}, \forall j \neq i$ only finite times. The corresponding trajectories are shown in Figure 3.6, denoted by case 2. Therefore the gear will still settle down to the i-th gear and the equilibrium will be stable.

3. The equilibrium is located in an overlap region, i.e., $\exists j \in N_i$ such that $(v^*, u^*) \in Q_{i,j}^{\mathrm{N}\varepsilon}$. If $D_{V(\tilde{v}_0,\tilde{u}_0)} \subset Q_{i,j}^{\mathrm{N}\varepsilon}$, the states converge to the equilibrium without changing gears and the equilibrium is stable. The final gear will be the same as the initial gear, and thus could be either i-th or j-th. If $D_{V(\tilde{v}_0,\tilde{u}_0)} \not\subset Q_{i,j}^{\mathrm{N}\varepsilon}$, then $\exists T > 0$ such that $\forall t > T$, $D_{V(\tilde{v}(t),\tilde{u}(t))} \subseteq Q_{i,j}^{\mathrm{N}\varepsilon}$. Since T is finite, the trajectory will enter and leave $P_j^{\mathrm{N}\varepsilon}, (j \neq i)$ only finite times. Therefore, the gear will still settle down at the same gear as $\big(\tilde{v}(T), \tilde{u}(T)\big)$ (also could be either i or j). The corresponding trajectories are shown in Figure 3.6, denoted by case 3.

3.4 Application Of The Gear Shift Schedule Design For A Heavy-Duty Vehicle

In this section we apply the proposed method to the gear shift schedule design of a class 8 truck. In particular, we consider a Prostar truck manufactured by Navistar that is equipped with a MaxxForce 13 liter diesel engine and a 10 speed automated manual transmission. The parameters for the vehicle are given in Table 2.1. The gear ratios η_i in (3.16) are given by the corresponding value in Table 2.1 times the final drive ratio. Similar to the gear ratio,

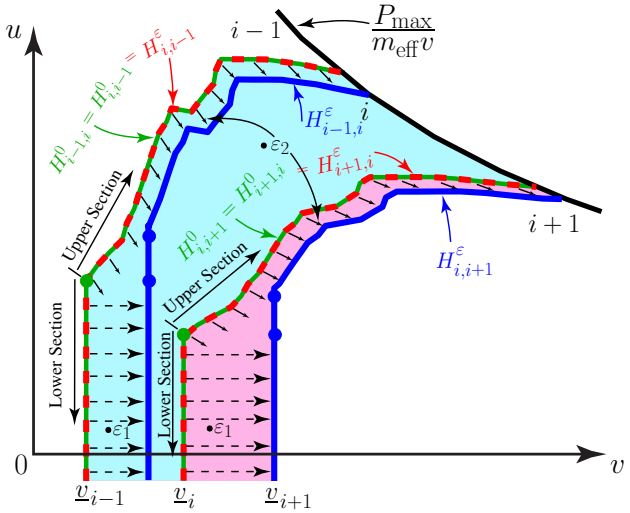

Figure 3.7: The procedure of generating the 2-neighbor ε-partition gear shift schedule from the ideal shift curves (green). Through the indicated shifting using ε_1 and ε_2, the actual upshift (blue) and downshift (red dashed) curves are obtained.

the efficiency is calculated by the corresponding number in Table 2.1 times the efficiency of the final drive. During simulations, the mild difference in efficiency of torque delivery at

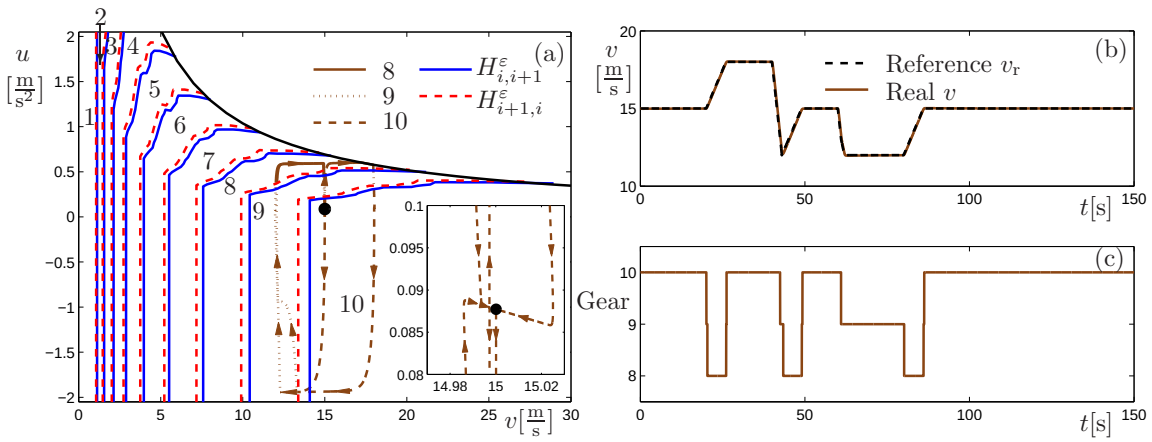

Figure 3.8: Performance of the system (3.13) with the gear shift schedule (3.19,3.20). (a) Trajectory in the (v, u)-space, with the corresponding gear indicated by the line styles. (b) Time profiles of the reference speed v_r and the vehicle speed v. (c) Time profile of the gear.

different gears is also taken into account. We also set $P_{\max} = 330$ [kW], $u_{\max} = 2[\mathrm{m/s^2}]$, and $u_{\min} = -2[\mathrm{m/s^2}]$, yielding $v_{\max} = 40.70[\mathrm{m/s}]$.

Using the proposed gear shift schedule design, the ideal shift curves $H^0_{i,i+1} = H^0_{i+1,i}$ and $H^0_{i,i-1} = H^0_{i-1,i}$ are shown as green solid curves in Figure 3.7. Note that each $H^0_{i,i+1}$ consists of two sections. The vertical line at the bottom up to blue dot is resulted from the low engine speed limit, i.e., $\underline{v}_i = \underline{\omega}_e \eta_i / R$. We refer to this section as the lower section. The rest of the curve $H^0_{i,i+1}$ is called the upper section. To generate a 2-neighbor ε-partition in the (v, u)-space, we shift the ideal curve $H^0_{i,i+1}$ to the right in order to get the upshift curve $H^\varepsilon_{i,i+1}$, while keep downshift curve as $H^\varepsilon_{i+1,i} = H^0_{i+1,i}$. The curve $H^\varepsilon_{i,i+1}$ is obtained in three steps. First, the lower section of $H^0_{i,i+1}$ is shifted to the right with ratio ε_1, that is, from $H^0_{i,i+1}$ to $H^0_{i,i+1} + \varepsilon_1(H^0_{i+1,i+2} - H^0_{i,i+1})$, as shown by the black dashed arrows in Figure 3.7. Second, the upper section of the new $H^0_{i,i+1}(v, u)$ is shifted along iso-power curves, that is from $H^0_{i,i+1}(v, u) = 0$ to $H^0_{i,i+1}\big((1+\varepsilon_2)v, u/(1+\varepsilon_2)\big) = 0$, as shown by the black solid arrows in Figure 3.7. Finally, the upshift curve $H^\varepsilon_{i,i+1}$ is generated by extending the lower section toward the upper section as shown by the blue curve in Figure 3.7. The downshift curves are shown as red dashed curves and they coincide with the ideal green curves.

All upshift and downshift curves are shown in the (v, u)-space in Figure 3.8a when choosing $\varepsilon_1 = 0.15$ and $\varepsilon_2 = 0.05$. Indeed, a 2-neighbor ε-partition in (v, u)-space is generated, so Assumption 1 holds and thus the stability of (3.13) is guaranteed by Theorem 1. We remark that larger ε-s lead to better drivability in traditional sense [55], as they make the vehicle stay at a lower gear compared to the ideal design, making the maximum available power larger at a given speed. On the other hand, increasing ε-s pushes the design

away from the ideal curves and thus, lowers the fuel economy. Thus, the ε-s can be used for tuning between fuel economy and drivability.

Numerical simulations are carried out to show the effectiveness of the proposed design. The feedback gains in (3.8) are set to $K_{\mathrm{I}} = 0.5[1/\mathrm{s}^2]$ and $K_{\mathrm{P}} = 6[1/\mathrm{s}]$. As the condition of Lemma 3 holds, stability of the equilibrium is guaranteed. The simulation uses time step 0.01[s], and the gear shift decision made at each time step is applied in the next step. In Figure 3.8b, we first show the case where controller (3.6) tries to follow a test cycle marked as a black dashed curve. The resulted time profile of the speed is shown by the solid brown curve in Figure 3.8b while the time profile of the gear engaged is displayed in Figure 3.8c. In the last part of the cycle, the reference speed is set as a constant $v_{\mathrm{r}} = 15[\mathrm{m/s}]$, and the vehicle speed approaches this equilibrium. The corresponding trajectory is plotted in the (v, u)-plane in Figure 3.8a, with the gear engaged indicated by line type.

Next we simulate cases where controller (3.6) is used to follow real driving cycles. In particular, we use two different EPA driving cycles, the heavy duty urban dynamometer driving schedule (HUDDS) cycle and the New York City (NYC) cycle, shown as black dashed curves in Figure 3.9 a, b, d and e, respectively. We compare the results using the proposed gear shift map and the in-production gear shift map implemented in the Navistar Prostar. The time evolution of the speed is shown in Figure 3.9a and d for the optimal design (brown curves) and in Figure 3.9b and e for the in-production benchmark design (red curves), while the corresponding gear profiles are shown in Figure 3.9c and f. The fuel performance and tracking performance are summarized in Table 3.1. In both cases, the controller manages to follow the reference speed closely, but the proposed gear shift map can achieve better tracking performance with less fuel consumption.

However, frequent gear changes with the proposed optimal design can be seen, especially for the HUDDS cycle. For the HUDDS cycle, downshift at high speed happens when a large acceleration is needed, while for the NYC cycle, the frequent change is caused by both large deceleration and large acceleration.

With traffic information available, an automated vehicle may plan the torque demand, so large variation of the torque demand can be avoided [16]. As an example, we filtered the original driving the HUDDS and the NYC cycles using an moving average filter of window size 5 [s], and fed the filtered cycle to the controller. This mimics a predictive controller for an automated vehicle with prediction window of 2.5 [s]. The time profiles of the speed and the gear of the filtered cycles are shown in Figure 3.10 a,b,d and e as dashed blue curves. For filtered cycles, the controller still manages to follow the reference speed closely as shown by the brown and red curves. The corresponding gear profiles in Figure 3.10 c and f show that by providing a smoother speed profile (and therefore requiring lower torque),

Optimal/Benchmark design	HUDDS	NYC
Fuel economy [MPG]	4.66/4.60	2.68/2.60
Maximum tracking error [m/s]	1.10/1.22	1.72/1.91
Average tracking error [m/s]	0.046/0.048	0.079/0.082

Table 3.1: Fuel consumption and tracking performance comparison between proposed design and in-production benchmark design while following the original driving cycles

frequent gear changes can be avoided. In Table 3.2, the fuel consumption and the tracking performance are summarized for the cases when the truck tries to follow the filtered cycle. It can be seen that a large improvement in fuel economy is achieved by filtering without

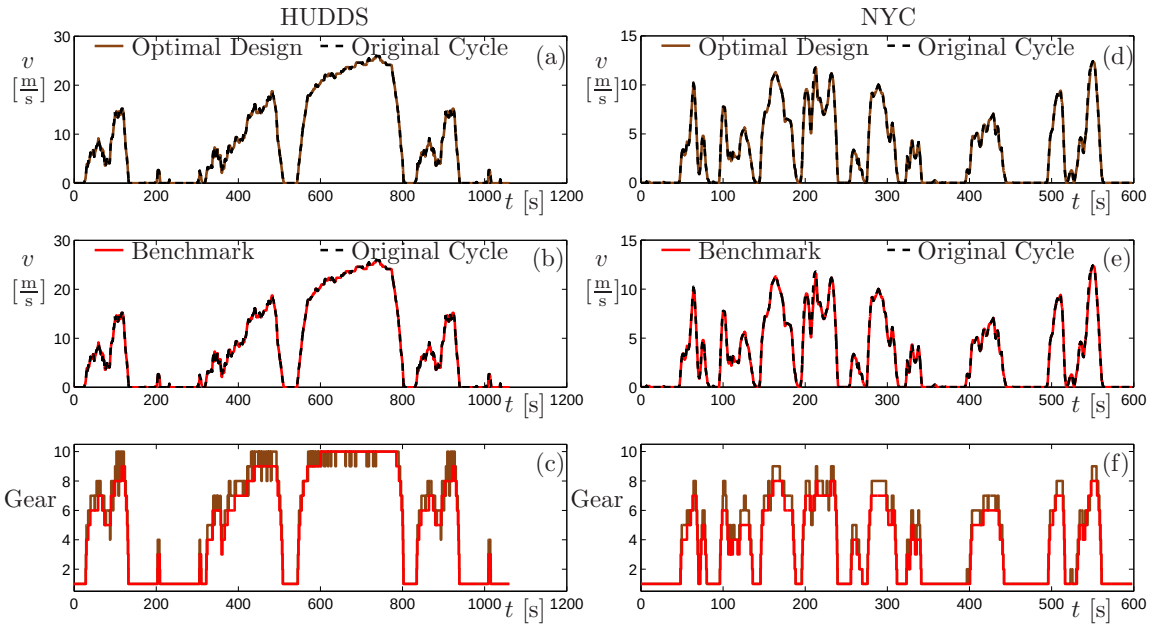

Figure 3.9: Performance of the system (3.13) with proposed gear shift schedule while following different driving cycles. The top and middle rows show the speed profiles of both optimal design (brown) and in-production benchmark design (red) while following the driving cycle (dashed black). The bottom row shows the corresponding gear profiles.

creating a noticeable difference in the tracking error. The improvement of the proposed design over in-production design becomes more significant. These imply that by integrating the proposed gear shift design with proper speed profile planning, the automated vehicle could be driven both safely and fuel-efficiently. To sum up, our framework guarantees the stability and efficiency of propulsion system, and enables further improvement in fuel economy with driving cycle planning for an automated vehicle, while achieving better fuel performance.

Optimal/Benchmark design	HUDDS	NYC
Fuel economy [MPG]	5.44/5.23	3.17/3.00
Maximum tracking error compared to filtered cycle [m/s]	0.28/0.29	0.48/0.80
Average tracking error compared to filtered cycle [m/s]	0.027/0.027	0.052/0.054
Maximum tracking error compared to original cycle [m/s]	1.19/1.19	1.73/1.72
Average tracking error compared to original cycle [m/s]	0.122/0.122	0.196/0.198

Table 3.2: Fuel consumption and tracking performance comparison between proposed design and in-production benchmark design while following the filtered driving cycles

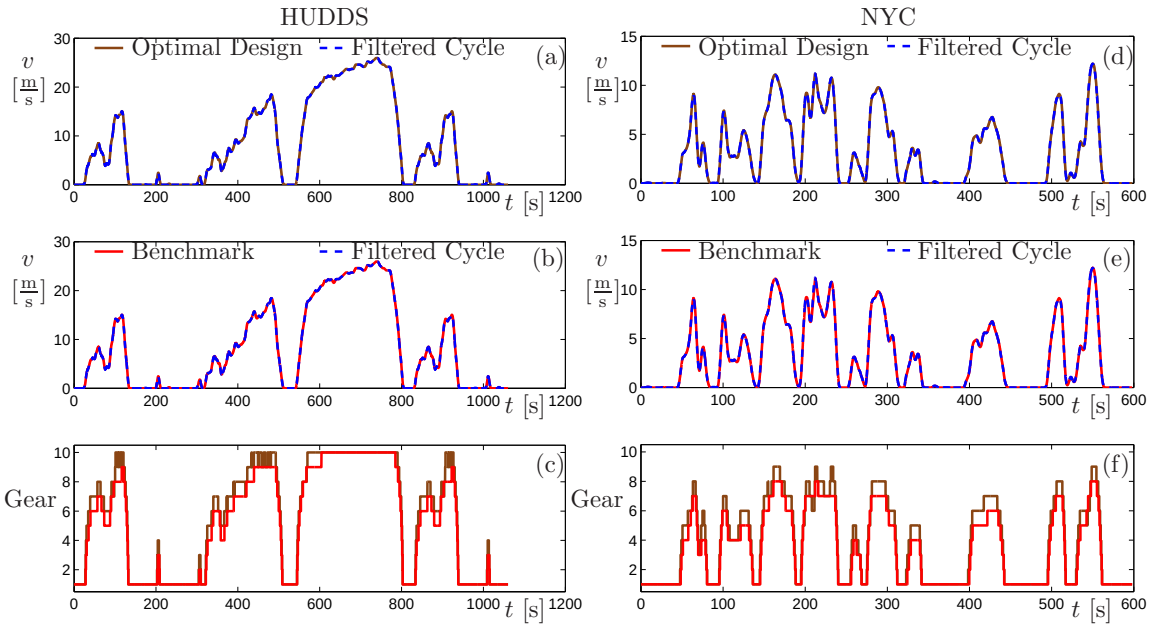

Figure 3.10: Performance of the system (3.13) with proposed gear shift schedule while following filtered cycles. The top and middle rows show the speed profiles of both optimal design (brown) and in-production benchmark design (red) while following the filtered cycles (dashed blue). The bottom row shows gear profiles corresponding to the two difference speed profiles.

3.5 Summary

In this chapter, we proposed a gear shift schedule design primarily intended for automated vehicles. We used Lyapunov arguments to prove the stability of equilibrium of the underlying constrained hybrid dynamical systems in the presence of constraints. Our design guarantees that the torque demand is delivered at the most fuel efficient gear, that is, fuel economy is improved without compromising drivability. It was shown that further im-

provements in fuel economy can be achieved by requesting smoother speed profile through automation.

Using the proposed design, one would have a safe and fuel-efficient powertrain. With such powertrain, it is possible to design a fuel-efficient driving profile that optimally use the powertrain. This will be discussed in Chapter 4.

CHAPTER 4

Analytical Approach for Fuel Optimal Control

First get the physics right. The rest is mathematics.

RUDOLPH E. KALMAN

Using the results of previous section In the previous chapter, an automated powertrain system can be acquired. Based on such powertrain, in this chapter, we design eco-driving systems that generate fuel-efficient driving profile based on elevation obtained via connectivity.

Eco-driving problem can be formulated as optimal control problems. These problems, however, contain many parameters that may be fixed to some reasonable values and then the problems can be solved using particular methods of choice. However, a thorough and systematic study on how the optimal solution changes when the parameters are varied is not available in the literature. Since the performance of the optimal controller depends heavily on the parameter values, understanding how to tune the parameters is as important as understanding the design framework. In this chapter, we use analytical and numerical tools from bifurcation theory to investigate the effects of parameter variations on optimal control problems. This allows us to determine regions in the parameter space with qualitatively different dynamics and control actions and quantify the trade-off between different control goals in the different regions.

We start with a modeling framework that allows one to optimize the driving profile to achieve better fuel economy given the elevation profile, headwind, and traffic information along the route. We also take into account the desired terminal time leading to a multi-objective optimal control problem. Then, we present a systematic approach to analyze the optimal control trajectory for fuel efficient driving while varying parameters and quantify the trade-offs in different parameter regions. We convert the resulting optimal control problem to a boundary value problem (BVP) by using Pontryagin's Maximum Principle

(PMP). We first solve a simplified BVP analytically and then use numerical continuation to gradually change the parameters until the solution to the original nonlinear problem is reached. Also, in order to avoid the sensitivity to initial conditions, we use collocation to solve the BVP that is embedded in our pseudo-arclength numerical continuation program. This allows us to increase the computational speed by distributing the sensitivity along the trajectory while reacting to changing parameters.

Mathematically, we need to deal with an optimal control problem that involves mixed state-control constraints and singular arcs. Optimal control problems with mixed constraints are challenging due to the non-smooth and non-continuous nature of the problem [68]. Necessary optimality conditions for this class of control problems can be found in [69–72]. In our problem, the control variable appears linearly in the dynamics and cost functional. Then, in view of PMP, the optimal control is a concatenation of bang-bang and singular arcs, which makes it difficult to generate numerical solutions. In [73], mixed control-state constraints were handled using saturation functions which can tolerate the discontinuity to some extent. In [74], numerical continuation was used to study the optimal solution while varying parameters in (smooth) optimal control problems occurring in biomedical imaging. Inspired by these works, in this chapter we use the analytical solution of a simplified (linear damped) system to characterize the switching structure between different arcs while varying parameters. This allows us to identify the structure of the optimal controller that may switch between different "bang-bang" and "bang-singular-bang" scenarios as parameters vary. Moreover, using the analytical solution to initialize the numerical continuation allows us to speed up the solution process.

The rest of the chapter is organized as follows. The optimal control problem is formulated in Section 4.1, and the necessary condition for optimal trajectories is presented in Section 4.2. We generate the analytical solution of a corresponding linear system in Section 4.3 that is used to initialize the numerical solver discussed in Section 4.4. We analyze the optimal solution with respect to the change of traffic condition in Section 4.5. Finally, we summarize this chapter in Section 4.6.

4.1 Optimal Control Formulation

In this section we lay out a modeling framework that is used to optimize fuel economy of HDVs. This framework allows the use of different models to describe the vehicle dynamics, a wide variety of fuel consumption maps, and real-time traffic information.

4.1.1 Optimization Problem

Let us denote the distance (arc-length) traveled by the vehicle as s and the speed of the vehicle by v. The goal is to find the scalar input u that minimizes the objective function

$$J_0 = \int_0^{t_\mathrm{f}} q(v,u)\,\mathrm{d}t + \sigma_0\, t_\mathrm{f} + \int_0^{t_\mathrm{f}} r(v,s)\mathrm{d}t, \tag{4.1}$$

subject to the constraints

$$\begin{bmatrix}\dot{s}\\ \dot{v}\end{bmatrix} = \begin{bmatrix} v \\ f(s,v,u)\end{bmatrix}, \tag{4.2}$$

$$\begin{bmatrix}s(0)\\ v(0)\end{bmatrix} = \begin{bmatrix}0\\ v_0\end{bmatrix}, \qquad \begin{bmatrix}s(t_\mathrm{f})\\ v(t_\mathrm{f})\end{bmatrix} = \begin{bmatrix}s_\mathrm{f}\\ v_\mathrm{f}\end{bmatrix}, \tag{4.3}$$

$$0 \le u \le a_\mathrm{U}(v), \tag{4.4}$$

where the dot represents the derivative with respect to time t. The initial time is considered to be 0, while the terminal time is denoted by t_f and it is considered to be unknown.

The objective functional J_0 in (4.1) consist of three parts. The first terms represents the total fuel consumption, where the fuel consumption rate $q(v,u)$ is a function of the vehicle speed v and control input u. The second term $\sigma_0 t_\mathrm{f}$ represents the total cost corresponding to the terminal time t_f with weight σ_0. The third term is a penalty term related to traffic. It includes penalties related to the speed limits and traffic speed, as explained later.

The dynamic system (4.2) describes a longitudinal vehicle dynamics which will be specified below. The boundary conditions (4.3) fix the total arc-length of the route s_f, the initial speed v_0, and the final speed v_f, while (4.4) gives a speed-dependent upper bound for the control input u. To avoid braking (since it dissipates energy), we require the control input to be nonnegative, and assuming no safety hazard would occur.

4.1.2 Vehicle Dynamic Model

Recall the longitudinal vehicle model acquired from Chapter 2, we assume that no slip occurs on the wheels and that the flexibility of the tires and the suspension can be neglected. Then using the Newton-Euler equation we obtain

$$m_\mathrm{eff}\dot{v} = -m\,g\sin\phi - \gamma\,m\,g\cos\phi - k(v+v_\mathrm{w})^2 + \frac{\eta}{R}T_\mathrm{e}, \tag{4.5}$$

see [35,44], where the effective mass $m_{\text{eff}} = m + J_{\text{w}}/R^2$ contains the mass of the vehicle m, the moment of inertia J_{w} of the rotating elements, and the wheel radius R. For simplicity, this part only consider $J_{\text{e}} = 0$ in the design. Furthermore, g is the gravitational constant, ϕ is the inclination angle, γ is the rolling resistance coefficient, k is the air drag constant, v_{w} is the speed of the headwind, η is the gear ratio (that includes the final drive ratio and the transmission efficiency), and T_{e} is the engine torque. See Table 2.1 for parameter values used in this section, which are for a Prostar truck, a class 8 heavy duty vehicle manufactured by Navistar [1]. When units are not spelled out, quantities should be understood in SI units.

Based on (4.5), we have

$$f(s, v, u) = -\alpha \sin\phi - \beta \cos\phi - \kappa (v + v_{\text{w}})^2 + u, \tag{4.6}$$

in (4.2) where

$$\alpha = \frac{mg}{m_{\text{eff}}}, \quad \beta = \frac{\gamma mg}{m_{\text{eff}}}, \quad \kappa = \frac{k}{m_{\text{eff}}}, \quad u = \frac{\eta T_{\text{e}}}{m_{\text{eff}} R}. \tag{4.7}$$

Note that the control input u is a rescaled torque, with unit of acceleration $[\text{m/s}^2]$, and by choosing the appropriate gear ratio η one can calculate the corresponding engine torque T_{e}.

The inclination angle ϕ is calculated from the elevation profile $h(s)$ that gives the elevation as a function of the distance traveled s. Throughout this chapter, we consider a straight road with the simple elevation profile

$$h(s) = h_{\text{R}} \left(\frac{s - s_{\text{R}}}{s_{\text{R}}} \right)^2, \tag{4.8}$$

shown in Figure 4.1. We also consider $h_R \ll s_R$, in particular we use $h_{\text{R}} = 30$ [m], $s_{\text{f}} = 2s_{\text{R}} = 4000$ [m]. This profile is selected to enable the derivation of an analytical solution for the resulted optimal control problem in Section 4.3. Nonetheless, the methods presented can be applied when using other profiles as well. Since $\phi < 0.05$ [rad], here we use the approximation $\cos\phi \approx 1$. Moreover, for simplicity we consider no headwind $v_{\text{w}} = 0$. Thus, (4.6) can be simplified to

$$f(s, v, u) = -\alpha\, h'(s) - \beta - \kappa\, v^2 + u; \tag{4.9}$$

see Section 2.2.

We emphasize that using u as the control input enables us to decouple the optimization of the speed profile and the gear selection: the rescaled torque u is derived first and then the optimal gear is selected to minimize fuel consumption.

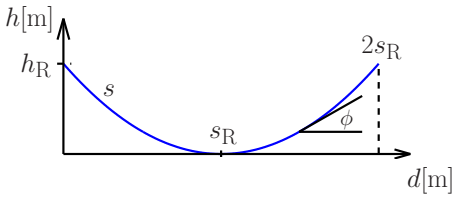

Figure 4.1: Elevation h as function of distance d and arc-lengths s.

4.1.3 Fuel Consumption Map with Gear Change

In order to keep the problem analytically tractable, we use a static fuel consumption map, $q(v,u)$ that specifies the fuel consumption rate (with unit [g/s]) for a given input u and a given speed v. Fuel consumption maps are typically given as a function of the engine speed ω_{e} and engine torque T_{e}, that is, $q(\omega_{\mathrm{e}}, T_{\mathrm{e}})$. Dividing this with the engine power $P_{\mathrm{d}} = T_{\mathrm{e}}\omega_{\mathrm{e}} = m_{\mathrm{eff}}uv$ we obtain the brake specific fuel consumption (BSFC):

$$\text{BSFC} = \frac{q(\omega_{\mathrm{e}}, T_{\mathrm{e}})}{T_{\mathrm{e}}\omega_{\mathrm{e}}} = \frac{q(v,u)}{m_{\mathrm{eff}}uv}, \tag{4.10}$$

where we used $u = \frac{\eta T_{\mathrm{e}}}{m_{\mathrm{eff}}R}$ and $v = \frac{R\omega_{\mathrm{e}}}{\eta}$; cf. (4.7). Small BSFC values typically imply good fuel economy [51]. Previous efforts on fuel economy optimization with analytical approach usually assumed fixed gear ratio, which resulted in a one-to-one relationship between $q(\omega_{\mathrm{e}}, T_{\mathrm{e}})$ and $q(v,u)$ [15,75]. In this chapter, we generate a map with the gear changes involved.

Given a control input u at a certain speed v, different gears set the engine to different working points, and therefore, yield different BSFC values. We choose the gear that gives the least BSFC among all the available gears and generate the working zone for each gear in the (v,u) plane as shown in Figure 4.2(a) for a MaxxForce 13 diesel engine with a 10-speed transmission used in a Prostar truck manufactured by Navistar [1]. Recall Chapter 3 for the optimal design. We found that for any given (v,u) point, there is a single optimal gear ratio, so one can map the fuel consumption from the $(\omega_{\mathrm{e}}, T_{\mathrm{e}})$-plane to the (v,u)-plane using the associated gear, which is shown by the contours in Figure 4.2(b). This corresponds to the optimal gear shift schedule in chapter 3. It can be observed that the contours of the fuel consumption map are similar to the iso-power curves ($P_{\mathrm{d}} = m_{\mathrm{eff}}uv$). To obtain an analytical model we fit the data using the Willans approximation

$$q(v,u) = p_2 v\, u + p_1 v + p_0, \tag{4.11}$$

see [76], where p_2, p_1, p_0 are parameters to be identified. By applying least squares fitting,

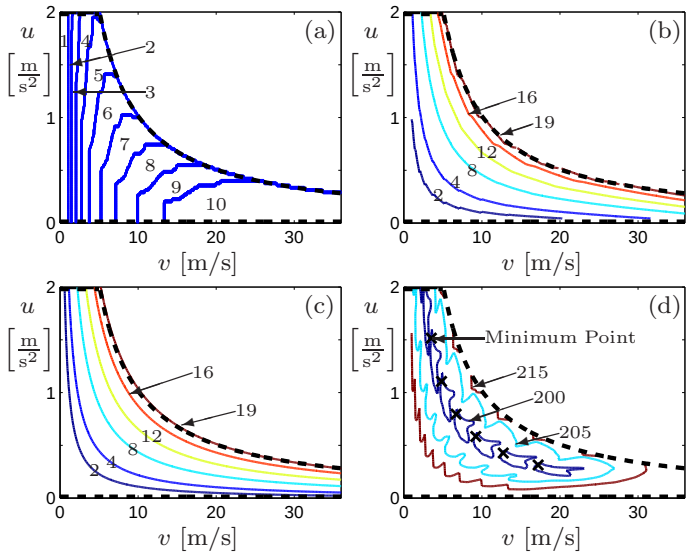

Figure 4.2: Contours in the plane of speed v and control input u. (a) Optimal gear ratios; (b) Experimental fuel consumption contours, with units $[\mathrm{g/s}]$; (c) Fitted fuel consumption contours, with units $[\mathrm{g/s}]$; (d) BSFC with optimal gear ratios applied, with units $[\mathrm{g/(kW \cdot h)}]$. The black crosses represent points with minimal BSFC value. In all four panels, black dashed curves indicate the boundaries of the domain accessible by the engine for all gears.

we obtain $p_2 = 1.8284 \pm 0.0019\,[\mathrm{gs^2/m^2}], p_1 = 0.0209 \pm 0.0006\,[\mathrm{g/m}], p_0 = -0.1868 \pm 0.0068\,[\mathrm{g/s}]$. The corresponding contours are shown in Figure 4.2(c). With the gear applied, the BSFC in (v, u)-plane is shown in Figure 4.2(d), where crosses indicate the minimal BSFC points for different gears.

We assume that gear changes occur instantaneously and the engine's state jumps along iso-power curves during gear change. The blank regions in Figure 4.2 correspond to (v, u) combinations that are not accessible by the engine. The corresponding black dashed boundary at the top consists of two sections: a constant section at $a_{\max}$ for low speeds and an iso-power curve at $P_{\max}$ for higher speeds. Since $P = T_{\mathrm{e}}\omega_{\mathrm{e}} = m_{\mathrm{eff}}uv$, we have

$$a_{\mathrm{U}}(v) = \min\{a_{\max}, U/v\}, \qquad U = \frac{P_{\max}}{m_{\mathrm{eff}}}, \tag{4.12}$$

in (4.4). In this chapter we use $a_{\max} = 2[\mathrm{m/s^2}]$, $P_{\max} = 300.65\,[\mathrm{kW}] \Rightarrow U = 10.14\,[\mathrm{m^2/s^3}]$ that are acquired through data fitting.

We rewrite the constraints (4.4,4.12) into the form

$$\begin{aligned} & 0 \leq \frac{u}{\min\{a_{\max},\, U/v\}} \leq 1 \\ \Leftrightarrow & \begin{cases} C_1(v,u) := \dfrac{u}{\min\{a_{\max},\, U/v\}} - 1 \leq 0, \\ C_2(v,u) := -\dfrac{u}{\min\{a_{\max},\, U/v\}} \leq 0. \end{cases} \end{aligned} \tag{4.13}$$

We note that the mixed constraint trivially satisfies the regularity condition $\partial_u C_i(v,u) \neq 0$, $i = 1, 2$. This guarantees the existence of Lagrange multipliers that is continuous over the whole time interval [77]. This will be supported by the derivation in the next section. Moreover, having the two constraints in a similar form results in multipliers of same scale, which is convenient for numerical computation.

4.1.4 Penalty on Traffic

We consider two types of penalty on traffic: one related to the speed limit, the other related to the traffic flow speed, that is, in (4.1) we consider

$$r(s,v) = r_1\big(v_{\lim}(s), v\big) + r_2\big(v_{\text{traf}}(s), v\big). \tag{4.14}$$

Here we assume the speed limit penalty is,

$$r_1\big(v_{\lim}(s), v\big) = \rho_1 \left\{ \sec\left[\frac{\pi}{2}\left(\frac{2v}{v_{\lim}(s)} - 1\right)^n\right] - 1 \right\}, \tag{4.15}$$

where the speed limit $v_{\lim}(s)$ is given along the route and as a function of the arc-length s and ρ_1 is a constant weight. The function (4.15) is illustrated in Figure 4.3(a), with $v_{\lim} \equiv 30\,[\mathrm{m/s}]$, $\rho_1 = 0.1[\mathrm{g/s}]$, for different values of n. It can be seen that as parameter n increases, the function becomes more "square shaped". In this chapter, we use the power $n = 10$.

For traffic penalty, we use a quadratic function

$$r_2\big(v_{\text{traf}}(s), v\big) = \rho_2\big(v_{\text{traf}}(s) - v\big)^2, \tag{4.16}$$

which is illustrated in Figure 4.3(b) for the weight $\rho_2 = 1[\mathrm{gs/m^2}]$. Indeed, the traffic penalty increases when the vehicle speed moves away from the traffic flow speed $v_{\text{traf}}(s)$ that is given as a function of the arc-length s. We remark that we use an Eulerian description to describe the traffic flow, that is, v_{traf} shows the "averaged" flow speed at location s and

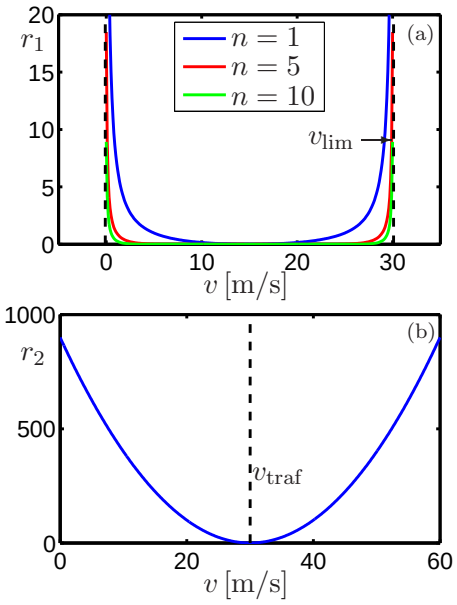

Figure 4.3: Traffic penalty given by (4.14,4.15,4.16).

does not necessarily correspond to the speed of an individual vehicle (that would require a Lagrangian description [78]). When increasing the weight ρ_1, one intends to adapt more to the traffic flow speed.

4.2 Optimal Control Problem and Necessary Conditions for Optimality

Substituting (4.11) into (4.1), we obtain

$$J_0 = \int_0^{t_\mathrm{f}} (p_2 v u + p_1 v + p_0)\,\mathrm{d}t + \sigma_0\, t_\mathrm{f} + \int_0^{t_\mathrm{f}} r(s,v)\,\mathrm{d}t. \tag{4.17}$$

Since $\int_0^{t_\mathrm{f}} p_1 v(t)\,\mathrm{d}t = p_1 s_\mathrm{f}$ is constant, this term may be dropped. We define $\sigma = p_0 + \sigma_0$, drop the subscript of p_2, and redefine the objective function as

$$J = \int_0^{t_\mathrm{f}} p\, u v\,\mathrm{d}t + \sigma\, t_\mathrm{f} + \int_0^{t_\mathrm{f}} r(s,v)\,\mathrm{d}t. \tag{4.18}$$

To minimize this, we need to determine a piecewise continuous control function $u : [0, t_f] \to \mathbb{R}$ that minimizes the functional (4.18) subject to the dynamic system (4.2) (or specifically (4.9)), the boundary conditions (4.3) and the mixed state-control constraints (4.4) (or specifically (4.13)). For systems with mixed constraints, necessary conditions of

optimality were derived in [70, 72, 79] in the form of PMP, and the following analytical framework is based on these works.

Let $x = [s, v]^{\mathrm{T}}$ be the state vector of the system and $\lambda = [\lambda_s, \lambda_v]^{\mathrm{T}}$ be the associated costate vectors. The standard Hamiltonian function is defined as

$$\begin{aligned} H(x, \lambda, u) &= puv + \sigma + r(v, s) \\ &\quad + \lambda_s v + \lambda_v(-\alpha h'(s) - \beta - \kappa v^2 + u). \end{aligned} \tag{4.19}$$

Then, the *augmented* Hamiltonian that takes into account the mixed constraints is given by

$$\mathcal{H}(x, \lambda, \mu, u) = H(x, \lambda, u) + \mu^{\mathrm{T}} C(x, u), \tag{4.20}$$

where $C = [C_1, C_2]^{\mathrm{T}}$ are given by (4.13) and $\mu = [\mu_1, \mu_2]^{\mathrm{T}}$ are the Lagrange multipliers.

Let x^*, u^* denote a local minimum pair of the optimal control problem. Then according to [70] there exist a continuous and piecewise continuously differentiable costate $\lambda^* : [0, t_{\mathrm{f}}] \to \mathbb{R}^2$ and a continuous multiplier $\mu^* : [0, t_{\mathrm{f}}] \to \mathbb{R}^2$ such that the following conditions hold:

1. adjoint equations
$$\dot{\lambda}^* = -\partial_x \mathcal{H}(x^*, \lambda^*, \mu^*, u^*). \tag{4.21}$$

2. minimum condition for the standard Hamiltonian
$$H(x^*(t), \lambda^*(t), u^*(t)) = \min_{u \in \Omega(t)} H(x^*(t), \lambda^*(t), u), \tag{4.22}$$
with (momentarily) admissible control set
$$\Omega(t) = \big\{ u \,|\, 0 \le u \le \min\{a_{\max},\, U/v^*(t)\} \big\}.$$

3. local minimum condition for the augmented Hamiltonian
$$\partial_u \mathcal{H}(x^*(t), \lambda^*(t), \mu^*(t), u^*(t)) \equiv 0. \tag{4.23}$$

4. complementarity condition
$$\mu^*(t) \ge 0, \qquad \mu^*(t)^{\mathrm{T}} C(x^*(t), u^*(t)) = 0, \tag{4.24}$$

5. transversality condition (for free terminal time t_f)

$$H(x^*(t_\mathrm{f}), \lambda^*(t_\mathrm{f}), u^*(t_\mathrm{f})) = 0. \tag{4.25}$$

Note that because C_1 and C_2 cannot be active at the same time, the complementarity condition (4.24) actually leads to $\mu_i^* C_i = 0$, $i = 1, 2$ when either of the constraints is active and, consequently, the constraint qualification condition is trivially satisfied [68]. Also note that we do not get a terminal condition for $\lambda(t_\mathrm{f})$, since the terminal state $x(t_\mathrm{f})$ is fixed.

From now on we abuse the notation and drop the $*$ for the optimal solution. Using (4.19) and (4.20), the adjoint equation (4.21) becomes

$$\begin{bmatrix} \dot{\lambda}_s \\ \dot{\lambda}_v \end{bmatrix} = \begin{bmatrix} \lambda_v \alpha h''(s) - \partial_s r(v, s) \\ -\lambda_s + 2\lambda_v \kappa v - pu - \partial_v r(v, s) - \mu_1 \partial_v C_1 - \mu_2 \partial_v C_2 \end{bmatrix}, \tag{4.26}$$

where ∂_s and ∂_v denote the partial derivatives with respect to s and v, respectively. Since the control variable u appears linearly in the Hamiltonian (4.19), the minimum condition (4.22) gives the controller

$$u(t) = \begin{cases} \min\{a_{\max}, U/v(t)\}, & \text{if} \quad \zeta(t) < 0, \\ u^{\mathrm{sing}}(t), & \text{if} \quad \zeta(t) = 0,\ t \in I_\mathrm{s} \subset [0, t_f] \\ 0, & \text{if} \quad \zeta(t) > 0, \end{cases} \tag{4.27}$$

where I_s denotes the time interval corresponds to singular arc, $\zeta(t) = \zeta(v(t), \lambda_v(t))$ is the *switching function* given by

$$\zeta(v, \lambda_v) = \partial_u H = pv + \lambda_v, \tag{4.28}$$

and the control input u^{sing} along the singular arc is described further below. To determine the multipliers μ_1 and μ_2, we use the local minimum condition (4.23) which gives

$$\mu_1 = -\frac{\zeta}{\partial_u C_1}, \quad \mu_2 = -\frac{\zeta}{\partial_u C_2}. \tag{4.29}$$

Note that the sign condition $\mu_1 \geq 0$ and $\mu_2 \geq 0$ in (4.24) are in accordance with the sign of the switching function ζ in (4.28), and we exploited that C_1 and C_2 cannot be active at the same time.

Now we derive a formula of the singular control u^{sing} in (4.27). We achieve this by differentiating (4.28) with respect to time until u appears explicitly. The derivation is carried out for the case with no traffic penalty ($r(s, v) \equiv 0$ in (4.14)), but it can easily be gener-

alized when adding traffic penalty. Assume that control takes values in the interior of the control set, that is, $C_i(v,u) < 0$ for $i = 1, 2$, in a certain time interval $I_{\rm s}$. Then the singular arc is given by

$$\zeta = pv + \lambda_v = 0, \tag{4.30}$$

cf. (4.27,4.28). Differentiating this with respect to time and using (4.2,4.9,4.26) we obtain

$$\dot{\zeta} = p\big(-\alpha h'(s) - \beta - \kappa v^2\big) - \lambda_s + \lambda_v\, 2\kappa v = 0. \tag{4.31}$$

Note that the control variable u drops out in accordance with the theory of singular control; see [80]. Substituting $\lambda_v = -pv$ we attain

$$\dot{\zeta} = p(-\alpha h'(s) - \beta - 3\kappa v^2) - \lambda_s = 0. \tag{4.32}$$

Using again (4.2,4.9,4.26), the second derivative of ζ is computed as

$$\begin{aligned} \ddot{\zeta} \;&=\; p\big(-\alpha h''(s)v - 6\kappa v(-\alpha h'(s) - \beta - \kappa v^2 + u)\big) \\ &\quad -\lambda_v \alpha h''(s) = 0. \end{aligned} \tag{4.33}$$

Substituting $\lambda_v = -pv$ again, we obtain

$$\begin{aligned} \ddot{\zeta} \;&= -p6\kappa v\big(-\alpha h'(s) - \beta - \kappa v^2 + u\big) \\ &= -p6\kappa v \cdot \dot{v} = 0. \end{aligned} \tag{4.34}$$

The control u appears explicitly in the second derivative of ζ and, hence, a singular arc is of *first order*; see [80]. According to (4.34) a singular arc is characterized by the condition $\dot{v} \equiv 0$ of constant speed which yields the singular control

$$u^{\rm sing}(s,v) = \alpha h'(s) + \beta + \kappa v^2. \tag{4.35}$$

Moreover, note that the strict generalized Legendre-Clesch condition (GLC), which is a higher order necessary condition for the singular control to be optimal, holds since

$$-\frac{\partial \ddot{\zeta}}{\partial u} = 6p\kappa v \;> 0, \tag{4.36}$$

see [80]. To interpret the physical meaning of singular control (4.35), we give the following two theorems.

Theorem 2. *Assume that $\kappa \neq 0$ in (4.9), no constraints are applied to control input u, and no traffic penalties are considered ($r(s,v) \equiv 0$ in (4.14)). Then the necessary and*

sufficient condition to maintain $\zeta = 0$ is having constant speed $v \equiv \sqrt[3]{\sigma/(2p\kappa)}$, which can be calculated by setting $\dot{v} \equiv 0$ and using (4.25).

Theorem 3. *If the gradient $h'(s)$ is such that $0 \leq \alpha\, h'(s) + \beta + \kappa\, v^2 < \min\{a_{\max}, U/v\}$ for $s \in [0, s_{\mathrm{f}}]$ and we assume $v(0) = v(t_{\mathrm{f}}) = v_0$, then the singular control input (4.35) maintains a speed constant along the whole route.*

According to these theorems, if the combined effect of the grade, rolling resistance and wind are small, then limiting the acceleration (by traveling with constant speed) is the best strategy to minimize the fuel consumption. On the other hand, it will be demonstrated below that when the external effects are significant, the optimal controller switches between the minimum and maximum of u.

In the rest of this chapter, we will use the vector notation

$$X = [s, v, \lambda_s, \lambda_v]^{\mathrm{T}}. \tag{4.37}$$

Then the boundary value problem (4.2,4.3,4.9,4.25,4.26) can be summarized as

$$\begin{bmatrix} \dot{s} \\ \dot{v} \\ \dot{\lambda}_s \\ \dot{\lambda}_v \end{bmatrix} = \begin{bmatrix} v \\ -\alpha\, h'(s) - \beta - \kappa\, v^2 + u \\ \lambda_v \alpha\, h''(s) - \partial_s r(v, s) \\ -\lambda_s + 2\,\lambda_v \kappa\, v - p\, u - \partial_v r(v, s) - \mu_1 \partial_v C_1 - \mu_2 \partial_v C_2 \end{bmatrix}, \tag{4.38}$$

$$\underbrace{\begin{bmatrix} s(0) \\ s(t_{\mathrm{f}}) - s_{\mathrm{f}} \\ pv(0) - v_0 \\ v(t_{\mathrm{f}}) - v_{\mathrm{f}} \\ H(s(t_{\mathrm{f}}), v(t_{\mathrm{f}}), \lambda_s(t_{\mathrm{f}}), \lambda_v(t_{\mathrm{f}}), u(t_{\mathrm{f}})) \end{bmatrix}}_{\mathbf{B}(X(0), X(t_{\mathrm{f}}))} = \begin{bmatrix} 0 \\ 0 \\ 0 \\ 0 \\ 0 \end{bmatrix}. \tag{4.39}$$

There is no general existence and uniqueness conditions for boundary value problems, even for smooth dynamic systems [81]. Therefore, whether a solution exists is unknown when setting the parameter values. Even if system (4.27,4.38,4.39) consists of smooth subsystems, switches make the system non-smooth. Moreover, varying the parameter σ changes the boundary condition (4.39), and consequently, changes the optimal solution. We also remark that (4.27,4.38,4.39) essentially give a multi-point boundary value problem (MBVP) since the switching times $t_k \in (0, t_{\mathrm{f}})$, where the switching function $\zeta(t)$ vanishes, are not known a priori. Standard numerical methods like the shooting method cannot be applied directly to solve this problem as the system may become very sensitive to initial

conditions due to the switches at the interim points. In this chapter, we bypass this issue by using smoothing techniques and apply collocation to obtain the solutions. These combined with pseudo-arclength continuation allow us to trace the optimal solution while varying parameters. To obtain an initial guess of the solution, we analyze the switching structure of the optimal controller for a simplified linearized model.

Alternatively, one can discretize the problem by using a large number of grid points and solve the resulting nonlinear programming problem (NLP), e.g., by the Interior-Point optimization code IPOPT [82] that is implemented using the Applied Modeling Programming Language (AMPL) [83]. We use this direct "discretize and then optimize" approach to check the solutions provided by the proposed "collocation and continuation" method explained above. However, we remark that the direct method requires much finer time mesh to obtain the optimal solution.

4.3 Analytical Solution of the Linear Damped System

In this section, we simplify the BVP (4.27,4.38,4.39) to a linear system with simple constraints, and derive the analytical solution. This allows us to characterize how the optimal solution changes with the parameter σ. Moreover, the analytical solution will be utilized in Section 4.4 to initialize the numerical continuation when solving the original nonlinear BVP. Here, the air drag is substituted by linear damping, i.e., κv^2 is replaced by $\kappa v_0 v$, where $v_0 = v(0)$. Furthermore, traffic penalty is omitted by setting $r(s, v) \equiv 0$ in (4.14). Finally, the constraints (4.13) are substituted by $0 \leq u \leq a_{\max}$. Thus, (4.38) is simplified to the affine equations

$$\begin{bmatrix} \dot{s} \\ \dot{v} \\ \dot{\lambda}_s \\ \dot{\lambda}_v \end{bmatrix} = \begin{bmatrix} 0 & 1 & 0 & 0 \\ -2\alpha\frac{h_{\mathrm{R}}}{s_{\mathrm{R}}^2} & -\kappa v_0 & 0 & 0 \\ 0 & 0 & 0 & 2\alpha\frac{h_{\mathrm{R}}}{s_{\mathrm{R}}^2} \\ 0 & 0 & -1 & \kappa v_0 \end{bmatrix} \begin{bmatrix} s \\ v \\ \lambda_s \\ \lambda_v \end{bmatrix} + \begin{bmatrix} 0 \\ 2\alpha\frac{h_{\mathrm{R}}}{s_{\mathrm{R}}} - \beta + u \\ 0 \\ -pu \end{bmatrix}, \tag{4.40}$$

which can be solved analytically, given the control input u. According to (4.27), the input u stays at its maximum $a_{\max}$ or minimum 0 when $\zeta \neq 0$. Therefore, we obtain the solution

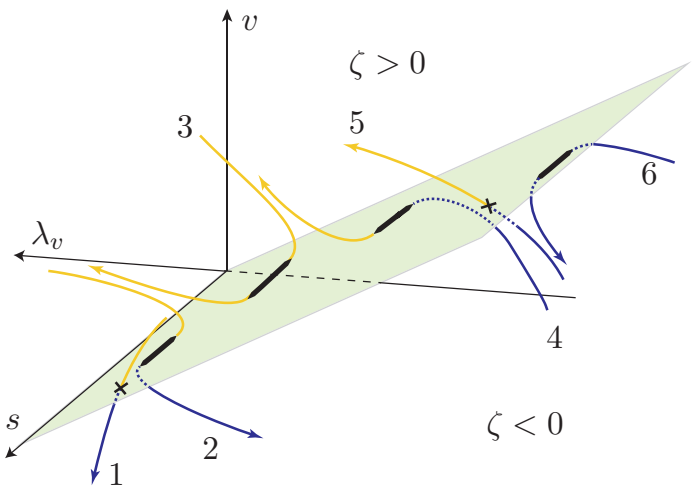

Figure 4.4: Six possible scenarios involving one switch. For trajectories 1 and 2, u switches from maximum to minimum (i.e., $\zeta = pv + \lambda_v$ switches from negative to positive). For trajectories 4 and 5, u switches from minimum to maximum (i.e., $\zeta = pv+\lambda_v$ switches from positive to negative). Trajectories 1 and 5 represent transverse scenarios, while trajectories 2 and 4 show tangential scenarios. Trajectories 3 and 6 are for the grazing scenarios, where the minimum and the maximum control input is maintained, respectively. Bold segments and crosses indicate $\zeta = 0$.

in the following form when u is constant.

$$\underbrace{\begin{bmatrix} s(t) \\ v(t) \\ \lambda_s(t) \\ \lambda_v(t) \end{bmatrix}}_{X(t)} = \underbrace{\begin{bmatrix} F_1(s_0, v_0, t, u) \\ F_2(s_0, v_0, t, u) \\ F_3(\lambda_{s0}, \lambda_{v0}, t, u) \\ F_4(\lambda_{s0}, \lambda_{v0}, t, u) \end{bmatrix}}_{\mathbf{F}(X_0,t,u)}, \tag{4.41}$$

where we used the abbreviated notation: $s(0) = s_0$, $v(0) = v_0$, $\lambda_s(0) = \lambda_{s0}$, $\lambda_v(0) = \lambda_{v0}$, $X_0 = X(t_0) = [s_0, v_0, \lambda_{s0}, \lambda_{v0}]^{\mathrm{T}}$. Note that, when u changes in time, we may still get an expression similar to (4.41), but the right hand side becomes a functional. In this case the dynamics of s, v and the dynamics of λ_s, λ_v are not decoupled anymore, but the control law (4.27) makes them coupled through switching. Even though we cannot guarantee that a unique solution exists, we assume that the boundary condition (4.39) allows at least one solution.

If the system does not satisfy the conditions in Theorem 3, the control input switches between the cases in (4.27). Switches may occur in 6 different ways as illustrated in Figure 4.4 where the switching surface $\zeta = 0$ is also depicted. The control input u either switches from the maximum $a_{\max}$ to minimum 0 (trajectories 1 and 2), or vice versa (trajectories 4

and 5). Trajectories 3 and 6 do not cross the switching surface but attach to it and leave to the same side, so the control input stays at the minimum (trajectory 3) or at the maximum (trajectory 6). We call them *grazing scenarios*. Trajectories 1 and 5 are named *traverse scenarios* since these trajectories go through the switching surface. On the other hand, trajectories 2 and 4 attach to the plane, travel along it, and leave it on the other side. We name these *tangential scenarios*. We remark that the switching structure is determined by the boundary conditions and in general multiple switches may occur.

By solving the affine equation (4.40) analytically, the linear system (4.27,4.39,4.40) can be transformed to a system of nonlinear algebraic equations. By using the notation defined in (4.39,4.41), for the traverse scenario we obtain

$$\begin{aligned} &\mathbf{B}(X_0, X_{\mathrm{f}}) = \mathbf{0}, \\ &X_1 = \mathbf{F}(X_0, t_1, a_{\mathrm{d1}}), \\ &X_{\mathrm{f}} = \mathbf{F}(X_1, t_{\mathrm{f}} - t_1, a_{\mathrm{df}}), \end{aligned} \tag{4.42}$$

where $X_1 = X(t_1)$, $X_{\mathrm{f}} = X(t_{\mathrm{f}})$, $a_{\mathrm{d1}}, a_{\mathrm{df}} \in \{0, a_{\max}\}$ such that $a_{\mathrm{d1}} \neq a_{\mathrm{df}}$. Solving these equations we obtain $t_1, t_{\mathrm{f}}, \lambda_{s0}, \lambda_{v0}$. On the other hand, for the tangential and grazing scenarios, we have

$$\begin{aligned} &\mathbf{B}(X_0, X_{\mathrm{f}}) = \mathbf{0}, \\ &p\dot{v} + \dot{\lambda}_v = 0, \quad \text{for} \quad t \in [t_1, t_2], \\ &X_1 = \mathbf{F}(X_0, t_1, a_{\mathrm{d1}}), \\ &X_{\mathrm{f}} = \mathbf{F}(X_2, t_{\mathrm{f}} - t_2, a_{\mathrm{df}}), \end{aligned} \tag{4.43}$$

where $a_{\mathrm{d1}}, a_{\mathrm{df}} \in \{0, a_{\max}\}$ such that $a_{\mathrm{d1}} \neq a_{\mathrm{df}}$ for tangential scenarios and $a_{\mathrm{d1}} = a_{\mathrm{df}}$ for grazing scenarios. Solving these equations we obtain $t_1, t_2, t_{\mathrm{f}}, \lambda_{s0}, \lambda_{v0}$. The overall solution of the multi-point boundary value problem will be a series of segments that are given analytically.

As an example, we consider the case $v(t_{\mathrm{f}}) = v(0) = 25\,[\mathrm{m/s}]$, $a_{\max} = 0.6\,[\mathrm{m/s^2}]$. We set $a_{\max}$ at this value since it is close to the minimum value of U/v in the velocity range we consider; see Figure 4.2. With these parameters, all types of switches shown in Figure 4.4 can be obtained except trajectory 6. Meanwhile, solutions with multiple switches also appear.

The range of parameter σ is divided into 6 domains and the appearing 6 different types of solutions are shown in Figure 4.5. Red dashed curves represent analytical solutions while blue solid curves represent numerical simulations for the same initial condition, and

they match very well. We compared these trajectories with those using a direct method "discrete and optimize" method mentioned in Section 3 and they essentially give the same results.

When $\sigma \in [0, 1.05]$ [g/s], the optimal solution is of transverse scenario 1, and the control input switches from minimum to maximum, see case A in Figure 4.5. When $\sigma \in [1.05, 3.71]$ [g/s], the optimal solution is of attached scenario 2, and the control input changes from minimum to maximum but the trajectory attaches to the surface $\zeta = 0$ in the middle; see case B in Figure 4.5. When $\sigma \in [3.71, 4.33]$ [g/s], the optimal solution is of grazing scenario 3, and the control input starts from minimum and ends at minimum while attaching to the plane $\zeta = 0$ in the middle; see case C in Figure 4.5. When $\sigma \in [4.33, 9.43]$ [g/s], trajectories with two switches exist so that the transverse scenario 5 followed by the attached scenario 3; see case D in Figure 4.5. When $\sigma \in [9.43, 12.73]$ [g/s], the optimal solution is of attached scenario 4; see case E in Figure 4.5. Finally, when $\sigma \in [12.73, +\infty)$ [g/s], the optimal solution is of transverse scenario 5; see case F in Figure 4.5.

The terminal time t_f and total fuel consumption Q are plotted in Figure 4.6 as a function of σ, where the total fuel consumption is defined as

$$Q = \int_0^{t_\mathrm{f}} q(v, u)\,\mathrm{d}t = \int_0^{t_\mathrm{f}} (p_2 v u + p_1 v + p_0)\,\mathrm{d}t, \tag{4.44}$$

cf. (4.1,4.11). The six domains explained above are separated by the black vertical lines, with the numbers 1-5 indicating the solution type corresponding to those in Figure 4.4, while the letters A–F correspond to the cases in Figure 4.5. Note that the solution $\sigma > 12.73$ [g/s] the trajectories for s, v and u are essentially the same as those for $\sigma = 15$ [g/s].

The analysis of this simplified problem shows that by varying the system parameters, the optimal solution may change qualitatively. To experience the trade-off between travel time and fuel consumption, one shall set $\sigma \in [3, 15]$, where, indeed, better fuel economy leads to a longer traveling time. Meanwhile, it is possible to use the analytical solution to start the numerical continuation and gradually steer the system to the original nonlinear system. We will introduce the numerical technique in Section 4.4.

4.4 Numerical Solution of the Full Nonlinear System

In this section we investigate the original nonlinear BVP (4.27,4.38,4.39) using numerical continuation. This technique was originally developed to compute solutions of systems of parameterized nonlinear equations [84]. The idea is to start from a solution with certain set of system parameters and gradually change the parameters until the target parameters are

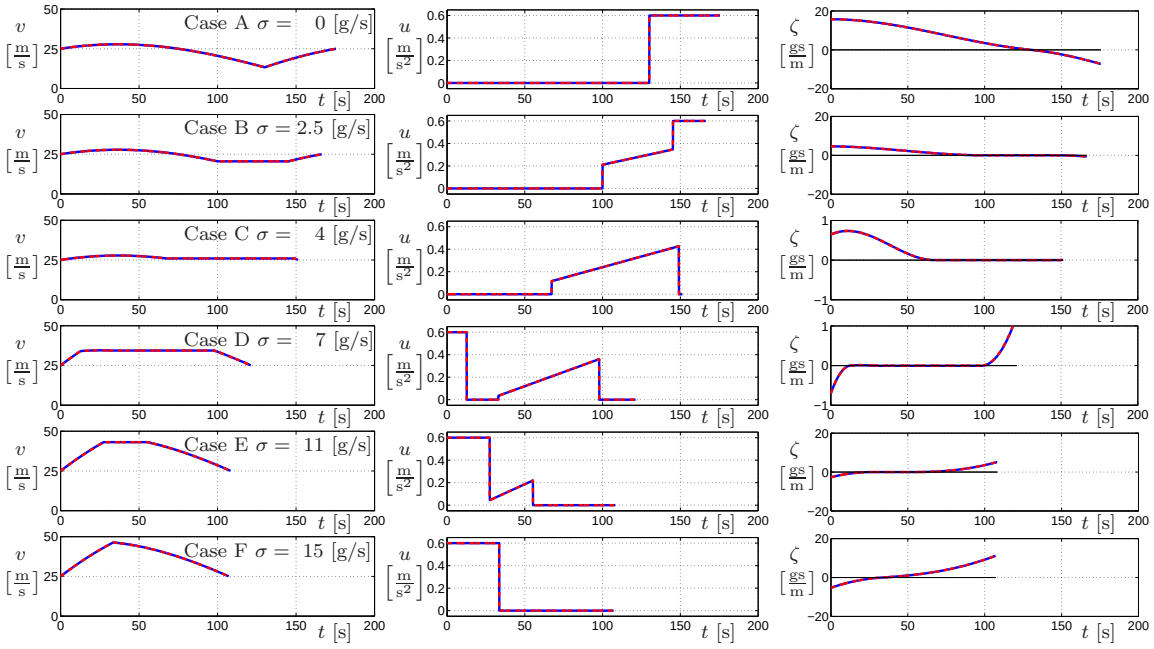

Figure 4.5: Time evolution of the speed v (left column), the corresponding control input u (middle column), and the switching variable ζ (right column) for different values of the parameters σ as indicated. The rows correspond to the points A–F marked in Figure 4.6. Red dashed curves represent analytical solutions while blue solid curves represent numerical solutions and they match very well.

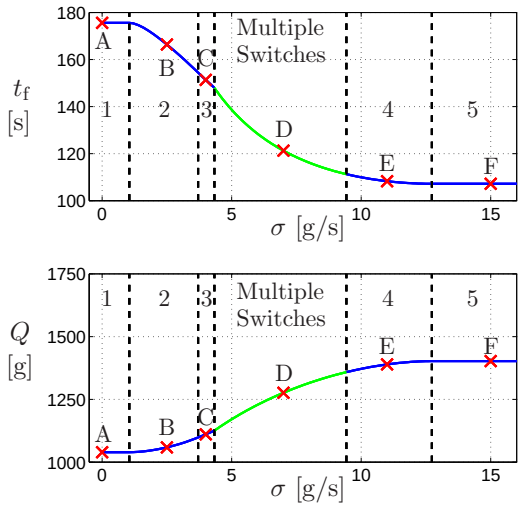

Figure 4.6: The upper panel gives the terminal time t_f as a function of σ, while the lower panel shows the total fuel consumption Q (4.44) as a function of σ, for $v(t_f) = v(0) = 25\,[\mathrm{m/s}]$, $a_{\max} = 0.6\,[\mathrm{m/s^2}]$ for the system (4.27,4.40). The black dashed vertical lines separate 6 regions of qualitatively different solutions, with the numbers corresponding to those in Figure 4.4. The points A–F corresponds to the cases in Figure 4.5

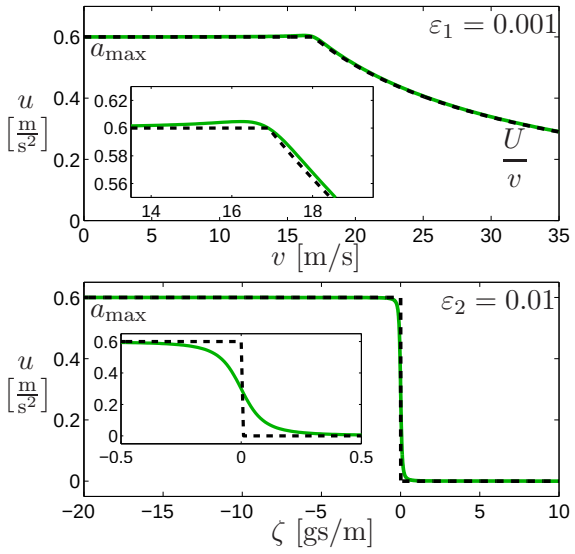

Figure 4.7: Visualization of the nonsmooth functions (4.12,4.27) (black dashed) and the corresponding smooth functions (4.45,4.46) (solid green).

reached; see Appendix A for a brief overview of the method. We start from the solution of the simplified system (4.27,4.39,4.40) and add nonlinearities gradually until we reach (4.27,4.38,4.39) by varying the parameters. Besides the nonlinear "bang-bang" controller (4.27), the original problem also has other types of nonlinearity: nonlinear input constraint $a_{\mathrm{U}}(v)$ in (4.13), air drag in (4.9), and traffic penalty $r(v, s)$ in (4.1).

Instead of starting from $U \to \infty$, we set $U = 100\,[\mathrm{m}^2/\mathrm{s}^3]$, so that $U/v \gg a_{\max} = 0.6[\mathrm{m}/\mathrm{s}^2]$; see Figure 4.2. Then we decrease U until we reach U=$P_{\max}/m_{\text{eff}}$=$10.14[\mathrm{m}^2/\mathrm{s}^3]$. After that we change the maximum acceleration gradually from $a_{\max} = 0.6[\mathrm{m}/\mathrm{s}^2]$ to $a_{\max} = 2[\mathrm{m}/\mathrm{s}^2]$. This last step does not change the optimal trajectories in the cases considered here. The nonlinear air drag term is added by varying $\tilde{\kappa}$ from 0 to κ in $\tilde{\kappa}v^2+(\kappa-\tilde{\kappa})v_0 v$. The traffic penalty (4.14) is introduced in similar manners. For speed limit r_1, initially we set v_{lim} in (4.15) to be large and gradually decrease it to the target value while ρ_1 is kept fixed. For penalty r_2 corresponding to the deviation from the traffic speed, we introduce it gradually by increasing ρ_2.

Since continuation requires a certain level of smoothness, we derive an approximate system by smoothing (4.27,4.38,4.39). Specifically, the smoothed version of constraint (4.12) is written as

$$\tilde{a}_{\mathrm{U}}(v) = \frac{a_{\max} + U/v}{2} - \frac{(a_{\max} - U/v)^2}{2\sqrt{\varepsilon_1 + (a_{\max} - U/v)^2}}, \tag{4.45}$$

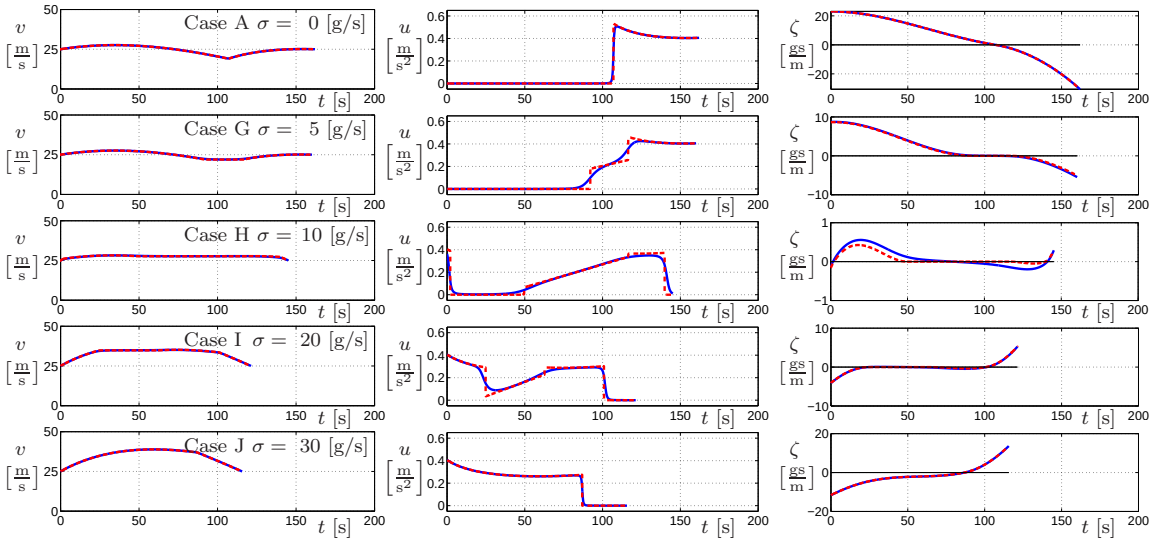

Figure 4.8: Time evolution of the speed v (left column), the corresponding control input u (center column), and the switching variable ζ for different values of the parameter σ (right column) as indicated. The rows correspond to the points A, G, H, I, J marked in Figure 4.10. The blue solid curves are associated with the trajectories acquired by the our BVP solver based on pseudo arc-length collocation method using the smoothed controller (4.45,4.46), the red dashed curves are those generated by direct method.

while the smoothed version of the switching rule (4.27) is given as

$$u = \frac{1}{2} a_{\mathrm{U}}(v)\left(1 - \frac{\zeta}{\sqrt{\varepsilon_2 + \zeta^2}}\right), \tag{4.46}$$

where ε_1 and ε_2 are small parameters with units $[\mathrm{m}^2/\mathrm{s}^4]$ and $[\mathrm{g}^2\mathrm{s}^2/\mathrm{m}^2]$, respectively. In Figure 4.7 the nonsmooth functions (4.12,4.27) (black dashed curves) are compared to (4.45,4.46) (solid green curves), for $\varepsilon_1 = 0.001[\mathrm{m}^2/\mathrm{s}^4]$, $\varepsilon_2 = 0.01[\mathrm{g}^2\mathrm{s}^2/\mathrm{m}^2]$ and $a_{\max} = 0.6[\mathrm{m}/\mathrm{s}^2]$. Indeed, the smoothed curves approximate the nonsmooth ones well.

Our BVP solver is based on pseudo arclength continuation algorithm. We discretize the BVP using collocation method [85] which results in a large system of nonlinear equations that also depends on parameters. Then a continuation algorithm is used to solve these nonlinear equations while varying parameters. To speed up the computation, we use adaptive steps. When solving BVPs with singular arcs with other methods like the shooting method, [68,81,86], difficulties often arise due to the sensitivity with respect to initial values. The collocation method can bypass this problem because it tunes the whole solution, that is, distributes the sensitivity along the whole trajectory. In this chapter, we use the collocation method with 400 points $\varepsilon_1 = 10^{-6}[\mathrm{m}^2/\mathrm{s}^4]$ and $\varepsilon_2 = 0.01[\mathrm{g}^2\mathrm{s}^2/\mathrm{m}^2]$.

The time evolution of the system (4.27,4.38,4.39) is shown in Figure 4.8 for different

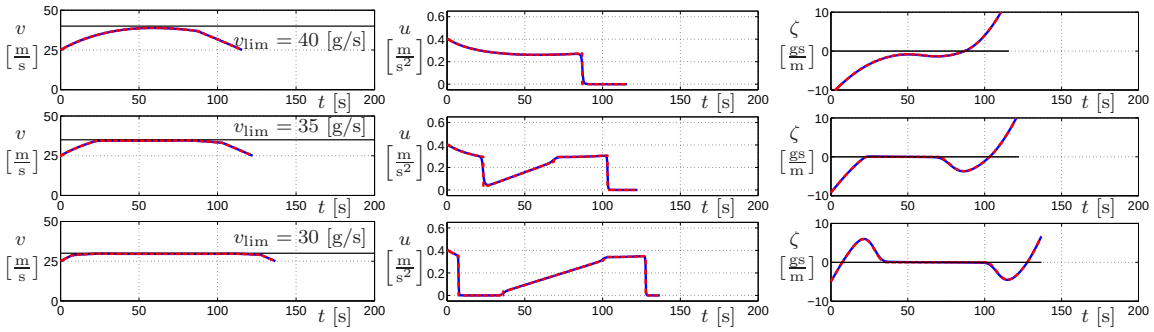

Figure 4.9: Effect of the speed limit penalty with different values of $v_{\lim}$ as indicated. The same notation is used as that in Figure 4.8.

values of σ as indicated (different from those used in Figure 4.5, and 4.6 for better illustration of the switching structure). The blue solid curves are the trajectories acquired by the our BVP solver based on pseudo arc-length continuation method using the smoothed controller (4.45,4.46), while the red dashed curves are generated by a direct method using the nonsmooth controller (4.27). The two trajectories in each panel are close to each other, implying that the smoothed controller represents the original non-smooth one with a good accuracy. Note that when applying our method we used 400 points to represent the trajectory, and for the direct method we used 10000 points, which increases the computational demand significantly. The numerical solutions of the nonlinear system maintain the same trend as the analytical solutions of the linear system. That is, as σ increases, the solutions starts with minimum to maximum bang-bang type controller. Then, a singular arc appears. Eventually it becomes a bang-bang type again but with maximum to minimum switch. We also plot the terminal time t_{f} and the total fuel consumption Q (cf. (4.44)) as functions of σ in Figure 4.10. Compared with Figure 4.6, besides the change in values of terminal time and total fuel consumption, the transition region expands in the σ direction due to the nonlinearities.

We summarize the above results in Table 4.1, where we show the terminal time t_{f} and the total fuel consumption Q for different σ values for $v(0) = v(t_{\mathrm{f}}) = 25$ [m/s]. For comparison, we also show the results for constant speed (that can be maintained using standard cruise control). When σ is small the optimal solution consumes approximately 11.9% less fuel compared to the constant speed scenario. On the other hand, when the weight on terminal time is large and the truck reaches its destination earlier but consumes more fuel. Again we can identify the region $\sigma \in [3, 30]$ where one has a trade-off between travel time and fuel consumption. We remark that in order to maintain the constant speed, braking and large engine torque may be needed (i.e., the constraints (4.13) may be violated). Therefore the constant speed driving profile is not necessarily in the function space for the

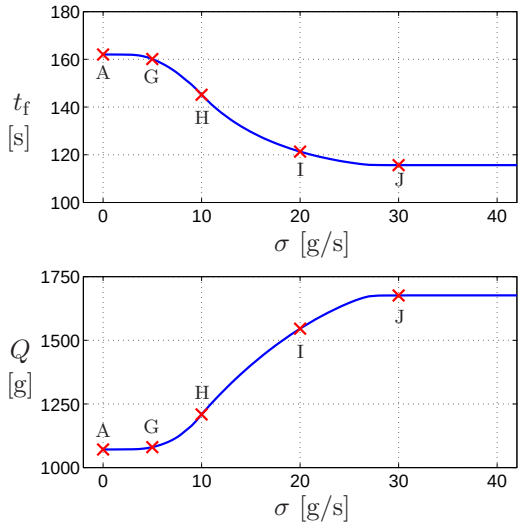

Figure 4.10: The terminal time t_f (upper panel) and the fuel consumption Q (4.44) (lower panel) as a function of σ for $v(t_f) = v(0) = 25\,[\mathrm{m/s}]$. The corresponding trajectories are shown in Figure 4.8 for the points marked A, G, H, I, J.

	t_f[s]	Q[g]
$\sigma = 0$ (Case A)	162.1	1071.1
$\sigma = 5$ (Case G)	160.1	1080.2
$\sigma = 10$ (Case H)	145.2	1208.9
$\sigma = 20$ (Case I)	121.3	1545.7
$\sigma = 30$ (Case J)	115.6	1676.2
Cruise Control	160.0	1222.3

Table 4.1: Terminal time t_f and fuel consumption Q for multiple σ values (cf. Figure 4.8), compared with the fuel consumption and time of cruise control, with conditions $v(0) = v(t_f) = 25[\mathrm{m/s}]$.

optimal control problem. Finally, we remark that increasing the speed of headwind will increase the length of the time where maximum available control input is applied.

4.5 Traffic Information

In this section, we investigate the effect of the penalty term on traffic. In particular, we study the effects of the speed limit and the traffic flow speed separately. We first study the penalty on speed limit by setting $\rho_1 = 0.1[\mathrm{g/s}]$, and $\rho_2 = 0[\mathrm{gs/m^2}]$ and using constant v_{lim} along the route, cf. (4.15). We start from the solution with $\sigma = 30[\mathrm{g/m}]$ (cf. Figure 4.8, case J, where the maximum speed reaches $\approx 39[\mathrm{m/s}]$) and continue the solution while changing v_{lim} from $40[\mathrm{m/s}]$ to $30[\mathrm{m/s}]$. The results are shown in Figure 4.9 where the

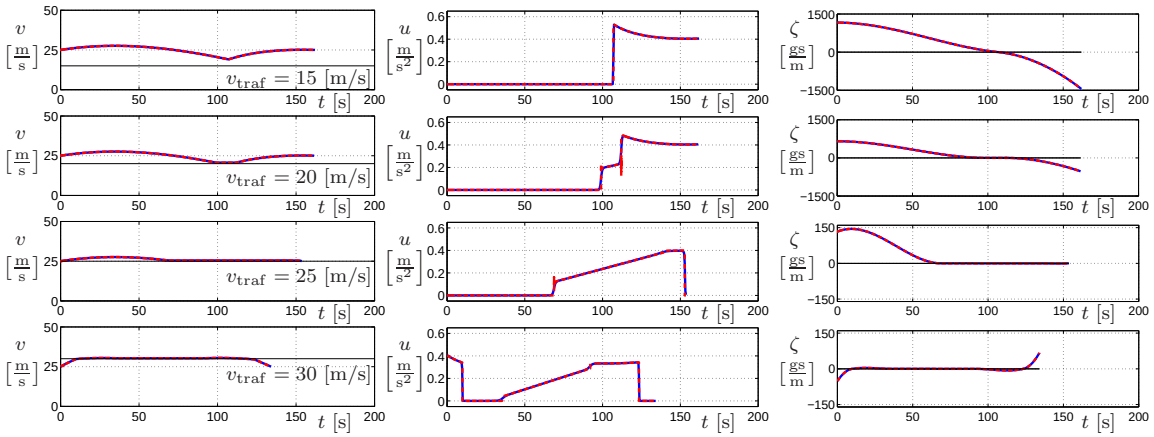

Figure 4.11: Traffic flow penalty with different values of v_{traf} as indicated. The same notation is used as that in Figure 4.8.

same notation is used as in Figure 4.8. As the speed limit decreases, the maximum speed of the optimal speed profile decreases in response. Notice that to achieve the optimal profile, complicated switching structure may be required for the control input. For example, when $v_{\text{lim}} = 30\,[\text{m/s}]$, minimum control, singular control and maximum control are all needed.

In order to investigate the effect of traffic flow penalty, we set $\sigma = 30[\text{g/s}]$, $\rho_1 = 0[\text{g/s}]$, and consider v_{traf} to be constant along the route; cf. (4.16). We start from the solution with $\sigma = 30[\text{g/m}]$ (cf. Figure 4.8 case J), and change ρ_2 from 0 to 1. The results with different v_{traf} values are shown in Figure 4.11, where again the same notation is used as in Figure 4.8. Four different values of the constant traffic speed v_{traf} are considered along the road and the results imply that the optimal trajectories settle down to different speed profiles. When v_{traf} is small, the speed profile is similar to the solution without traffic penalty; cf. Figure 4.8, case A. This is because, according to the results in Section 4.4, the solution is the one with the lowest average speed, so the controller cannot bring the vehicle to lower speed. Note that lower desired traffic speed v_{traf} can be achieved by adjusting problem parameters (e.g., the boundary condition (4.3) and the constraints (4.4)) but such analysis is beyond the scope of this chapter. As v_{traf} increases, the speed profile comes closer to v_{traf} and the penalty cost is reduced. However, as a result of the multi-objective optimization considering fuel consumption, travel time, and traffic speed, the optimal profile requires nontrivial control action including multiple switches between maximum, minimum and singular control.

Finally, in Figure 4.12 we show the ratio between traffic cost and the total cost (4.1) as a function of the weight ρ_2. When it is achievable by control, the speed profile gets closer to the traffic flow speed (as in the second two rows of Figure 4.11) and therefore $(v - v_{\text{traf}})^2$ goes to zero as ρ_2 increases. As a result, the ratio between traffic cost and the total cost

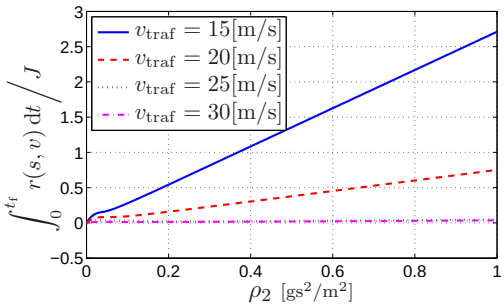

Figure 4.12: The ratio between the traffic cost and the total cost (4.1) as a function of the weight ρ_2.

will converge to a constant value, as shown by the black dotted and magenta dashed-dotted curves in Figure 4.12. On the other hand, if the traffic flow speed cannot be followed by the vehicle using any feasible control (as in the first two rows of Figure 4.11), then the speed profile remains significantly different from the traffic flow as ρ_2 increases. As a result, the ratio between traffic cost and the total cost will keep growing as ρ_2 increases, since $(v - v_{\text{traf}})^2$ converges to a constant value, as demonstrated by the blue solid and red dashed curves in Figure 4.12. These results show that increasing the weight on traffic may not force the vehicle to approach the desired speed given by the traffic conditions. Also, we emphasize that this desired speed does not correspond to the speed of a particular vehicle. To take into account such effects (e.g., to address safety) a different description is needed and it is left for future research.

4.6 Summary

In this chapter, we proposed a framework for fuel economy optimization of heavy duty vehicles that can incorporate road elevation, headwind, desired terminal time, and traffic information. We established a systematic approach in order to solve the arising multi-objective optimal control problem while varying the system parameters. First, we solved a simplified problem analytically that allowed us to characterize the switching structure of the resulting bang-bang controller or bang-singular-bang controller. Then, we used this knowledge to initialize our numerical continuation software.

We demonstrated that varying the weight on the desired terminal time causes qualitative changes in the switching structure of the controller. We also identified a parameter region where one can balance the fuel-economy and the traveling time. Moreover, we investigated the effects of traffic dynamics and identified the conditions (in term of the traffic speed and the weigh on the traffic cost) that allow the truck to balance between fuel economy

and adaptation to traffic conditions. These were achieved by nontrivial control actions that cannot be obtained intuitively.

For fuel efficient driving in heavy traffic conditions, reacting to the motion of individual vehicles in the neighborhood may be important. Merging such an Lagrangian description with the Eulerian description used in the chapter is a challenging task. One possible mean is by incorporating V2V information from multiple vehicles ahead as will be investigated in Chapter 5.

CHAPTER 5

Fuel Efficient Connected Cruise Control for Heavy-duty Trucks in Real Traffic

All stable processes we shall predict.
All unstable processes we shall control.

JOHN VON NEUMANN

In the previous chapter, the analysis on fuel efficient control was carried out, assuming the traffic perturbations were mild. In this chapter, we focus on the case when a heavy duty truck is in a dense traffic and need to react to traffic perturbations.

At the vehicle level, one may use geo-location information to do eco-driving and design optimal speed profiles [11,14,87]. Without traffic perturbations, such optimal speed profiles can lead to over 10 percent reduction in fuel consumption, as pointed out in Chapter 4. However, this benefit may not be attainable in real traffic when a truck has to respond to the speed profiles of human-driven vehicles ahead. While an automated truck using on-board sensors may respond to such scenarios better than a human driver, the fuel-economy improvement may still be limited because on-board sensors can only obtain information within their lines of sight [33].

To further improve fuel economy in real traffic, one approach is to monitor the motion of multiple vehicles ahead and utilize beyond-line-of-sight information through vehicle-to-vehicle (V2V) communication. Some researchers have designed centralized and cooperative controllers for platoons of automated trucks [88, 89], so that each participating truck can enjoy significant fuel improvement [35,90]. However, it can be challenging to organize such cooperative platoons, before automated trucks become widespread [91]. Therefore, non-cooperative schemes have been proposed to predict the preceding vehicle's motion and optimize fuel economy in a receding horizon manner [41,42,92–94]. Yet such methods often have heavy computational load [47], and their performance in real traffic is unclear when the prediction accuracy is low. While stochastic approaches and off-line methods can

be used to alleviate such limitations [22], examples from other research areas indicate that a simpler design scheme may be more applicable and even perform better in real application scenarios [37].

Therefore, we directly include V2V information from multiple vehicles ahead in the feedback structure and propose the concept of connected cruise control (CCC) [44]. A vehicle driven by such a connected cruise controller is referred to as a connected automated vehicle (CAV). While a small percentage of connected automated vehicles on the road can already improve traffic safety and efficiency [45, 46], the connected automated vehicle itself can also achieve better fuel economy theoretically [47–49]. Yet the question remains whether connected cruise control can indeed save fuel in real traffic. To answer this question, in this chapter, we present a data-driven design for connected cruise control that improves fuel economy through minimizing overall energy consumption. We evaluate the design with real traffic data, and demonstrate that the proposed connected cruise controller can lead to robust fuel savings in real traffic.

The reminder of this chapter is organized as follows. In Section 5.1, as a motivation to the proposed design, we use real traffic data to analyze the influence of traffic perturbations on a truck's fuel consumption using a high-fidelity model. We demonstrate that the majority of fuel consumption in traffic is due to the energy consumption during speed fluctuations. In Section 5.2, we present a connected cruise control design that utilizes motion information of multiple vehicles ahead to minimize such energy consumptions in traffic. The proposed design is evaluated in Section 5.3 using real traffic data sets, and the results are also compared to those obtained using receding-horizon controllers. Finally, the conclusions are given in Section 5.4.

5.1 Evaluating fuel consumption in traffic

In this section, we demonstrate the impact of traffic perturbations on a truck's fuel consumption using real traffic data. We show that while such impacts can be reduced by tuning the longitudinal controller through high-fidelity simulations, a systematic optimization method is needed for more robust designs.

In this illustrative example, we consider a driving scenario where a truck drives behind several human-driven vehicles on a segment of flat road that has one lane in each direction;

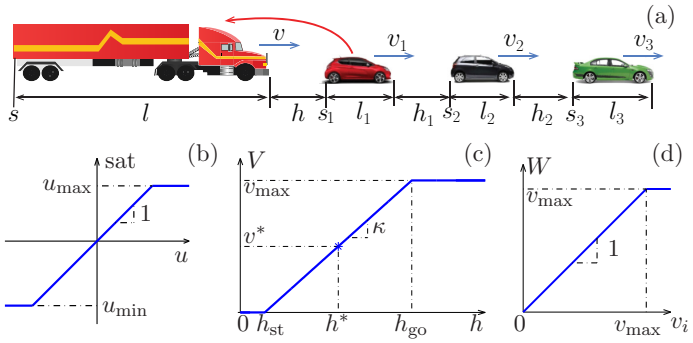

Figure 5.1: (a) A truck driving behind three human-driven vehicles on a single-lane road. (b) The saturation function in (5.1). (c) The range policy function (5.5). (d) The saturation function (5.6).

see Figure 5.1(a). The longitudinal motion of the truck can be described by

$$\begin{aligned} \dot{s}(t) &= v(t), \\ \dot{v}(t) &= -f\big(v(t)\big) + \mathrm{sat}\Big(\tilde{f}\big(v(t-\zeta)\big) + a_{\mathrm{d}}(t-\zeta)\Big), \end{aligned} \tag{5.1}$$

where the dots denote differentiation with respect to time t, s denotes the position of the rear bumper of the truck, v denotes its velocity, and ζ is the actuator delay that can also be approximated by a first order lag [42, 44].

The physical effects like air resistance and rolling resistance are described by

$$f(v) = \frac{1}{m_{\text{eff}}}(\gamma m \mathrm{g} + k_0 v^2)\,, \tag{5.2}$$

where g is the gravitational constant, γ is the rolling resistance coefficient, k_0 is the air drag constant, and the effective mass $m_{\text{eff}} = m + I/R^2$ includes the mass of the vehicle m, the moment of inertia I of the rotating elements, and the wheel radius R [87]. To compensate for these physical effects, the term $\tilde{f}$ is often added through a lower-level controller. Finally, a_{d} denotes the higher-level acceleration command, which is limited between $u_{\min}$ and $u_{\max}$ by the saturation function $\mathrm{sat}(\cdot)$ based on the engine and braking power limit; see Figure 5.1(b). In this chapter, we use $u_{\max} = 1\,[\mathrm{m/s^2}]$ and $u_{\min} = -4\,[\mathrm{m/s^2}]$ for the truck.

If the truck is driven by a human driver or adaptive cruise controller, the higher-level controller can be modeled as

$$\begin{aligned} a_{\mathrm{d}}(t) =& \alpha\Big(V\big(h(t-\xi_1)\big) - v(t-\xi_1)\Big) \\ &+ \beta_1\Big(W\big(v_1(t-\xi_1)\big) - v(t-\xi_1)\Big)\,. \end{aligned} \tag{5.3}$$

Here α and β_1 are the feedback gains. The headway

$$h = s_1 - s - l\,, \tag{5.4}$$

is the distance gap between the truck and its preceding vehicle, where l denotes the length of the truck. Finally, ξ_1 represents the sensory delay of position and speed information from vehicle 1.

The range policy function

$$V(h) = \begin{cases} 0 & \text{if } h \leq h_{\rm st}, \\ \kappa(h - h_{\rm st}) & \text{if } h_{\rm st} < h < h_{\rm go}, \\ v_{\max} & \text{if } h \geq h_{\rm go}, \end{cases} \tag{5.5}$$

describes the desired velocity of the truck as a function of its headway; see Figure 5.1(c). For a small headway ($h < h_{\rm st}$), the truck intends to stop; for a large headway ($h > h_{\rm go}$), it intends to travel with the speed limit $v_{\max}$; between $h_{\rm st}$ and $h_{\rm go}$ the desired velocity increases linearly, with the gradient $\kappa = v_{\max}/(h_{\rm go} - h_{\rm st})$. Finally, the saturation function

$$W(v_1) = \begin{cases} v_1 & \text{if} \quad v_1 \leq v_{\max}, \\ v_{\max} & \text{if} \quad v_1 > v_{\max}, \end{cases} \tag{5.6}$$

shown in Figure 5.1(d) is included to stay below the speed limit when a preceding vehicle is speeding. In this chapter, we use $v_{\max} = 30\,[\mathrm{m/s}]$, $h_{\rm st} = 5\,[\mathrm{m}]$ and $\kappa = 0.6\,[1/\mathrm{s}]$.

To evaluate the performance of a truck under higher-level controllers such as (5.3), we build a high-fidelity model in TruckSim based on a 2012 Navistar Prostar truck [1]; see Figure 5.2 for the configuration and Appendix 2.1 for the data. In Figure 5.2, acceleration commands for the truck are calculated using (5.3) and the motion information of the human-driven vehicle ahead. These higher-level commands are then converted by a lower-level controller into throttle and brake commands. Then using the TruckSim module, we obtain the truck's speed v, its engine speed $\omega_{\rm e}$ and engine torque $T_{\rm e}$. Finally, the truck's fuel consumption can be obtained using the fuel map $q(\omega_{\rm e}, T_{\rm e})$.

In order to evaluate the influence of traffic perturbations on fuel consumption, we define the cumulative energy consumption for the truck per unit mass

$$w(t) = \int_{t_0}^{t} v(\tilde{t}) g\Big(\dot{v}(\tilde{t}) + f\big(v(\tilde{t})\big)\Big)\,\mathrm{d}\tilde{t}\,, \tag{5.7}$$

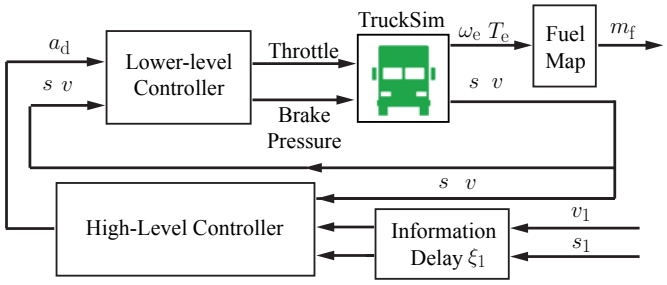

Figure 5.2: Structure of the high-fidelity simulation platform using TruckSim and MATLAB/Simulink to obtain the speed response and energy/fuel consumption of a truck responding to traffic perturbations.

where $t \in [t_0, t_{\rm f}]$ and $g(x) = \max(0, x)$. For vehicles with internal combustion engines, fuel consumption typically increases with the energy consumption $w(t)$. However, as $w(t)$ is defined by the vehicle's motion, it can also be used to evaluate the energy consumption of electric or hybrid vehicles due to speed variations using an appropriate g function.

In order to describe the traffic perturbations, we track the motion of three consecutive human-driven vehicles in traffic. Two sets of recorded speed data are plotted in Figure 5.3(a,b), where the green, black, and red curves correspond to the speed of vehicle 3, vehicle 2 and vehicle 1, respectively. In both cases, while the human-driven vehicles travel with average speed of $\overline{v} \approx 22$ [m/s], their speed data exhibit large variations that are often observed in dense traffic. We perform fast Fourier transforms on the speed data and display their spectral amplitude ρ_i and phase angle ϕ_i in Figure 5.3(c-f). The spectral plots in panels (c,d) show that both speed profiles contain similar Fourier components that are mainly low-frequency oscillations.

Using the high-fidelity simulation platform shown in Figure 5.2, we simulate the truck responding to speed perturbations shown in Figure 5.3(a,b) and obtain its energy consumption (5.7) as well as the fuel consumption for different values of the feedback parameters in the controller (5.3). In Figure 5.3(g,h), we plot the total energy consumption (blue dots) of the truck during each simulation for $\kappa = 0.6$ [1/s] and $\alpha = 0.4$ [1/s], while $\beta_1 \in \{0.1, \ldots, 1.0\}$ [1/s]. In panel (g), the truck consumes the least amount of energy when $\beta_1 = 0.6$ [1/s]. Moreover, as we calculate the total fuel consumption (red dots), we find the truck also consumes the least amount of fuel at $\beta_1 = 0.6$ [1/s]. This indicates that one may minimize the fuel consumption through minimizing the energy consumption while tuning the feedback gains in the higher-level controller (5.3).

If there were no speed perturbations, i.e., the preceding vehicles have constant speed, the truck could also maintain the same constant speed. Then it consumes the total energy

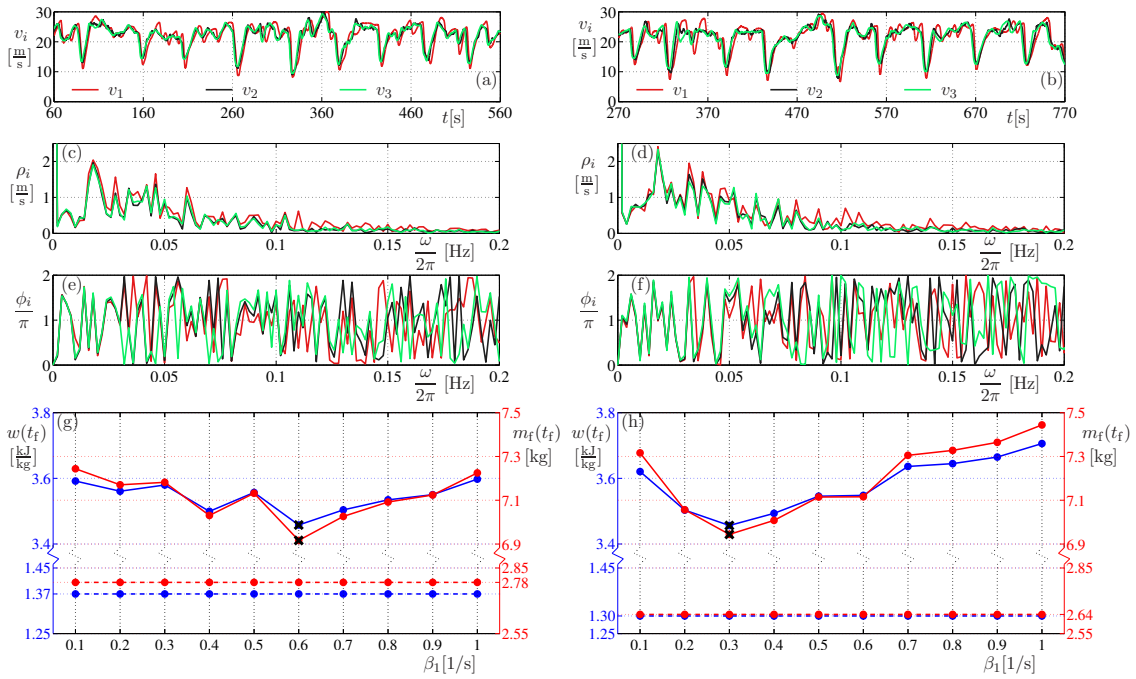

Figure 5.3: (a,b) Speed profiles of preceding human-driven vehicles, where the red, black, and green curves represent v_1, v_2, v_3 , respectively. (c,d) The amplitude spectra and (e,f) the phase angle spectra of the speed profiles. (g,h) The total energy consumption (5.7) at the end of each run for different values of the control gain β_1 is shown as blue dots. The total mass of fuel m_f consumed by the truck in the high-fidelity simulation for the same parameters is shown as red dots. For both curves, the black cross denotes the minimum point. For comparison the values corresponding to constant speed are also plotted as blue and red dots connected by dashed lines.

$w(t_\mathrm{f}) = 1.37$ [kJ/kg] and the total fuel $m_\mathrm{f}(t_\mathrm{f}) = 2.78$ [kg]; see the blue and red dots along the dashed lines in Figure 5.3(g). While constant-speed driving comprises less than half of the total fuel/energy consumption, such motion can rarely be achieved in real traffic. Nevertheless, the truck may reduce its energy consumption towards the constant-speed level, if it is able to minimize its speed variation despite the traffic perturbations. In particular, such smooth speed profiles can be maintained using connected cruise control, where V2V signals from vehicles ahead serve as a "preview" of incoming traffic situations.

While the high-fidelity simulation platform can readily provide optimal controller gains given specific speed profiles, it can be very costly in computation, and the optimal design may be very sensitive even with similar speed profiles. For example, based on Figure 5.3(g), one may be tempted to set $\beta_1 = 0.6$ [1/s] for the truck driving in such slow-and-go traffic. However, in panel (h), under speed profiles that are qualitatively very similar, the energy and fuel minima are reached at $\beta_1 = 0.3$ [1/s]. Therefore, in the next section, we exploit the Fourier spectrum of the traffic perturbations in the connected cruise control design, in order to obtain optimal parameters that are robust and computationally efficient.

5.2 Data-driven Connected Cruise Control

In this section, we consider a connected cruise controller for the truck that includes direct feedback on speed signals from n human-driven vehicles ahead (see red arrows in Figure 5.4). In particular, we propose the connected cruise controller for the connected automated truck

$$\begin{aligned} a_\mathrm{d}(t) =& \alpha\Big(V\big(h(t-\xi_1)\big) - v(t-\xi_1)\Big) \\ &+ \sum_{i=1}^{n} \beta_i\Big(W\big(v_i(t-\xi_i)\big) - v(t-\xi_i)\Big)\,. \end{aligned} \tag{5.8}$$

cf. (5.3) and recall that h is the headway defined in (5.4).

The speed signals from vehicles farther ahead can be viewed as "preview information" about speed variations propagating towards the connected automated truck. By including v_i, $i = 2, \ldots, n$, in the feedback structure, the connected cruise controller (5.8) gains "phase lead" against variations in the speed v_1 of its immediate predecessor. In this way, (5.8) enjoys the advantages of many cooperative adaptive cruise control designs [91] without requiring the support of an automated vehicle fleet. While headway, speed, and acceleration from multiple preceding vehicles can be used in connected cruise control [95, 96], here we only use V2V speed signals for simplicity.

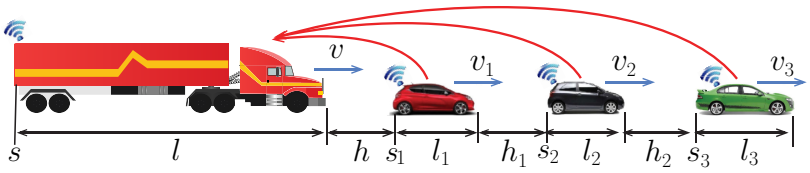

Figure 5.4: Layout of the connected vehicle system with a truck at the tail controlled by a CCC algorithm. Each preceding vehicle is reacting to motion of the vehicle immediately ahead while the truck utilizes V2V information from all three vehicles ahead.

5.2.1 Stability condition for maintaining constant speed

Before searching for the energy/fuel-optimal feedback gains, it is necessary to obtain the stability boundaries to ensure that the connected automated truck is able to maintain constant speed. Thus, we consider the steady-state traffic flow where

$$v(t) \equiv v_i(t) \equiv v^*, \tag{5.9}$$

for $i = 1, \ldots, n$ and

$$h(t) \equiv h^*, \quad v^* = V(h^*)\,, \tag{5.10}$$

cf. (5.5) and Figure 5.1(c).

We define $\tilde{s}$, $\tilde{s}_1$, $\tilde{v}_i$, $i = 1, \ldots, n$ as the perturbations about the equilibrium positions and velocities and assume that the influence of the physical effects $f(v)$ can be negated by $\tilde{f}(v)$. Then linearizing the dynamics (5.1,5.8) of the connected automated truck about (5.9), we obtain

$$\begin{aligned}
\dot{\tilde{s}}(t) =& \tilde{v}, \\
\dot{\tilde{v}}(t) =& \alpha\Big(\kappa\big(\tilde{h}(t-\sigma_1)\big) - \tilde{v}(t-\sigma_1)\Big) \\
&+ \sum_{i=1}^{n} \beta_i\Big(\tilde{v}_i(t-\sigma_i) - \tilde{v}(t-\sigma_i)\Big)\,,
\end{aligned} \tag{5.11}$$

where $\tilde{h} = \tilde{s}_1 - \tilde{s}$ is the perturbation about the equilibrium headway h^* and $\sigma_i = \xi_i + \zeta$ for $i = 1, \ldots, n$ gives the total delay in the control loop. For simplicity, we consider $\sigma_i = \sigma$ for $i = 1, \ldots, n$.

In order for the connected automated truck (5.1,5.8) to be able to maintain its speed around the equilibrium, we require the linearized dynamics (5.11) to be plant stable [44].

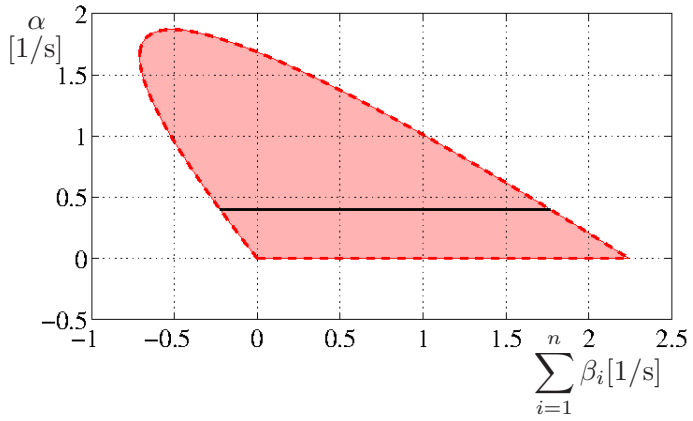

Figure 5.5: Stability diagram for $\kappa = 0.6$ [1/s] and $\sigma = 0.7$ [s] where the shaded region corresponds to plant stable parameters, with the black line segment corresponds to $\alpha = 0.4$ [1/s].

That is, all roots of the characteristic equation

$$D(\lambda) = \lambda^2 \mathrm{e}^{\sigma\lambda} + \left(\alpha + \sum_{i=1}^{n} \beta_i\right)\lambda + \alpha\kappa = 0 \tag{5.12}$$

must be located in the left half complex plane. Thus, the design parameters α and β_i need to be selected from the domain enclosed by

$$\alpha = 0, \tag{5.13}$$

and

$$\begin{aligned} \alpha &= \frac{\Omega^2}{\kappa}\cos(\Omega\sigma), \\ \sum_{i=1}^{n} \beta_i &= \Omega \sin(\Omega\sigma) - \frac{\Omega^2}{\kappa}\cos(\Omega\sigma), \end{aligned} \tag{5.14}$$

for $\Omega > 0$.

In Figure 5.5, we plot the plant-stable domain in the $(\sum_{i=1}^{n} \beta_i, \alpha)$-plane for $\kappa = 0.6$ [1/s] and $\sigma = 0.7$ [s]. For the headway feedback gain $\alpha = 0.4$ [1/s], the plant-stable range of $\sum_{i=1}^{n} \beta_i$ is highlighted by the black line in Figure 5.5.

5.2.2 Data-driven minimization on energy consumption

Given the similarity between energy-optimal and fuel-optimal designs (see Section 5.1), here we propose an energy-optimal connected cruise control design by exploiting the Fouri-

er decomposition of traffic perturbations.

Based on the linearized dynamics (5.11), the speed oscillation of the connected automated truck can be written as

$$\tilde{V}(\lambda) = \sum_{i=1}^{n} \Gamma_i(\lambda; \mathbf{p}_n)\tilde{V}_i(\lambda)\,, \tag{5.15}$$

where $\tilde{V}_i(\lambda)$ is the Laplace transform of the velocity perturbation $\tilde{v}_i(t)$, the vector $\mathbf{p}_n = [\alpha, \kappa, \beta_1, \ldots, \beta_n]$ contains the design parameters, and the so-called link transfer function from the i-th vehicle to the connected automated truck can be formulated as

$$\begin{aligned} \Gamma_1(\lambda; \mathbf{p}_n) &= \frac{\alpha\kappa + \lambda\beta_1}{\lambda^2 \mathrm{e}^{\sigma\lambda} + \left(\alpha + \sum_{k=1}^{n} \beta_k\right)\lambda + \alpha\kappa}, \\ \Gamma_i(\lambda; \mathbf{p}_n) &= \frac{\lambda\beta_i}{\lambda^2 \mathrm{e}^{\sigma\lambda} + \left(\alpha + \sum_{k=1}^{n} \beta_k\right)\lambda + \alpha\kappa}\,, \end{aligned} \tag{5.16}$$

for $i = 2, \ldots, n$.

Assume that the speed data $v_1, \ldots, v_n$ are available through V2V communication, then the velocity perturbation of vehicle i can be described using the m leading frequency components

$$\tilde{v}_i(t) \approx \sum_{j=1}^{m} \rho_{i,j} \sin(\omega_j t + \phi_{i,j})\,, \tag{5.17}$$

where we discretize frequency $\omega_j = j\Delta\omega$, with $\Delta\omega = 2\pi/(t_\mathrm{f} - t_0)$. Moreover, $\rho_{i,j} = \rho_i(\omega_j)$ and $\phi_{i,j} = \phi_i(\omega_j)$ are the amplitude and phase angle of speed oscillations at frequency ω_j for car i; see Figure 5.3(d-f).

Based on (5.15,5.16,5.17), the steady-state oscillation of the connected automated truck is given by

$$\tilde{v}(t) = \sum_{j=1}^{m} \sum_{i=1}^{n} \tilde{\rho}_{i,j}(\mathbf{p}_n) \sin\left(\omega_j t + \tilde{\phi}_{i,j}(\mathbf{p}_n)\right), \tag{5.18}$$

where

$$\begin{aligned} \tilde{\rho}_{i,j}(\mathbf{p}_n) &= \rho_{i,j}\Gamma_i(\mathrm{i}\omega_j; \mathbf{p}_n), \\ \tilde{\phi}_{i,j}(\mathbf{p}_n) &= \phi_{i,j} + \angle\,\Gamma_i(\mathrm{i}\omega_j; \mathbf{p}_n). \end{aligned} \tag{5.19}$$

This can be rewritten as

$$\tilde{v}(t) = \sum_{j=1}^{m} D_j(\mathbf{p}_n) \sin\big(\omega_j t + \theta_j(\mathbf{p}_n)\big), \tag{5.20}$$

where

$$D_j = \sqrt{\left(\sum_{i=1}^{n} \tilde{\rho}_{i,j} \cos\tilde{\phi}_{i,j}\right)^2 + \left(\sum_{i=1}^{n} \tilde{\rho}_{i,j} \sin\tilde{\phi}_{i,j}\right)^2},$$

$$\tan\theta_j = \frac{\sum_{i=1}^{n} \tilde{\rho}_{i,j} \sin\tilde{\phi}_{i,j}}{\sum_{i=1}^{n} \tilde{\rho}_{i,j} \cos\tilde{\phi}_{i,j}}. \tag{5.21}$$

Since directly minimizing the energy consumption (5.7) may lead to designs that are overly sensitive (see Figure 5.3), here we use (5.20) and propose the minimization of the cost function

$$\min_{\mathbf{p}_n \in \mathbf{P}} J_n(\mathbf{p}_n) = \sum_{j=1}^{m} \omega_j^2 D_j^2(\mathbf{p}_n)\,, \tag{5.22}$$

where $\mathbf{P}$ is the admissible set of $\mathbf{p}_n$ that ensures plant stability; see (5.13,5.14) and Figure 5.5. Other specifications such as string stability may also be incorporated [48]. The details about the construction of (5.22) are provided in Appendix B. By computing the level sets of (5.22), the parameters in $\mathbf{p}_n$ can be related to the energy efficiency of the connected automated truck at the linear level. We remark that the computational demand of such minimization is low.

5.3 Evaluating fuel consumption of CCC in traffic

In this section, we obtain the optimal α and β_i values using (5.22) while utilizing real traffic data; see Figure 5.3. We evaluate the corresponding fuel consumption for the connected automated truck using the high-fidelity simulation platform sketched in Figure 5.2. We first establish the benchmark design where the truck only uses motion information from its immediate predecessor. We then present the energy-optimal connected cruise control designs and demonstrate its robustness when using similar speed perturbations. Finally, we compare the performance of the optimal CCC to that of a receding horizon controller.

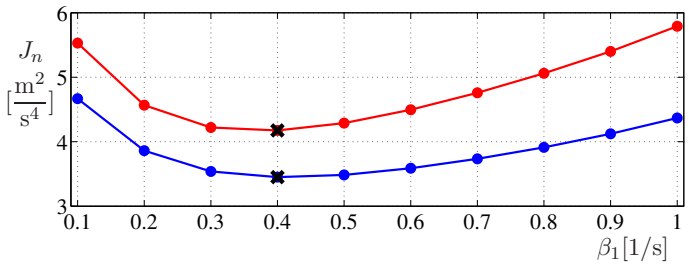

Figure 5.6: The value of objective function (5.22) for different values of the control gain β_1 for $\alpha = 0.4\,[1/\mathrm{s}]$ and $\kappa = 0.6\,[1/\mathrm{s}]$. The blue and red curves correspond to the design results using the speed profiles shown in Figure 5.3(a) and (b), respectively. For both curves, black cross denotes the minimum points.

5.3.1 Using motion information from one vehicle ahead

To establish a benchmark for the controller that exploits information from multiple vehicles ahead, we first consider the case where the truck only uses motion information from vehicle 1, that is, (5.8) reduces to (5.3) and β_1 is the only design parameter. We use the amplitude spectrum $\rho_1(\omega)$ in the objective function (5.22) for the speed profiles shown in Figure 5.3. We plot the value of (5.22) as a function of β_1 for $\alpha = 0.4\,[1/\mathrm{s}]$ and $\kappa = 0.6\,[1/\mathrm{s}]$ in Figure 5.6, where the minima are marked by the black crosses at $\beta_1 = 0.4$ [1/s]. Thus, when only motion information of the immediate predecessor is available, the parameter set $[\beta_1, \beta_2, \beta_3] = [0.4, 0, 0]$ [1/s] is the optimal design. We refer to it as the "benchmark design" in the remainder of this chapter.

In contrast to the variation of optimal β_1 in Figure 5.1(g,h), the optimal β_1 in Figure 5.6 is centered around 0.4 [1/s]. Such robustness is achieved by exploiting the Fourier spectrum of speed variations in (5.22).

5.3.2 Using motion information from multiple vehicles ahead

We now utilize motion information from vehicles 1, 2, 3 in the connected cruise controller (5.8). We consider the admissible range of β_i based on the linear stability region in Figure 5.5. Considering $\beta_1, \beta_2, \beta_3 \in \{0.1, \ldots, 1.0\}\,[1/\mathrm{s}]$, we compute the energy efficiency (5.22), and simulate the corresponding fuel consumption $m_{\mathrm{f}}(t_{\mathrm{f}})$ using the high-fidelity platform.

In Figure 5.7(a), we show the level sets of the cost function (5.22) in the (β_2, β_3)-plane for $\beta_1 = 0.1\,[1/\mathrm{s}]$ when the truck responds to the speed perturbations shown in Figure 5.3(a). The red dashed curve corresponds to the plant stability boundary; see Figure 5.5. The global minimum $J_n^* = 1.17\,[\mathrm{m}^2/\mathrm{s}^4]$ is achieved at $\mathbf{p}_n^* = [\beta_1^*, \beta_2^*, \beta_3^*] = [0.1, 0.2, 0.5]\,[1/\mathrm{s}]$, as marked by the black cross in Figure 5.7(a). Throughout this chap-

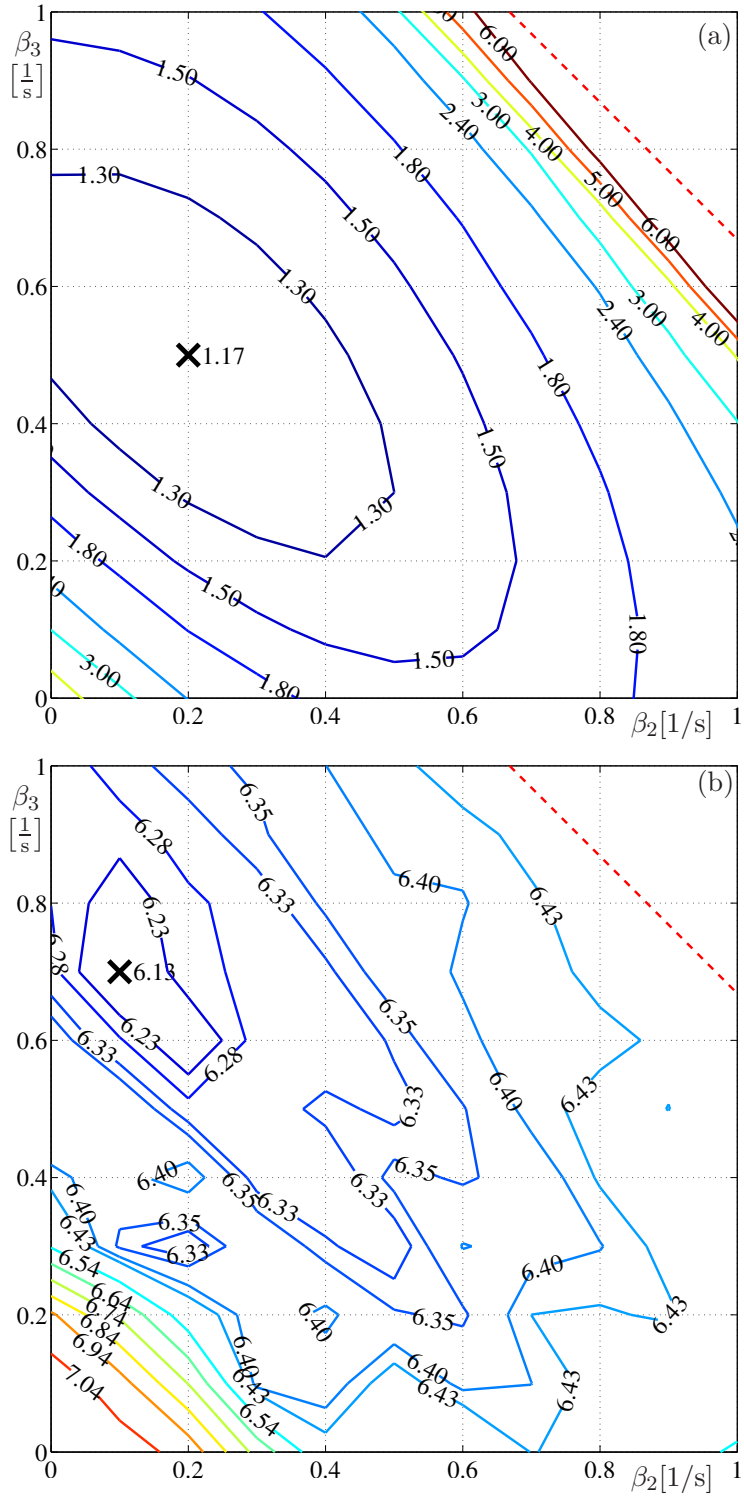

Figure 5.7: (a) The level sets of the cost function (5.22) in the (β_2, β_3)-plane for $\beta_1 = 0.1\,[1/s]$. (b) The level sets of the total fuel consumption $m_f(t_f)$ in the (β_2, β_3)-plane for $\beta_1 = 0.1\,[1/s]$. The black crosses denote the minima. The red dashed line corresponds to the stability boundary (cf. Figure 5.5).

ter, we refer this as the "energy-optimal CCC design". Note that not only the minimum is significantly smaller than the minima in Figure 5.6, but most contours in Figure 5.7(a) indicate less energy consumption than in Figure 5.6. This shows the energy-saving potentials of including the speed data from vehicles farther ahead.

In Figure 5.7(b) we show the corresponding level sets of the total fuel consumption $m_{\mathrm{f}}(t_{\mathrm{f}})$ for $\beta_1 = 0.1$ [1/s] obtained via high-fidelity Trucksim simulations. The fuel-optimal parameter combination is at is $[\beta_1, \beta_2, \beta_3] = [0.1, 0.1, 0.7]$ [1/s], as marked by the black cross. Throughout this chapter, we refer to this as the "fuel-optimal CCC design". This is close to the energy-optimal parameters (black cross in Figure 5.7(a)). Again, most level sets in Figure 5.7(b) show less fuel consumption than the minimum of the red curve in Figure 5.3(g). This indicates that even with nonlinearities in the longitudinal controller, powertrain dynamics and fuel map, adding feedback terms from vehicles farther ahead can help to improve fuel economy.

To further demonstrate the benefits of utilizing motion information from vehicles farther ahead, we plot the time profiles corresponding to the benchmark parameters $[\beta_1, \beta_2, \beta_3] = [0.4, 0, 0]$ [1/s] in blue, the energy-optimal CCC parameters $[\beta_1, \beta_2, \beta_3] = [0.1, 0.2, 0.5]$ [1/s] in green, and the fuel-optimal CCC parameters $[\beta_1, \beta_2, \beta_3] = [0.1, 0.1, 0.7]$ [1/s] in red in Figure 5.8. We also plot the speed and fuel consumption profiles that correspond to constant speed as solid black lines. Note that the two CCC designs have much smaller headway, speed, and acceleration variations, which contributes to smaller fuel consumption at the end of the simulation. While the energy-optimal and fuel-optimal parameters generate different trajectories, the difference is quite small.

When looking at the total fuel consumption $m_{\mathrm{f}}(t_{\mathrm{f}})$ at the end of the simulations in Figure 5.8(d), the energy-optimal CCC design (green) consumes about 10.4% less fuel compared with the benchmark design, while the fuel-optimal CCC design consumes about 12.8% less fuel compared with the benchmark design. Figure 5.8(c) highlights the reason behind this significant improvement: in each cycle of speed perturbation, the energy/fuel-optimal designs accelerate/brake earlier and milder than the benchmark design. With less energy dissipated in braking, the connected automated truck requests less energy from the engine and consumes less fuel.

Aside from the energy/fuel benefits of the CCC designs, we also quantify the car-following performance using the average headway error

$$\Delta h_{\mathrm{avg}} = \frac{1}{t_{\mathrm{f}} - t_0} \int_{t_0}^{t_{\mathrm{f}}} \left| h(t) - h_{\mathrm{st}} - \frac{v(t)}{\kappa} \right| \mathrm{d}t, \tag{5.23}$$

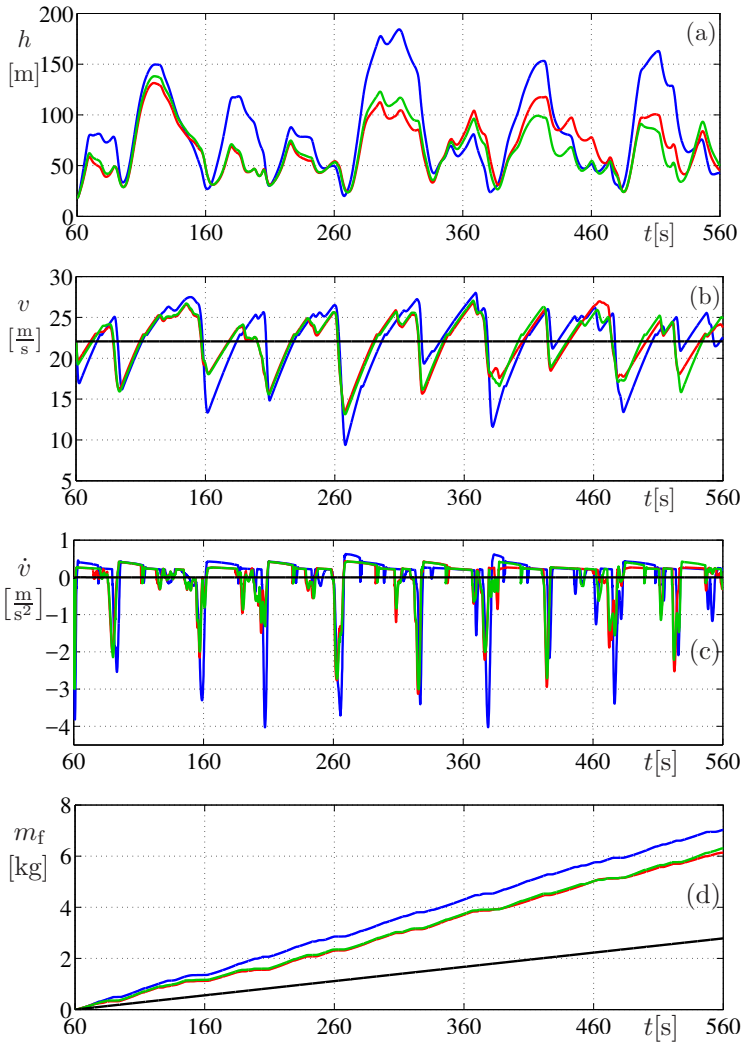

Figure 5.8: Time profiles for the connected automated truck. The blue curves correspond to the benchmark design when motion information only from vehicle 1 is used ($[\beta_1, \beta_2, \beta_3] = [0.4, 0.0, 0.0]$ [1/s]). The green curves correspond to the energy optimal CCC design when motion information from vehicles 1, 2, 3 are utilized ($[\beta_1, \beta_2, \beta_3] = [0.1, 0.2, 0.5]$ [1/s]). The red curves correspond to the fuel-optimal CCC design when motion information from vehicles 1, 2, 3 are utilized ($[\beta_1, \beta_2, \beta_3] = [0.1, 0.1, 0.7]$ [1/s]). The solid black lines corresponds to the constant speed profile without traffic disturbance.

and quantify the safety performance using the minimal time-to-collision

$$\mathrm{TTC} = \min_{t} \left\{ \frac{h(t)}{v(t) - v_1(t)} \middle| \, \forall\, v(t) > v_1(t) \right\} . \tag{5.24}$$

The total fuel consumption $m_{\mathrm{f}}(t_{\mathrm{f}})$, the average headway error Δh_{avg}, and the minimal time-to-collision TTC are summarized in Table 5.1. Based on this data we can conclude that by introducing motion information from vehicles farther ahead, fuel economy, car-following performance and safety are improved for the connected automated truck. Moreover, the energy optimal design acquired using (5.22) can achieve near optimal fuel performance without carrying out extensive simulations.

design	benchmark	energy-optimal CCC	fuel-optimal CCC
$[\beta_1, \beta_2, \beta_3]$[1/s]	[0.4, 0, 0]	[0.1, 0.2, 0.5]	[0.1, 0.1, 0.7]
$m_{\mathrm{f}}(t_{\mathrm{f}})$ [kg]	7.03	6.30	6.13
Δh_{avg}[m]	44.1	25.7	17.9
TTC [s]	4.0	5.9	6.1

Table 5.1: Fuel consumption, car-following, and safety performance for the benchmark, energy-optimal CCC, and fuel-optimal CCC designs.

5.3.3 Robustness of CCC design

For a connected automated truck responding to the speed profiles shown in Figure 5.3(a), we have obtained a benchmark design when information from its immediate predecessor is used, and energy-optimal and fuel-optimal designs when information from three vehicles ahead is used. However, the exact speed profiles used in these designs may not recur in real traffic. Thus, it is critical that given similar speed profiles, the energy/fuel-optimal gains maintain their benefits over the benchmark design. Therefore, here we evaluate the robustness of the energy-optimal design using six sets of traffic data that are qualitatively similar.

In Figure 5.9 we show the improvements of cost function (5.22), the fuel consumption, the average headway error, and the minimal time-to-collision of the energy-optimal CCC design ($[\beta_1, \beta_2, \beta_3] = [0.1, 0.2, 0.5]$ [1/s]) compared to the benchmark design ($[\beta_1, \beta_2, \beta_3] = [0.4, 0, 0]$ [1/s]) for the six data sets. It can be seen that the energy-optimal gains continue to produce 6-12% improvement in energy efficiency/fuel economy, while improvement in car-following performance and safety can also be obtained. These results demonstrate that proposed design approach can benefit the fuel economy, car-following performance,

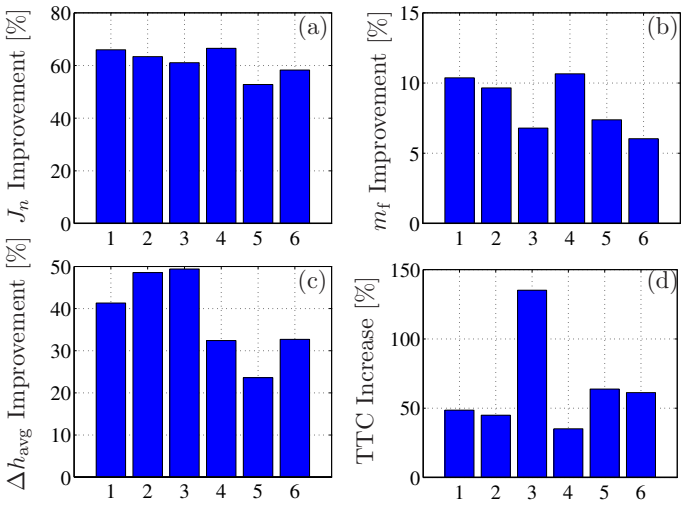

Figure 5.9: Performance improvements of the energy-optimal CCC design ($[\beta_1, \beta_2, \beta_3] = [0.1, 0.2, 0.5]$) over the benchmark design ($[\beta_1, \beta_2, \beta_3] = [0.4, 0, 0]$).

and safety of the connected automated truck, and such benefits are robust against traffic variations.

5.3.4 Comparison with receding horizon optimal control

While connected cruise control exploits "traffic preview" through motion data of vehicles farther ahead, receding horizon optimal control (RHOC) may also be used to exploit "traffic preview" by predicting the motion of the truck's immediate predecessor over a finite horizon and updating the optimal controller accordingly [41, 42]. While the energy-optimal CCC design requires much less computational load than a RHOC design, in order to declare the CCC design as an attractive alternative, its real-traffic performance needs to be at least comparable to that of a RHOC design. Therefore, here we compare the performance of the data-driven CCC design presented above to a RHOC design over real traffic data. The details of the RHOC design are presented in Appendix C; see also [41, 42].

We remark that the parameters for the RHOC problem are chosen such that the achieved car-following performance is comparable to that of the CCC design. The RHOC problem is discretized with $\Delta T = 0.1$ [s] and the resulting nonlinear programming problem is solved by the open-source interior point solver IPOPT [97]. Due to the non-convex and nonlinear nature of the problem, the solver cannot guarantee global optimality. It may also encounter infeasibility or fail to converge (exceed maximum number of iterations). In such cases, the benchmark controller with zero time delay is used, though this rarely happened for the RHOC tests reported in this section.

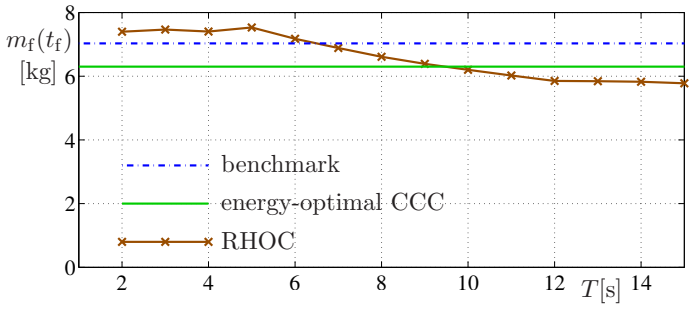

Figure 5.10: The total fuel consumption of RHOC design as a function of preview horizon T, compared to the benchmark design (blue dashed-dotted line) and the energy-optimal CCC design (solid green line).

Previous studies suggest that the length of the preview horizon has a large effect on the performance of the RHOC controllers [47]. Thus, we vary the preview horizon T from 2 [s] to 15 [s] and show the total fuel consumption of RHOC design at the end of the simulation in Figure 5.10 for the data set in Figure 5.3(a). We also mark the fuel consumption corresponding to the benchmark design (dashed-dotted blue) and the energy-optimal CCC design (solid green) in Figure 5.10. As it can be seen, RHOC requires a preview horizon to be larger than 9 [s] in order to outperform the energy-optimal CCC design. When the preview horizon is shorter than 6 [s], the RHOC performs even worse than the benchmark design. Indeed, similar trends are observed for all six data sets, underlining the robustness of these findings.

To take a closer look at the car-following performance, in Figure 5.11 we plot the time profiles of headway and speed for the RHOC design with preview horizons 5 [s] and 10 [s] (brown and magenta curves) along with the those for the benchmark design (blue curves) and energy-optimal CCC design (green curves). Notice that even for 10 [s] preview horizon the car-following performance of RHOC is worse than that of the energy-optimal CCC design.

We emphasize that the performance by RHOC design reported above are achieved by assuming perfect knowledge about the motion of the preceding vehicle. Prediction about preceding vehicle may be available for few second in practice, but most predictions are typically far from perfect; see [43, 98]. In practice, the performance may be improved by careful and extensive tuning of the parameters in the RHOC design, but it would become increasingly more specific for the specific speed profile and thus less robust. Therefore, compared with the RHOC method, the data-driven CCC design proposed in this chapter can be a desirable alternative.

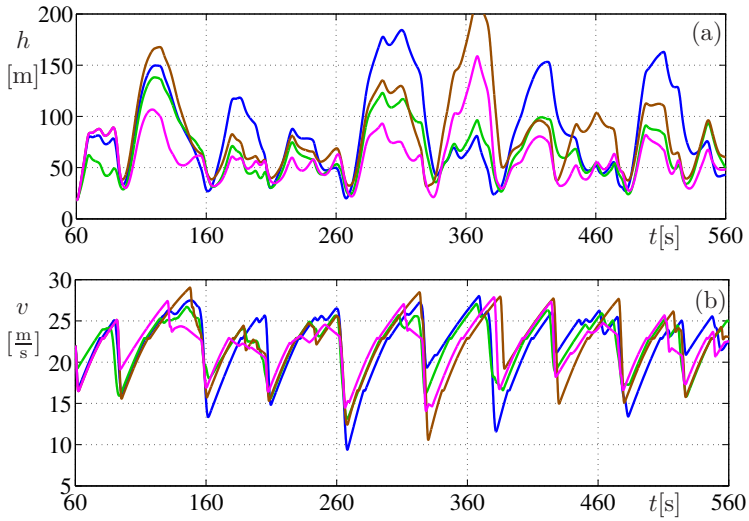

Figure 5.11: Time profiles for the connected automated truck. The blue curves corresponds to the benchmark design when motion information only from vehicle 1 is used ($[\beta_1, \beta_2, \beta_3] = [0.4, 0.0, 0.0]$ [1/s]). The green curves corresponds to the energy-optimal CCC design when motion information from vehicles 1, 2, 3 are utilized ($[\beta_1, \beta_2, \beta_3] = [0.1, 0.2, 0.5]$ [1/s]). The brown curves corresponds to the RHOC design with $T = 5$ [s], while the magenta curve corresponds to the RHOC design with $T = 10$ [s].

5.4 Summary

In this chapter, we have proposed a data-based method to optimize the energy efficiency and minimize the fuel consumption of a connected automated truck. First, using experimental data of human-driven vehicles in traffic, we demonstrated through a high-fidelity simulation platform that the fuel consumption is significantly influenced by the traffic perturbations. Then we proposed a data-based method to design optimal connected cruise controllers using the Fourier spectra of speed profiles. Evaluating the design on different sets of traffic data we found that utilizing motion information from multiple vehicles ahead not only improved the fuel economy of the connected automated truck, but also its car-following performance in traffic. Such improvements were also shown to be robust against variations in traffic data. Finally, the proposed data-driven design was shown to be a viable alternation to the receding horizon optimal control method.

At this stage, we have individual techniques at vehicle level (Chapter 4) and traffic level (this Chapter). A mechanism to allocate these techniques is needed to maximize the overall fuel saving, while ensuring that the overall system stays safe when reacting to other vehicles. In Chapter 6, an algorithm that incorporates safety concerns will be introduced to meet this need.

CHAPTER 6

Safety Guaranteed Connected Cruise Control

Scientists discover the world that exists;
engineers create the world that never was.

THEODORE VAN KARMAN

In the previous two chapters, the fuel efficient control techniques at vehicle level and traffic level were designed and analyzed. It was assumed that the resulted control action does not lead to safety hazards. To enable an implementation on real vehicles, a safety verification mechanism is required and that is the focus of this chapter. The notion of safety chart is established and utilized to provide safety guarantee while using the techniques at different levels.

Recent results in utilizing vehicle-to-vehicle (V2V) connectivity in vehicle automation has been showing significant improvements in congestion mitigation, fuel economy and vehicle safety [44, 46, 49, 99]. However, so far there exist no guarantees that can keep the V2V-based controllers collision free. In this chapter we target this important aspect and design connected cruise controllers with guaranteed safety performance. For simplicity, we focus on the simple scenario where the follower monitors the motion of its predecessor via V2V communication.

In order to integrate safety considerations into feedback control design, one may calculate sets in state space that remain invariant under certain feedback laws [100, 101]. Such approach is usually quite challenging in practice. However, recently the notion of control safety function has been introduced [102, 103] that allows one to certify the invariance of a chosen set in state space. In this chapter, we utilize these techniques for the safety enhancement of connected cruise control. In particular, we establish the notion of safety charts that allow one to select safe parameters for a given control law. Moreover, in order to handle the case with unsafe parameters, an intervention scheme is developed.

The reminder of the chapter is organized as follows. Section 6.1 establishes the connected cruise control design and define the safety requirements. Section 6.2 introduces

the method of safety verification for given feedback law. This is applied to guarantee the safety of a connected cruise controller in Section 6.3. Finally, we conclude the chapter in Section 6.4.

6.1 Connected Cruise Control Design

In this section we explain the connected cruise control design using a simple predecessor-follower setup shown in Figure 6.1(a). More complicated scenarios are discussed in [44, 96, 104]. Here we emphasize the role of actuation constraints and safety requirements.

6.1.1 Modeling and feedback law

To model the longitudinal dynamics of the vehicles, we use

$$\begin{bmatrix} \dot{h} \\ \dot{v} \\ \dot{v}_1 \end{bmatrix} = \begin{bmatrix} 0 & -1 & 1 \\ 0 & 0 & 0 \\ 0 & 0 & 0 \end{bmatrix} \begin{bmatrix} h \\ v \\ v_1 \end{bmatrix} + \begin{bmatrix} 0 \\ 0 \\ 1 \end{bmatrix} a_1 + \begin{bmatrix} 0 \\ 1 \\ 0 \end{bmatrix} a, \tag{6.1}$$

where h is the distance headway, that is, the bumper-to-bumper distance between the vehicles, v is the speed of the following vehicle, and v_1 is the speed of the preceding vehicle; see Figure 6.1(a). Moreover, a_1 denotes the acceleration of the preceding vehicles which serves as a disturbance while a denotes the acceleration of the following vehicle that will be assigned by the designed connected cruise controller.

It is assumed that a and a_1 are bounded due to the limited driving and braking torques available, that is,

$$a \in [-\underline{a}, \overline{a}], \quad a_1 \in [-\underline{a}_1, \overline{a}_1]. \tag{6.2}$$

Moreover, we also restrict speed of both vehicles to the domain

$$v, v_1 \in [0, \overline{v}]. \tag{6.3}$$

We remark that one may model the longitudinal dynamics by incorporating dissipations like rolling resistance and air drag [47]. However, for safety considerations the simple dynamics (6.1) will lead to more conservative results.

We refer to (6.1) as the open-loop system. The goal of connected cruise control design is to generate a feedback law $u(h, v, v_1, a_1)$. The design criteria typically include attenuation of velocity fluctuations (often referred as string stability [44]) as well as minimizing energy consumption [48]. According to (6.2) the feedback law enters (6.1) via $a = \mathrm{sat}(u)$ where

the saturation function is represented graphically in Figure 6.1(b). This leads to the closed-loop system

$$\begin{bmatrix} \dot{h} \\ \dot{v} \\ \dot{v}_1 \end{bmatrix} = \begin{bmatrix} v_1 - v \\ \text{sat}\big(u(h, v, v_1, a_1)\big) \\ 0 \end{bmatrix} + \begin{bmatrix} 0 \\ 0 \\ 1 \end{bmatrix} a_1. \tag{6.4}$$

The main question we try to answer here is that given a feedback law, how to make sure that a vehicle stays safe (i.e., avoids collision). This may be achieved by choosing the control parameters (e.g., feedback gains) appropriately which will lead to the concept of the safety chart. Choosing parameters from the safe regimes of the chart can ensure collision free motion. On the other hand, if the designer wishes to select parameters outside the safe parameter regime (due to other design considerations) safety may still be maintained by intervening once the given feedback law would render the vehicle unsafe.

We remark that the structure presented above is also used in adaptive cruise control design with the exception that acceleration of the proceeding vehicle a_1 is not directly available. While one may try to extract this information by taking derivatives of h and v, this requires heavy filtering, leading to significant inaccuracies and time lags. On the other hand, acceleration information can be sent via V2V communication and thus, it can be readily used in connected cruise control design [104].

Designers may come up with a plethora of feedback laws, but we require $u(h, v, v_1, a_1)$ to be continuous in its variables with piecewise continuous derivatives; see [78]. As an example we will consider the simple controller

$$u = \alpha\big(V(h) - v\big) + \beta\big(W(v_1) - v\big), \tag{6.5}$$

which is widely used in practice. The first term aims to maintain the velocity dependent distance given by the range policy

$$V(h) = \begin{cases} 0 & \text{if} \quad h < h_{\text{st}}, \\ \kappa(h - h_{\text{st}}) & \text{if} \quad h_{\text{st}} \leq h \leq h_{\text{go}}, \\ \overline{v} & \text{if} \quad h > h_{\text{go}}, \end{cases} \tag{6.6}$$

shown in Figure 6.1(c) where $h_{\text{go}} = \overline{v}/\kappa + h_{\text{st}}$. The second term in (6.5) aims to match the speed of the follower with that of the predecessor where the function

$$W(v_1) = \begin{cases} v_1 & \text{if} \quad v_1 \leq \overline{v}, \\ \overline{v} & \text{if} \quad v_1 > \overline{v}, \end{cases} \tag{6.7}$$

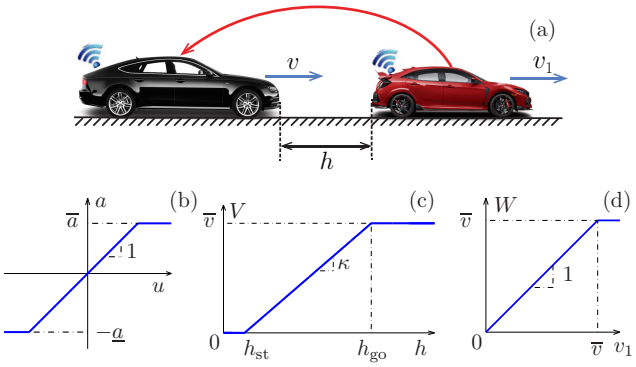

Figure 6.1: (a) Two vehicles following each other on a single lane. (b) Saturation function in (6.4). (c) Range policy function (6.6). (d) Speed saturation function (6.7).

is introduced to avoid following a speeding predecessor.

We remark that with (6.5) one can ensure that $v \in [0, \overline{v}]$. On one hand, when $v = \overline{v}$, for any given h and v_1, one has

$$\begin{aligned} &\dot{v} = u \le \alpha(\overline{v} - \overline{v}) + \beta(\overline{v} - v) = 0 \\ \Leftrightarrow \quad &\dot{v} \le 0 \quad \text{if } v = \overline{v}. \end{aligned} \tag{6.8}$$

One the other hand, when $v = 0$, for any given h and $v_1 \ge 0$, one has

$$\begin{aligned} &\dot{v} = u \ge \alpha(0 - 0) + \beta(v_1 - v) \ge 0 \\ \Leftrightarrow \quad &\dot{v} \ge 0 \quad \text{if } v = 0. \end{aligned} \tag{6.9}$$

Thus, to simplify the matter, we will focus on the controller

$$u = \alpha\big(\kappa(h - h_{\rm st}) - v\big) + \beta(v_1 - v), \tag{6.10}$$

and draw safety charts in the parameter space spanned by the desired stopping distance $h_{\rm st}$, the range policy derivative κ, and the feedback gains α and β.

6.1.2 Safety requirement

Consider the system (6.1) starts from time $t = 0$ with some initial value. A natural safety requirement would be having no collision, that is, $h > 0$ for all $t \ge 0$. In order to be more conservative, here we set the requirement $h - v\tau \ge 0$ for all $t \ge 0$ where $\tau > 0$ is the minimum time headway allowed. Corresponding to this we define the target set

$$\mathcal{T} = \{(h, v) | \, h - v\tau \ge 0\}, \tag{6.11}$$

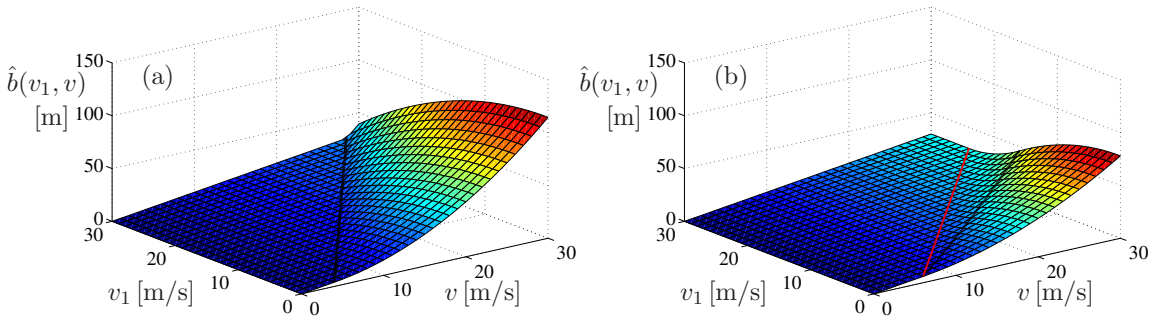

Figure 6.2: Surface of $\hat{b}(v_1, v)$ defining the safe distance for minimum time headway $\tau = 1$ [s]. The case given by (6.13) for with the black line indicating the switch (a) $\underline{a} = 4\,[\mathrm{m/s^2}]$ and $\underline{a}_1 = 6\,[\mathrm{m/s^2}]$ (6.14) . (b) The case given by (6.15) for $\underline{a} = 6\,[\mathrm{m/s^2}]$ and $\underline{a}_1 = 4\,[\mathrm{m/s^2}]$ with the black and red lines indicating the switches (6.16).

in state space. Thus, the safety requirement would correspond to the target set to be invariant: if the system starts in $\mathcal{T}$ it should stay in $\mathcal{T}$. However, it is easy to think of a scenario when this does not hold. Due to the limited deceleration capability of the follower (cf. (6.2)), for velocity v the distance needed to stop is $v^2/2\underline{a}$. When having a stationary vehicle within this distance, a collision is inevitable. Thus, the invariance of $\mathcal{T}$ can only be guaranteed if $v\tau \geq v^2/2\underline{a}$ for all v_1. This may require τ to be set to a few seconds which would result in unrealistically large distance headway.

In order to find a set in state space whose invariance can be ensured, we consider the scenario when the leader, initially traveling at speed v_1, applies its maximum deceleration $\underline{a}_1$. In the mean time, the follower, initially traveling at speed v, applies $\underline{a}$. Then, we investigate how the distance headway evolves between the vehicles before the follower comes to a halt and calculate how large the initial distance needs to be to avoid collision. Taking the maximum of this distance and $v\tau$ we obtain the set

$$\mathcal{C} = \{(h, v, v_1) |\, h - \hat{b}(v, v_1) \geq 0\}, \tag{6.12}$$

where $\hat{b}$ is defined as follows. If $\underline{a} \leq \underline{a}_1$ then we have

$$\hat{b}(v, v_1) = \begin{cases} v\tau, & \text{if} \quad v_1 \geq f_1(v), \\ v\tau + \frac{(v - \underline{a}\tau)^2}{2\underline{a}} - \frac{v_1^2}{2\underline{a}_1}, & \text{if} \quad v_1 < f_1(v), \end{cases} \tag{6.13}$$

where

$$f_1(v) = \sqrt{\frac{\underline{a}_1}{\underline{a}}}(v - \underline{a}\tau). \tag{6.14}$$

On the other hand, if $\underline{a} > \underline{a}_1$ then

$$\hat{b}(v, v_1) = \begin{cases} v\tau, & \text{if} \quad v_1 \geq f_2(v), \\ v\tau + \frac{(v-\underline{a}\tau-v_1)^2}{2(\underline{a}-\underline{a}_1)}, & \text{if} \quad f_2(v) < v_1 < f_3(v), \\ v\tau + \frac{(v-\underline{a}\tau)^2}{2\underline{a}} - \frac{v_1^2}{2\underline{a}_1}, & \text{if} \quad v_1 \geq f_3(v), \end{cases} \tag{6.15}$$

where

$$f_2(v) = v - \underline{a}\tau, \quad f_3(v) = \frac{\underline{a}_1}{\underline{a}}(v - \underline{a}\tau). \tag{6.16}$$

A detailed derivation may be found in [103]. Having different cases in (6.13) and (6.15) corresponds to the fact that the minimal distance headway may appear at different phases of the braking event: right at the moment when both vehicles launch the emergency brake, during the deceleration phase of the following vehicle, and at the end when the following vehicle stops.

Indeed, $\mathcal{C} \subseteq \mathcal{T}$ as can be observed in Figure 6.2 where we set the time headway $\tau = 1\,[\text{s}]$ and consider $\overline{v} = 30\,[\text{m/s}]$. Figure 6.2(a) corresponds to $\underline{a} \leq \underline{a}_1$, in particular, $\underline{a} = 4\,[\text{m/s}^2]$ and $\underline{a}_1 = 6\,[\text{m/s}^2]$. That is, the surface is given by (6.13) where (6.14) is indicated by a black line. On the other hand, Figure 6.2(b) corresponds to $\underline{a} > \underline{a}_1$, in particular, $\underline{a} = 6\,[\text{m/s}^2]$ and $\underline{a}_1 = 4\,[\text{m/s}^2]$. That is, the surface is given by (6.15) where (6.16) are indicated by red and a black lines.

At this point, our goal is to find conditions that a feedback law $u(h, v, v_1, a_1)$ has to satisfy in order to ensure the invariance of $\mathcal{C}$ under the closed-loop dynamics (6.4). For this, we utilize the concept of safety functions described in the next section.

6.2 Safety Functions for Set Invariance

In this section, we depart from the specific example of connected cruise control and propose a general theoretical framework for ensuring safety for a given feedback law. The logic flow is summarized in Figure 6.3.

Consider the affine control system

$$\dot{x} = f(x) + d + g(x)u, \tag{6.17}$$

where $x \in \mathbb{R}^n$ is the state, $d \in \mathcal{D} \subset \mathbb{R}^q$ is the disturbance and $u \in \mathcal{U} \subset \mathbb{R}^m$ is the control input, with $\mathcal{D}$ and $\mathcal{U}$ are compact sets, while f and g are locally Lipschitz continuous.

Given the Lipschitz continuous feedback law $u(x;p)$ where $p \in \mathbb{R}^r$ represents the control parameters, we obtain the closed loop system

$$\dot{x} = F(x;p) + d, \tag{6.18}$$

where $F(x;p) = f(x) + g(x)u(x;p)$.

Our goal is to find domain $\mathcal{P} \subset \mathbb{R}^r$ in the parameter space so that parameters $p \in \mathcal{P}$ guarantee the invariance of the closed set $\mathcal{C} \subset \mathbb{R}^n$ in state space under the dynamics (6.18). We refer to $\mathcal{C}$ as the safety set and refer to $\mathcal{P}$ as the safe parameter domain. The graphical representations of $\mathcal{P}$ are called safety charts. Moreover, we are also interested in designing controllers that can render the system safe even when $p \in \mathbb{R}^r \setminus \mathcal{P}$.

The safety set can be defined through the super-level set of the function $b : \mathbb{R}^n \mapsto \mathbb{R}$ such that

$$\begin{aligned} \mathcal{C} &= \{x \in \mathbb{R}^n : b(x) \geq 0\}, \\ \partial\mathcal{C} &= \{x \in \mathbb{R}^n : b(x) = 0\}, \\ \text{Int}\mathcal{C} &= \{x \in \mathbb{R}^n : b(x) > 0\}, \end{aligned} \tag{6.19}$$

where b is a continuously differentiable function or a continuous function constructed from finite number of continuously differentiable functions [103]. We recall the following definition from [102].

Definition 5. *Given a set $\mathcal{C} \in \mathbb{R}^n$ defined by* (6.19)*, the continuously differentiable function $b : \mathbb{R}^n \mapsto \mathbb{R}$ is a* safety function *if there exists an extended class $\mathcal{K}$ function π such that,*

$$\dot{b}(x) = L_{F+d}b(x) \geq -\pi(b(x)), \quad \forall\, x \in \mathbb{R}^n, \tag{6.20}$$

where L_{F+d} denotes the Lie derivative.

We recall that, a continuous function $\pi : [0, a) \mapsto [0, \infty)$ is of *class* $\mathcal{K}$ for some $a > 0$

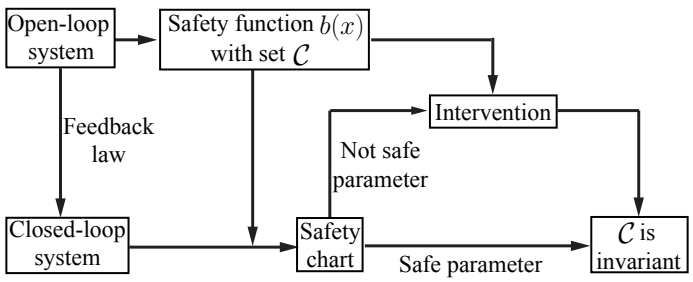

Figure 6.3: Ensuring safety of a given feedback law.

if it is strictly monotonically increasing and $\pi(0) = 0$. Moreover, a continuous function $\pi : (-b, a) \mapsto (-\infty, \infty)$ is of *extended class* $\mathcal{K}$ for some $a, b > 0$ if it is strictly monotonically increasing and $\pi(0) = 0$.

Seeking a safety function is usually challenging, particularly for a controller with non-trivial structure. Numerical techniques, such as sum of squares (SOS) programming, are usually used for complex cases. A safety function acquired this way may also lead to very conservative performance. This motivates us to go back to system (6.17) to find safety functions.

Definition 6. *Given a set* $\mathcal{C} \subset \mathbb{R}^n$ *defined by* (6.19) *the continuously differentiable function* $b : \mathbb{R}^n \mapsto \mathbb{R}$ *is a* control safety function *if there exists an extended class* $\mathcal{K}$ *function* π *such that*

$$\sup_{u \in \mathcal{U}} \left[L_{f+d} b(x) + L_g b(x) u + \pi(b(x)) \right] \geq 0, \quad \forall\, x \in \mathbb{R}^n. \tag{6.21}$$

The existence of a control safety function implies that there exist Lipschitz continuous controller $u : \mathbb{R}^n \mapsto \mathcal{U}$ such that the set $\mathcal{C}$ is invariant [102]. The intuition behind Definition 6 is that $\forall\, x \in \mathcal{C}$, there always exist control such that

$$\dot{b}(x) \geq -\pi\big(b(x)\big) \;\Rightarrow\; \dot{b}(x) \geq 0 \text{ if } b(x) = 0. \tag{6.22}$$

Compared to the safety function, control safety function describes the full capability of the system from safety perspective. Indeed, if one finds a control safety function for the open-loop systems it may be used as a safety function for the closed-loop systems as shown in Figure 6.3. In particular, we will use this function to determine the safe control parameters for the closed-loop systems and draw safety charts in parameter space. Using safe parameters $p \in \mathcal{P}$ in control law will result in the invariance of $\mathcal{C}$ in state space. Moreover, we will also utilize the control safety function to intervene in cases when one chooses control parameters outside the safe parameter regime. We remark that in the literature, safety functions and control safety functions are also referred as barrier functions and control barrier functions, respectively [102, 103, 105].

6.3 Connected Cruise Control with Safety Guarantee

In this section, we apply the method proposed in the previous section in order to ensure the safety of a given feedback law. In particular, we will provide a constructive method to derive the safe control parameters and represent these graphically using safety charts. We also present an algorithm that allows us to use parameters outside the safe parameter domain by intervening when the system approaches the boundary of the safety set.

Based on the definition of the set $\mathcal{C}$ in (6.12) we define the safety function candidate

$$b(h, v, v_1) = h - \hat{b}(v, v_1). \tag{6.23}$$

Then, by construction, the following conditions make (6.23) a control safety function according to Definition 6:

$$\mathcal{C} = \{(h, v, v_1) \mid b(h, v, v_1) \geq 0\} \neq \emptyset, \tag{6.24}$$

$$\sup_{u \in \mathcal{U}} \left[L_{f+d} b(h, v, v_1) + L_g b(h, v, v_1) u + \pi\big(b(h, v, v_1)\big) \right] \geq 0, \tag{6.25}$$

for $v, v_1 \in [0, \overline{v}], a_1 \in [-\underline{a}_1, \overline{a}_1]$ (cf. (6.2,6.3)) where π is a function of extended class $\mathcal{K}$.

Note that, by construction, (6.24,6.25) hold for $\pi(b(h, v, v_1)) = 0$, and therefore they hold for any function of extended class $\mathcal{K}$. Consequently, $b(h, v, v_1)$ is a control safety function and $\mathcal{C}$ is invariant under the dynamics (6.1) given $a \in [-\underline{a}, \overline{a}]$ (cf. (6.2)). In the next section we fix the system parameters $\underline{a}, \overline{a}, \underline{a}_1, \overline{a}_1, \tau$ and apply (6.25) in order to derive conditions for the feedback law $u(h, v, v_1, a_1)$ that ensures the invariance of $\mathcal{C}$.

6.3.1 Safety charts

With the control safety function (6.23), and given a feedback law $u(h, v, v_1, a_1)$, we present the main theorem that certifies the safety of the connected cruise controller.

Theorem 4. *Given a continuous and piecewise continuously differentiable feedback law* $u(h, v, v_1, a_1)$ *such that*

$$U \geq \frac{\partial u}{\partial h} \geq 0, \tag{6.26}$$

for some $U > 0$*, a piecewise continuously differentiable safety function* $b(h, v, v_1) = h - \hat{b}(v, v_1)$ *such that*

$$\frac{\partial \hat{b}}{\partial v} > 0, \tag{6.27}$$

for $v \neq 0$*, and*

$$v_1 - v - \frac{\partial \hat{b}}{\partial v_1} a_1 - \frac{\partial \hat{b}}{\partial v} \mathrm{sat}\Big(u\big(\hat{b}(v, v_1), v, v_1, a_1\big)\Big) \geq 0, \tag{6.28}$$

then there exists an extended class $\mathcal{K}$ *function* π *such that*

$$L_{F+d} b(h, v, v_1) \geq -\pi(b(h, v, v_1)) \tag{6.29}$$

holds and thus, $\mathcal{C}$ is invariant under (6.4).

The proof of Theorem 4 can be given by using a linear function for π.

Proof. Both $\hat{b}(v, v_1)$ and $u(h, v, v_1, a_1)$ are piecewise continuously differentiable. They take value from a compact set $v,\ v_1 \in [0, \overline{v}]$, despite h may be unbounded from above. Thus, $\frac{\partial \hat{b}}{\partial v}$ is bounded; see (6.27). Since $\frac{\partial u}{\partial h}$ has an upper bound U (see (6.26)), then for $b(h, v, v_1) = h - \hat{b}(v, v_1) \geq 0$, we have

$$\begin{aligned} Ub(h, v, v_1) &= U(h - \hat{b}(v, v_1)) \\ &\geq u\left(h, v, v_1, a_1\right) - u\big(\hat{b}(v, v_1), v, v_1, a_1\big), \end{aligned} \tag{6.30}$$

where the equality holds only when $b(h, v, v_1) = h - \hat{b}(v, v_1) = 0$. Now considering the sat$(\cdot)$ function, if $u\big(\hat{b}(v, v_1), v, v_1, a_1\big) \geq \overline{a} > 0$ or $u\big(h, v, v_1, a_1\big) \leq -\underline{a} < 0$, then

$$\begin{aligned} &u(h, v, v_1, a_1) - u\big(\hat{b}(v, v_1), v, v_1, a_1\big) \\ \geq &\,\text{sat}\Big(u\big(h, v, v_1, a_1\big)\Big) - \text{sat}\Big(u\big(\hat{b}(v, v_1), v, v_1, a_1\big)\Big) = 0. \end{aligned} \tag{6.31}$$

Otherwise, having $u\big(\hat{b}(v, v_1), v, v_1, a_1\big) < \overline{a}$ and $u(h, v, v_1, a_1) > -\underline{a}$ yields

$$\begin{aligned} &u(h, v, v_1, a_1) - u\big(\hat{b}(v, v_1), v, v_1, a_1\big) \\ \geq &\,\text{sat}\Big(u\big(h, v, v_1, a_1\big)\Big) - u\big(\hat{b}(v, v_1), v, v_1, a_1\big) \\ \geq &\,\text{sat}\Big(u\big(h, v, v_1, a_1\big)\Big) - \text{sat}\Big(u\big(\hat{b}(v, v_1), v, v_1, a_1\big)\Big). \end{aligned} \tag{6.32}$$

Thus, one has

$$\begin{aligned} &Ub(h, v, v_1) \\ &\geq u(h, v, v_1, a_1) - u\big(\hat{b}(v, v_1), v, v_1, a_1\big) \\ &\geq\ \text{sat}\Big(u\big(h, v, v_1, a_1\big)\Big) - \text{sat}\Big(u\big(\hat{b}(v, v_1), v, v_1, a_1\big)\Big) \end{aligned} \tag{6.33}$$

where again the equality holds only when $b(h, v, v_1) = h - \hat{b}(v, v_1) = 0$.

By selecting the linear extended class $\mathcal{K}$ function $\pi(y) = \gamma\, y$ such that

$$\gamma \geq U \max_{v, v_1 \in [0, \overline{v}]} \frac{\partial \hat{b}}{\partial v}, \tag{6.34}$$

we have

$$
\begin{aligned}
&L_{F+d}b(h,v,v_1) + \gamma\, b(h,v,v_1) \\
=&\dot{h} - \frac{\partial \hat{b}}{\partial v}\dot{v} - \frac{\partial \hat{b}}{\partial v_1}\dot{v}_1 + \gamma\, b(h,v,v_1) \\
=&v_1 - v - \frac{\partial \hat{b}}{\partial v_1}a_1 - \frac{\partial \hat{b}}{\partial v}\text{sat}\Big(u\big(h,v,v_1,a_1\big)\Big) \\
&+ \left(\gamma - U\frac{\partial \hat{b}}{\partial v} + U\frac{\partial \hat{b}}{\partial v}\right)b(x) \\
=&v_1 - v + \underbrace{\left(\gamma - U\frac{\partial \hat{b}}{\partial v}\right)}_{\geq 0} b(x) - \frac{\partial \hat{b}}{\partial v_1}a_1 \\
&- \frac{\partial \hat{b}}{\partial v}\Bigg[\text{sat}\Big(u\big(\hat{b}(v,v_1),v,v_1,a_1\big)\Big) + \\
&\underbrace{\text{sat}\Big(u\big(h,v,v_1,a_1\big)\Big) - \text{sat}\Big(u\big(\hat{b}(v,v_1),v,v_1,a_1\big)\Big) - Ub(h,v,v_1)}_{\leq 0}\Bigg] \\
\geq&v_1 - v - \frac{\partial \hat{b}}{\partial v_1}a_1 - \frac{\partial \hat{b}}{\partial v}\text{sat}\Big(u\big(\hat{b}(v,v_1),v,v_1,a_1\big)\Big),
\end{aligned}
\tag{6.35}
$$

where the equality at last step holds only when $b(h,v,v_1) = h - \hat{b}(v_1,v) = 0$. Note that (6.35) gives condition (6.29) at $b(h,v,v_1) = 0$. □

One may show that in fact

$$
u\big(\hat{b}(v,v_1),v,v_1,a_1\big) \leq -\underline{a}, \tag{6.36}
$$

implies $L_{F+d}b(h,v,v_1) \geq 0$ for the safety function (6.23) with definition (6.13) and also with definition (6.15). Consequently, this is a sufficient condition for (6.29) and implies the invariance of $\mathcal{C}$. Based on this we will use

$$
\max_{v,v_1}\Big[u\big(\hat{b}(v,v_1),v,v_1,a_1\big)\Big] \leq -\underline{a}, \tag{6.37}
$$

to find control parameters that ensure safety.

For example, given the controller (6.10) we are searching for the parameters $p = [\alpha,\beta,\kappa,h_{\text{st}}]$ such that

$$
\max_{v,v_1}\Big[\alpha\big(\kappa(\hat{b}(v,v_1) - h_{\text{st}}) - v\big) + \beta(v_1 - v)\Big] \leq -\underline{a}. \tag{6.38}
$$

For the sake of presentation, we assume α, β and τ are given and draw safety charts in the $(h_{\rm st}, \kappa)$-plane. Before providing the corresponding detailed conditions, we remark that one needs

$$\kappa < 1/\tau, \tag{6.39}$$

in order to obtain a meaningful controller as κ determines the time headway in equilibrium.

We recall that $\hat{b}(v, v_1)$ is given by different analytical formulae in different domains of the (v, v_1) space; cf. (6.13,6.15). The maximum of (6.38) may occur either in the interior of these domains or at the boundaries of these domains given by (6.3,6.14,6.16).

In case $\underline{a} \leq \underline{a}_1$ the results are summarized in Tables 6.1,6.2,6.3. In particular, Table 6.1 is for $\hat{b}(v, v_1) = v\tau$ while Tables 6.2 and 6.3 are for $\hat{b}(v, v_1) = v\tau + \frac{(v-\underline{a}\tau)^2}{2\underline{a}} - \frac{v_1^2}{2\underline{a}_1}$. When $\underline{a} > \underline{a}_1$ the results are summarized in Tables 6.1 and 6.4. Again Table 6.1 correspond to $\hat{b}(v, v_1) = v\tau$ while Table 6.4 is for $\hat{b}(v, v_1) = v\tau + \frac{(v-\underline{a}\tau-v_1)^2}{2(\underline{a}-\underline{a}_1)}$ and $\hat{b}(v, v_1) = v\tau - \frac{(v-\underline{a}\tau)^2}{2\underline{a}} - \frac{v_1^2}{2\underline{a}_1}$. These two cases can be brought together since the former function is convex in its domain and the maximum appears at the boundary $v_1 = f_3(v)$. Thus, it is enough to consider (6.38) only when $v_1 \leq f_3(v)$.

if α, β, τ	then $h_{\rm st}, \kappa$
$1-(\beta+\alpha)\tau \geq 0$	$\alpha\kappa(h_{\rm st} - \underline{a}\tau^2) \geq \underline{a}\big(1-\beta\tau-\alpha\tau\big)$
$\beta\tau - 1 \geq 0$	$\alpha\kappa h_{\rm st} \geq \overline{a}(\tau\beta - 1)$ and $\kappa\tau < 1$
$\beta\tau - 1 < 0$ and $1-(\beta+\alpha)\tau < 0$	either $h_{\rm st} \geq \underline{a}\tau^2$ or $\alpha\kappa(\underline{a}\tau^2 - h_{\rm st}) \leq \underline{a}\big((\beta+\alpha)\tau - 1\big)$

Table 6.1: Safety conditions when $\hat{b}(v, v_1) = v\tau$ independent of the relation between $\underline{a}_1$ and $\underline{a}$.

if $\alpha, \beta, \tau, \kappa$	then $h_{\rm st}$
$\alpha > 0, \beta > 0, \tau > 0,$ and $\kappa \geq \frac{\beta\underline{a}_1}{\alpha\overline{\overline{v}}}$	$\alpha\kappa\left(\overline{v}\tau + \frac{(\overline{v}-\underline{a}\tau)^2}{2\underline{a}} - h_{\rm st}\right)$ $+\frac{\beta^2\underline{a}_1}{2\alpha\kappa} - (\alpha+\beta)\overline{v} \leq -\underline{a}$
$\alpha > 0, \beta > 0, \tau > 0,$ and $\kappa < \frac{\beta\underline{a}_1}{\alpha\overline{\overline{v}}}$	$\alpha\kappa\left(\overline{v}\tau + \frac{(\overline{v}-\underline{a}\tau)^2}{2\underline{a}} - \frac{\overline{\overline{v}}^2}{2\underline{a}_1} - h_{\rm st}\right)$ $-\alpha\overline{v} + \beta(\overline{\overline{v}} - \overline{v}) \leq -\underline{a}$

Table 6.2: Safety conditions when $\underline{a} \leq \underline{a}_1$ and $\hat{b}(v, v_1) = v\tau + \frac{(v-\underline{a}\tau)^2}{2\underline{a}} - \frac{v_1^2}{2\underline{a}_1}$ along the boundary $v = \overline{v}$.

We remark that the conditions summarized in the above tables give non-empty sets of $\alpha, \beta, \tau, \kappa, h_{\rm st}$. In particular, choosing sufficiently small κ and sufficiently large $h_{\rm st}$ ensures

if α, β, τ	then h_{st}, κ
$\alpha+\beta<\beta\sqrt{\frac{\underline{a}_1}{\underline{a}}}$	$\alpha\kappa(h_{\mathrm{st}}-\tau\hat{\overline{v}}-\underline{a}\tau^2)\geq$ $\left(\beta\sqrt{\frac{\underline{a}_1}{\underline{a}}}-(\alpha+\beta)\right)\hat{\overline{v}}+\underline{a}(1-\beta\tau-\alpha\tau)$
$\alpha+\beta>\beta\sqrt{\frac{\underline{a}_1}{\underline{a}}}$	either $\alpha\kappa\tau\leq\alpha+\beta-\beta\sqrt{\frac{\underline{a}_1}{\underline{a}}}$ and $\alpha\kappa(h_{\mathrm{st}}-\underline{a}\tau^2)\geq\underline{a}\big(1-\beta\tau-\alpha\tau\big)$ or $\alpha\kappa\tau>\alpha+\beta-\beta\sqrt{\frac{\underline{a}_1}{\underline{a}}}$ and $\alpha\kappa(h_{\mathrm{st}}-\tau\hat{\overline{v}}-\underline{a}\tau^2)\geq$ $\left(\beta\sqrt{\frac{\underline{a}_1}{\underline{a}}}-(\alpha+\beta)\right)\hat{\overline{v}}+\underline{a}(1-\beta\tau-\alpha\tau)$

Table 6.3: Safety conditions when $\underline{a}\leq\underline{a}_1$ and $\hat{b}(v,v_1)=v\tau+\frac{(v-\underline{a}\tau)^2}{2\underline{a}}-\frac{v_1^2}{2\underline{a}_1}$ along the boundary $v_1=f_1(v)$.

if $\alpha, \beta, \tau, \kappa$	then h_{st}
$\alpha>0, \beta>0, \tau>0,$ and $\kappa\geq\frac{\beta\underline{a}_1}{\alpha\overline{v}}$	$\alpha\kappa\left(\frac{(\overline{v}-\underline{a}\tau)^2}{2\underline{a}}+\overline{v}\tau-h_{\mathrm{st}}\right)$ $+\frac{\beta^2\underline{a}_1}{2\alpha\kappa}-(\alpha+\beta)\overline{v}\leq-\underline{a}$
$\alpha>0, \beta>0, \tau>0,$ and $\kappa<\frac{\beta\underline{a}_1}{\alpha\overline{v}}$	$\alpha\kappa\left(\frac{\underline{a}-\underline{a}_1}{2\underline{a}}(\overline{v}-\underline{a}\tau)^2+\overline{v}\tau-h_{\mathrm{st}}\right)$ $-(\alpha+\beta)\overline{v}+\beta\frac{\underline{a}_1}{\underline{a}}\overline{v}\leq-\underline{a}$

Table 6.4: Safety conditions when when $\underline{a}>\underline{a}_1$ and $\hat{b}(v,v_1)\neq v\tau$.

safety. In the tables we also used the notation

$$\begin{aligned}\hat{\overline{v}}&=\min\left\{(\overline{v}-\underline{a}\tau)\sqrt{\frac{\underline{a}_1}{\underline{a}}},\overline{v}\right\},\\ \hat{\overline{v}}&=\min\left\{\overline{v}-\underline{a}\tau,\overline{v}\sqrt{\frac{\underline{a}}{\underline{a}_1}}\right\}.\end{aligned}\tag{6.40}$$

As an example, we pick a set of control parameter $\alpha=0.4\,[1/\mathrm{s}]$, $\beta=0.5\,[1/\mathrm{s}]$, $\tau=1\,[\mathrm{s}]$, $\kappa=0.6\,[1/\mathrm{s}]$, $h_{\mathrm{st}}=5\,[\mathrm{m}]$ that were used in a real experiment [46]. The acceleration limits are given as $\overline{a}=\overline{a}_1=2\,[\mathrm{m/s^2}]$, $\underline{a}=4\,[\mathrm{m/s^2}]$, $\underline{a}_1=6\,[\mathrm{m/s^2}]$ which correspond to Tables 6.1, 6.2, 6.3. The safety chart is plotted in the (h_{st},κ)-plane in Figure 6.4, where the curves corresponds to the different limits given in the tables and shading indicates the region of safe parameters. The corresponding color code is explained in Table 6.5.

In order to show the difference between the safe and unsafe parameter combinations we mark some point inside the safe parameter region (green cross at $\kappa=0.4\,[1/\mathrm{s}]$, $h_{\mathrm{st}}=10\,[\mathrm{m}]$) and another outside (red cross at $\kappa=0.6\,[1/\mathrm{s}]$, $h_{\mathrm{st}}=5\,[\mathrm{m}]$) in Figure 6.4. We plot the corresponding simulation results in Figure 6.5 and Figure 6.6 as red solid and green dashed-dotted curves, respectively. In particularly, we exam two different two different

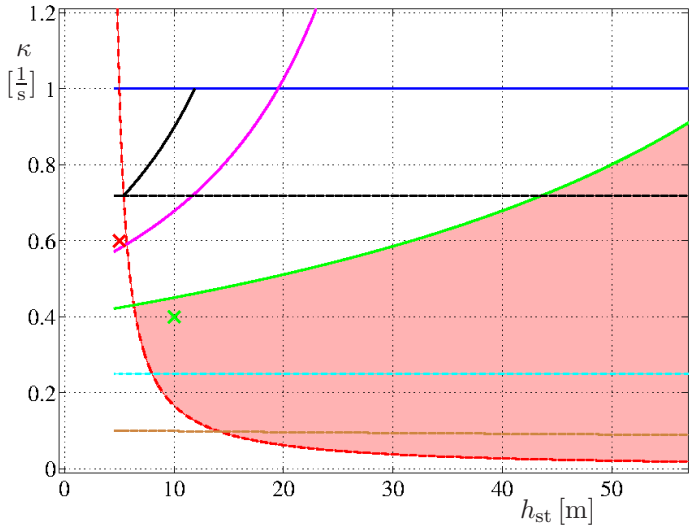

Figure 6.4: Safety chart for $\underline{a}_1 = 6\,[\text{m/s}^2]$, $\underline{a} = 4\,[\text{m/s}^2]$, $\tau = 1\,[\text{s}]$, $\alpha = 0.4\,[1/\text{s}]$, and $\beta = 0.5\,[1/\text{s}]$. The red shaded region corresponds safe (h_{st}, κ) combinations. The blue solid line corresponds to (6.39). For the mean of the rest curves, see Table 6.5.

since α, β, τ	$1 - (\beta + \alpha)\tau \geq 0$
then h_{st}, κ	$\alpha\kappa(h_{\text{st}} - \underline{a}\tau^2) \geq \underline{a}\big(1 - \beta\tau - \alpha\tau\big)$ (red dashed)

if κ (cyan)	then h_{st}
$\kappa \geq \frac{\beta \underline{a}_1}{\alpha \overline{v}}$	$\alpha\kappa\left(\overline{v}\tau + \frac{(\overline{v} - \underline{a}\tau)^2}{2\underline{a}} - h_{\text{st}}\right)$ (between green $+\frac{\beta^2 \underline{a}_1}{2\alpha\kappa} - (\alpha + \beta)\overline{v} \leq -\underline{a}$ and brown solid)
$\kappa < \frac{\beta \underline{a}_1}{\alpha \overline{v}}$	$\alpha\kappa\left(\overline{v}\tau + \frac{(\overline{v} - \underline{a}\tau)^2}{2\underline{a}} - \frac{\overline{v}^2}{2\underline{a}_1} - h_{\text{st}}\right) \leq \alpha\overline{v} - \underline{a}$ (magenta)

since α, β	$\alpha + \beta > \beta\sqrt{\frac{\underline{a}_1}{\underline{a}}}$
then h_{st}, κ	either $\alpha\kappa\tau \leq \alpha + \beta - \beta\sqrt{\frac{\underline{a}_1}{\underline{a}}}$ (black dashed) and $\alpha\kappa(h_{\text{st}} - \underline{a}\tau^2) \geq \underline{a}\big(1 - \beta\tau - \alpha\tau\big)$ (red dashed)
	or $\alpha\kappa\tau > \alpha + \beta - \beta\sqrt{\frac{\underline{a}_1}{\underline{a}}}$ (black dashed) and $\alpha\kappa\left(h_{\text{st}} - \overline{v}\sqrt{\frac{\underline{a}}{\underline{a}_1}} - \underline{a}\tau^2\right) \geq$ (black solid) $\left(\beta\sqrt{\frac{\underline{a}_1}{\underline{a}}} - (\alpha + \beta)\right)\overline{v}\sqrt{\frac{\underline{a}}{\underline{a}_1}} + \underline{a}(1 - \beta_1\tau - \alpha\tau)$

Table 6.5: Safety conditions when $\underline{a}_1 = 6\,[\text{m/s}^2]$, $\underline{a} = 4\,[\text{m/s}^2]$, $\tau = 1\,[\text{s}]$, $\alpha = 0.4\,[1/\text{s}]$, and $\beta = 0.5\,[1/\text{s}]$. The color codes correspond to those in Figure 6.4.

scenarios. The first scenario starts from a traffic equilibrium: both vehicles travel with the same speed and an ideal distance is kept. The predecessor's velocity profile v_1 is shown in panel Figure 6.5(a) as a black curve. After a constant-speed plateau at 30 [m/s] the

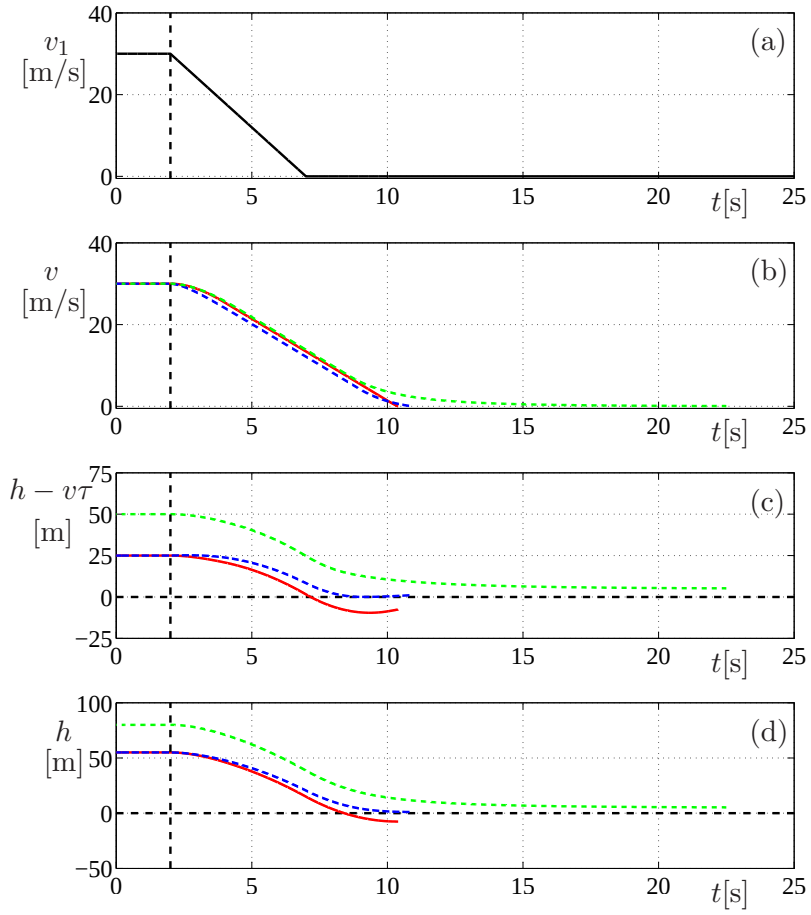

Figure 6.5: Simulation results when a safety critical events occur from a traffic equilibrium. The predecessor applies heavy braking as shown by the speed profile in panel (a). The green and the red profiles in panels (b,c,d) correspond to the safe and unsafe parameter combinations marked by a green and red crosses in Figure 6.4. The blue profiles also correspond to the unsafe combination but with the intervening controller (6.43).

predecessor applies maximum braking with $-6\,[\text{m/s}^2]$. Initially the following vehicle is traveling with speed $v = 30\,[\text{m/s}]$ and the initial distance between the two vehicles are given by $h = V(v)$, which equals to 80 [m] and 50 [m] for the chosen κ, h_{st} combinations; cf. (6.6). Panels (b,c,d) show the time profiles for v, $h - v\tau$, h. While the unsafe controller leads to collision, the safe controller is able to bring the vehicle slowly to a stop. The second scenario mimic a "cut-in" event: a slower traveling vehicle suddenly appear at the front. As shown in Figure 6.6(a) after a constant-speed plateau at 14 [m/s] the predecessor applies maximum braking with $-6\,[\text{m/s}^2]$. Initially the following vehicle is traveling with speed $v = 30\,[\text{m/s}]$ and the initial distance between the two vehicles is given by $h = \hat{b}(v_1, v) = 98.17\,[\text{m}]$. As see in panels (b,c,d) in Figure 6.6, the unsafe controller leads to collision, but the safe controller is still able to bring the vehicle slowly to a stop.

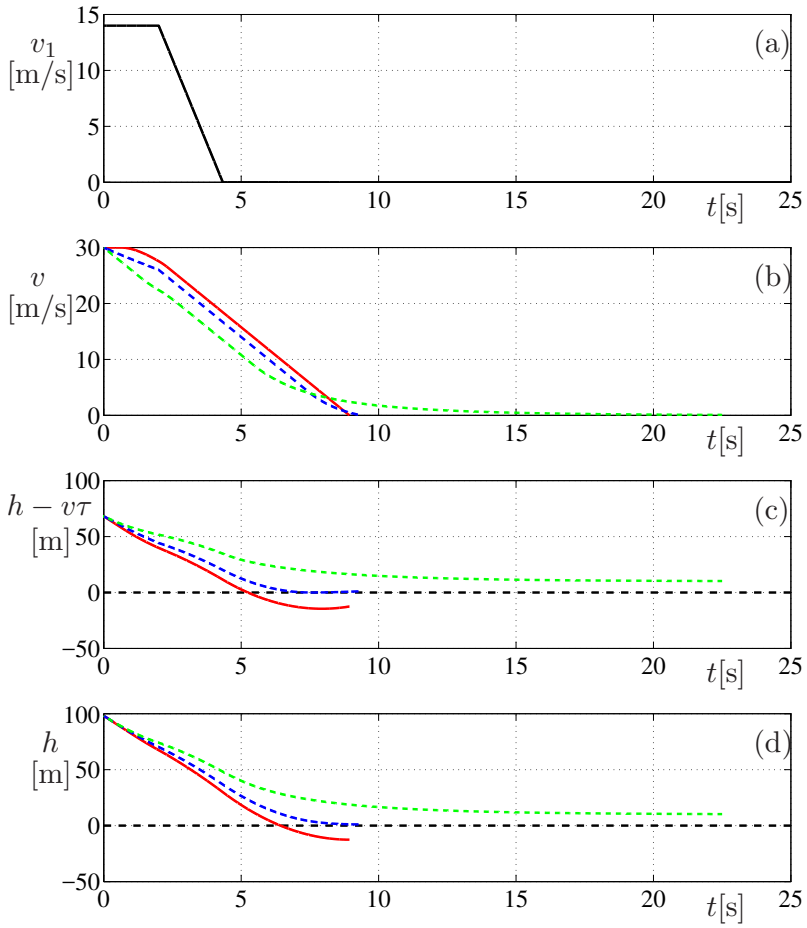

Figure 6.6: Simulation results when a safety critical events occur after a slower preceding vehicle appears in the front. The predecessor applies heavy braking as shown by the speed profile in panel (a). The dashed green and the solid red curves in panels (b,c,d) correspond to the safe and unsafe parameter combinations marked by a green and red crosses in Figure 6.4. The blue profiles also correspond to the unsafe combination but with the intervening controller (6.43).

6.3.2 Intervening controller

While the safety charts allowed us to select safe control parameters, the corresponding connected cruise control algorithm tends to keep large distances. This may not be feasible heavy traffic scenarios as it may "invite" other road users to cut in front of the vehicle. In order to resolve this issue one may prefer to choose parameter combinations outside the safe parameter region. In this section we propose an intervention that overrides the feedback law once non-safe situations are detected.

Recall that the invariance of the safety set $\mathcal{C}$ is guaranteed once (6.29) holds which is ensured by (6.28). Similar to the proof of Theorem 4 shown in Section 6.3.1, we choose the extended class $\mathcal{K}$ function to be linear $\pi(y) = \gamma\, y$ and propose the control law

$$\begin{aligned} &\hat{u}(h, v, v_1, a_1) \\ &= \left(\frac{\partial \hat{b}}{\partial v}\right)^{-1} \left(v_1 - v - \frac{\partial \hat{b}}{\partial v_1} a_1 + \gamma\big(h - \hat{b}(v, v_1)\big)\right) \end{aligned} \tag{6.41}$$

that is applied when

$$L_{F+d} b(h, v, v_1) + \gamma\, b(h, v, v_1) \leq 0. \tag{6.42}$$

Then, the enhanced controller is given by

$$\min\big\{u(h, v, v_1, a_1), \hat{u}(h, v, v_1, a_1)\big\}. \tag{6.43}$$

We show the result of this enhanced controller while choosing u according to the feedback law (6.10) and setting

$$\gamma \geq \alpha\kappa \max\left\{\tau, \frac{\overline{v}}{\underline{a}}\right\}, \tag{6.44}$$

according to (6.34) in the proof of Theorem 4. We present the corresponding simulation results as blue dashed curves in Figure 6.5 and Figure 6.6 for the unsafe parameters ($\kappa = 0.6$ [1/s], $h_{\mathrm{st}} = 5$ [m]) marked by the red cross in Figure 6.4 while using $\gamma = 1.8$ that satisfies (6.44). For both scenarios, apart from being able to maintain safety, the enhanced controller also provides a faster response compared to the one with safe parameters (green dashed-dotted curves).

6.4 Summary

In this chapter, we investigated the safety of a predecessor-follower system with connected cruise control. We proposed a theoretical framework to evaluate the safety of a given

control law using the notion of control safety function. The concept of safety chart was established in order to help the selection of control parameters that guarantee collision-free motion and an intervening scheme was establish to handle unsafe parameters. With the safety chart concept, as well as the intervening scheme, allocation between the fuel saving techniques introduced at vehicle level (in Chapter 4) and traffic level (in Chapter 5) can be carried out with safety guarantee.

CHAPTER 7

Conclusion and Future Work

We can only see a short distance ahead, but we can see plenty there that needs to be done.

ALAN M. TURING

7.1 Conclusion

In this dissertation, a series of techniques was proposed to improve the fuel economy of heavy-duty vehicles using connectivity and automation. These techniques were targeting fuel saving at different levels, from powertrain design, up to vehicle motion control in sparse as well as dense traffic conditions. Each technique was demonstrated to result in fuel benefit.

Starting from the powertrain level, in Chapter 3 a hybrid approach was proposed to design a safe and stable gear shift schedule for automated vehicles. This gear shift schedule is shown to result in a fuel-saving of 3-5% for a given powertrain compared to the benchmark in-production design. This improvement is demonstrated in simulation when the truck is driven over standard EPA driving cycles, with no compromises to driveability. The proposed design was also shown to be compatible with the human-driven case as well. Furthermore, it was demonstrated that when geographical, traffic conditions are utilized in motion planning algorithms of automated vehicles, the proposed design may lead to more significant improvements.

Based on the findings at the powertrain level, a systematic tool for geographic previewed eco-driving system was developed at the vehicle level in Chapter 4. Using this tool, a connected automated truck can achieve around 10% fuel economy improvement given freeway driving or mild traffic conditions compared to standard non-preview cruise control. A further benefit is that the trade-offs between different objectives (e.g., traveling time, fuel economy, traffic flow merging) can be evaluated and controlled. However,

when the traffic is dense, fuel improvement may not be fully attainable, which demanded a technique that works in such conditions.

To address this issue, at the traffic level, when the connected automated truck is driven in dense traffic, a data-driven optimization method was developed in Chapter 5. This technique utilized beyond-line-of-sight traffic information. Using real traffic data, it was found that a connected automated truck with optimal connected cruise control can save 5-13% fuel compared to the traditional adaptive cruise control that does not use beyond-light-of-sight information.

The results presented in this dissertation can be applied to in-production trucks for fuel savings. Also, the novel design analysis and application of nonlinear control theory, optimal control, control safety function can be executed in control design and applications in a general sense.

7.2 Future work

Despite the fuel savings resulting from the techniques proposed in this dissertation individually, integrations are still needed to unify the overall propulsion system of a connected automated truck. Specifically, due to the relatively small design scale, both in terms of time and distance (a few seconds and few dozens of meters), the connected cruise control design at the traffic level may be insufficient to include a large scale geographic preview needed at the vehicle level (a few kilometers and few minutes). Moreover, how to integrate these techniques together in a safe manner is also an important task.

Preliminary attempts to integrate the technologies used at the different levels in a safe manner were also made, as presented in Chapter 6. A safety verification theory is developed for connected cruise control; the notion of minimal intervention was proposed to allocate the use of techniques at both the vehicle level and traffic level. Indeed, this minimal intervention was demonstrated to ensure a collision free connected cruise control design.

Preliminary simulation results also showed that the minimum intervention technique may combine the fuel saving potential by individual techniques to maximize the overall fuel-saving for certain traffic conditions, while still keeping the vehicle safe. In the future, it important to understand how to adjust such minimum intervention under different traffic conditions while maintaining safety. Furthermore, future integrations of these techniques using minimum intervention should be applied to real in-service trucks and tested out in real daily traffic scenarios, so as to fully evaluate their performance.

APPENDIX A

Pseudo arclength continuation method

Our BVP solver developed is based on pseudo arclength continuation. Given a BVP problem, the solver first uses a collocation method to transform the continuous ODE to a set of nonlinear equations. Consider the BVP in the form

$$\begin{aligned} \dot{x} &= f(x, t; p), \qquad t \in [0, t_{\mathrm{f}}], \\ 0 &= g(x(0), x(t_{\mathrm{f}}); p), \end{aligned} \tag{A.1}$$

where $x \in \mathbb{R}^n$ is the state and $p \in \mathbb{R}$ is the system parameter. The boundary condition g contains n equations, assuming that the terminal time t_{f} is given.

We define N collocation points $x(t_i) = x_i$ at time $t_i = i \cdot \frac{t_{\mathrm{f}}}{N-1}$, $i = 0, 1, \ldots, N-1$. Using the *trapezoidal rule*, we arrive at the algebraic equations

$$\begin{aligned} x_{i+1} - x_i &= \frac{t_{\mathrm{f}}}{2(N-1)} \Big[f(x_{i+1}, t_{i+1}; p) + f(x_i, t_i; p) \Big], \\ 0 &= g(x_0, x_N; p). \end{aligned} \tag{A.2}$$

Therefore the collocation method of order N transforms the original BVP to a nonlinear equation problem of dimension Nn that can be written to the form:

$$F(\mathbf{x}, p) = 0, \tag{A.3}$$

where $\mathbf{x} \in \mathbb{R}^{Nn}$ contains all the component $x_i \in \mathbb{R}^n$, $i = 0, \ldots, N-1$. Note that the terminal time t_{f} may be a variable as well, and in this case g shall contain $n+1$ equations, and the resulting nonlinear equations will be of dimension $Nn + 1$.

The key idea behind continuation is that one may solve the BVP for a particular value of p and then use the corresponding solution as an initial guess when solving the BVP for the nearby parameter $p + \delta p$. This way the solution can be continued while the parameter is varied [106]. Continuation is based on the implicit function theorem, which guarantees that

(A.3) can be solved for $x(p)$. However, there may be points where implicit function theorem is violated. For example, in Figure A.1, the curve (A.3) is shown in the $(p, \|\mathbf{x}\|)$-plane. The implicit function theorem is violated at the fold points where the partial derivative of F with respect to $\mathbf{x}$ is 0. In order to be able to continue the curve through these points, we apply the so-called pseudo arc-length continuation method [107]. Throughout the descrip-

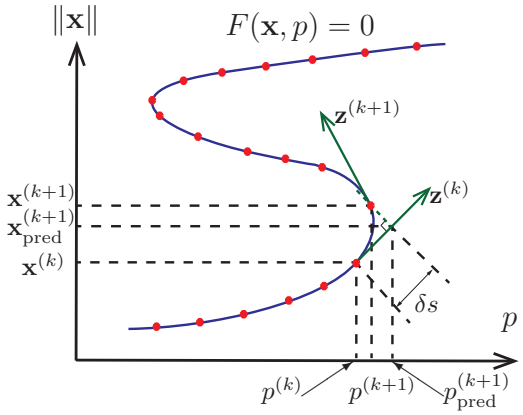

Figure A.1: Concept of the Pseudo Arc-length Method

tion of the algorithm, we use the subscript k to denote the iteration number. In the k-th iteration, the point $(\mathbf{x}^{(k)}, p^{(k)})$ lies on the curve with tangent vector $\mathbf{z}^{(k)}$. Let us consider the arc-length step δs.

Then we follow the steps:

1. Compute the a predicted value for the $(k+1)$-st step

$$\begin{bmatrix} \mathbf{x}_{\text{pred}}^{(k+1)} \\ \\ p_{\text{pred}}^{(k+1)} \end{bmatrix} = \begin{bmatrix} \mathbf{x}^{(k)} \\ \\ p^{(k)} \end{bmatrix} + \mathbf{z}^{(k)} \delta s. \tag{A.4}$$

2. Solve the following system of augmented nonlinear equations

$$\begin{aligned} 0 &= F(\mathbf{x}^{(k+1)}, p^{(k+1)}), \\ 0 &= {\mathbf{z}^{(k)}}^{\mathrm{T}} \cdot \begin{bmatrix} \mathbf{x}^{(k+1)} - \mathbf{x}_{\text{pred}}^{(k+1)} \\ \\ p^{(k+1)} - p_{\text{pred}}^{(k+1)} \end{bmatrix}, \end{aligned} \tag{A.5}$$

   for $(\mathbf{x}^{(k+1)}, p^{(k+1)})$ given $(\mathbf{x}_{\text{pred}}^{(k+1)}, p_{\text{pred}}^{(k+1)})$.

3. Find the tangent $\mathbf{z}^{(k+1)}$ to the curve for the $(k+1)$-st point by solving the linear equations

$$\begin{bmatrix} \frac{\partial F}{\partial \mathbf{x}}(\mathbf{x}^{(k+1)}, p^{(k+1)}), & \frac{\partial F}{\partial p}(\mathbf{x}^{(k+1)}, p^{(k+1)}) \\ & \\ & {\mathbf{z}^{(k)}}^{\mathrm{T}} \end{bmatrix} \mathbf{z}^{(k+1)} = \begin{bmatrix} 0 \\ \vdots \\ 0 \\ 1 \end{bmatrix}, \tag{A.6}$$

   with $\quad \|\mathbf{z}^{(k+1)}\| = 1.$

In this chapter, we use the classical Newton method [108] to solve the nonlinear algebraic equations (A.5). These steps are demonstrated in Figure A.1. It can be seen that the pseudo arc-length continuation method may allow one to continue curve through the fold points. Finally, we remark that the step size δs can be adapted during the process, e.g., can be chosen larger where (A.3) is "flat".

APPENDIX B

Approximating the energy consumption

In this Appendix we provide the detailed derivation of the cost function (5.22).

Recall the truck's speed response (5.20) for a certain parameter set $\mathbf{p}_n$, we have

$$v(t) = v^* + \tilde{v}(t) = v^* + \sum_{j=1}^{m} D_j \sin(\omega_j t + \theta_j), \tag{B.1}$$

where $t \in [t_0, t_\mathrm{f}]$, $\omega_j = j\Delta\omega$, $j = 1, \ldots, m$, and $\Delta\omega = 2\pi/(t_\mathrm{f} - t_0)$. Correspondingly, the acceleration of the truck is

$$\dot{v}(t) = \sum_{j=1}^{m} D_j \omega_j \cos(\omega_j t + \theta_j). \tag{B.2}$$

Note that the nonlinear function $g(x) = \max(x, 0)$ in (5.7) can be approximated by

$$\hat{g}(x) = \frac{1}{2}\left(x + \frac{x^2}{\sqrt{\varepsilon + x^2}}\right), \tag{B.3}$$

for small $\varepsilon > 0$.

Since the energy consumption due to physical effects $f(v)$ is shown to be small in Figure 5.3, we may omit $f(v)$ and approximate the total energy consumption (5.7) by

$$\hat{w} = \int_{t_0}^{t_\mathrm{f}} v\, \hat{g}\big(\dot{v}\big)\, \mathrm{d}t = \frac{1}{2}\int_{t_0}^{t_\mathrm{f}} \frac{v\, \dot{v}^2}{\sqrt{\varepsilon + \dot{v}^2}}\, \mathrm{d}t\,. \tag{B.4}$$

Note that

$$\dot{v}^2 = \sum_{j,k=1}^{m} D_j D_k \omega_j \omega_k \cos(\omega_j t + \theta_j)\cos(\omega_k t + \theta_k)\,. \tag{B.5}$$

Thus, for some $M > 0$, we have

$$\varepsilon \leq \varepsilon + \dot{v}^2 \leq \varepsilon + \sum_{j,k=1}^{m} D_j \omega_j D_k \omega_k \leq M \sum_{j=1}^{m} D_j^2 \omega_j^2 \,, \tag{B.6}$$

where in the last step we utilized the Cauchy-Schwarz inequality. Thus, we obtain the bounds

$$\frac{\displaystyle\int_{t_0}^{t_\mathrm{f}} v\, \dot{v}^2 \mathrm{d}t}{2\sqrt{M \displaystyle\sum_{j=1}^{m} D_j^2 \omega_j^2}} \leq \hat{w} \leq \frac{\displaystyle\int_{t_0}^{t_\mathrm{f}} v\, \dot{v}^2 \mathrm{d}t}{2\sqrt{\varepsilon}} \,. \tag{B.7}$$

On the other hand,

$$\begin{aligned} v^* \dot{v}^2 =& \frac{v^*}{2} \sum_{j=1}^{m} D_j^2 \omega_j^2 - \frac{v^*}{2} \sum_{j=1}^{m} D_j^2 \omega_j^2 \cos(2\omega_j t + 2\theta_j) \\ &+ \frac{v^*}{2} \sum_{j=1}^{m} \sum_{k=1, k\neq j}^{m} D_j D_k \omega_j \omega_k \\ &\quad \times \Big[\cos\big((\omega_j + \omega_k)t + \theta_j + \theta_k\big) \\ &\qquad + \cos\big((\omega_j - \omega_k)t + \theta_j - \theta_k\big) \Big], \end{aligned} \tag{B.8}$$

and

$$\begin{aligned} \tilde{v}\, \dot{v}^2 =& \sum_{j=1}^{m} \sum_{k=1}^{m} \sum_{l=1}^{m} D_j D_k D_l \omega_j \omega_k \\ &\quad \times \cos(\omega_j t + \theta_j) \cos(\omega_k t + \theta_k) \sin(\omega_l t + \theta_l) \\ =& \frac{1}{4} \sum_{j=1}^{m} \sum_{k=1}^{m} \sum_{l=1}^{m} D_j D_k D_l \omega_j \omega_k \\ &\quad \times \Big[\sin\big((\omega_j + \omega_k + \omega_l)t + \theta_j + \theta_k + \theta_l\big) \\ &\qquad - \sin\big((\omega_j + \omega_k - \omega_l)t + \theta_j + \theta_k - \theta_l\big) \\ &\qquad + \sin\big((\omega_j - \omega_k + \omega_l)t + \theta_j - \theta_k + \theta_l\big) \\ &\qquad - \sin\big((\omega_j - \omega_k - \omega_l)t + \theta_j - \theta_k - \theta_l\big) \Big]. \end{aligned} \tag{B.9}$$

Thus, adding (B.8) and (B.9) and evaluating the integrals, we obtain

$$\begin{aligned}\int_{t_0}^{t_\mathrm{f}} v\,\dot{v}^2\mathrm{d}t &= \frac{t_\mathrm{f}-t_0}{2}v^*\sum_{j=1}^{m} D_j^2\omega_j^2 \\ &+ \frac{t_\mathrm{f}-t_0}{4}\sum_{j=1}^{m-1}\sum_{k\le m-j}^{m} D_jD_kD_{j+k}\omega_j\omega_k\sin(\theta_{j+k}-\theta_j-\theta_k) \\ &+ \frac{t_\mathrm{f}-t_0}{2}\sum_{j=1}^{m-1}\sum_{k>j}^{m} D_jD_kD_{k-j}\omega_j\omega_k\sin(\theta_j+\theta_{k-j}-\theta_k).\end{aligned} \tag{B.10}$$

Here, we assume the speed oscillations are small compared to the steady-state speed, that is, $v^* \gg D_j$ for $j = 1, \ldots, m$. Then denoting $\overline{D} = \max\{D_j | j = 1, \ldots, m\}$. Thus, we have

$$\begin{aligned}&\left|\sum_{j=1}^{m-1}\sum_{k\le m-j}^{m} D_jD_kD_{j+k}\omega_j\omega_k\sin(\theta_{j+k}-\theta_j-\theta_k)\right| \\ &\le \sum_{j=1}^{m-1}\sum_{k\le m-j}^{m} D_jD_kD_{j+k}\omega_j\omega_k < m\overline{D}\sum_{j=1}^{m}\omega_j^2D_j^2,\end{aligned} \tag{B.11}$$

and

$$\begin{aligned}&\left|\sum_{j=1}^{m-1}\sum_{k>j}^{m} D_jD_kD_{k-j}\omega_j\omega_k\sin(\theta_j+\theta_{k-j}-\theta_k)\right| \\ &\le \sum_{j=1}^{m-1}\sum_{k>j}^{m} D_jD_kD_{k-j}\omega_j\omega_k < \frac{m\overline{D}}{2}\sum_{j=1}^{m}\omega_j^2D_j^2,\end{aligned} \tag{B.12}$$

yielding

$$\begin{aligned}&\frac{(v^*-m\overline{D})(t_\mathrm{f}-t_0)}{2}\sum_{j=1}^{m} D_j^2\omega_j^2 \\ &\le \int_{t_0}^{t_\mathrm{f}} v\,\dot{v}^2\mathrm{d}t \le \\ &\frac{(v^*+m\overline{D})(t_\mathrm{f}-t_0)}{2}\sum_{j=1}^{m} D_j^2\omega_j^2.\end{aligned} \tag{B.13}$$

Finally, the energy consumption (B.4) can be bounded

$$\underline{C}\sqrt{\sum_{j=1}^{m} D_i^2\omega_j^2} \le \hat{w} \le \overline{C}\sum_{j=1}^{m} D_j^2\omega_j^2 \tag{B.14}$$

where

$$\underline{C} = \frac{(v^* - m\overline{D})(t_\mathrm{f} - t_0)}{4\sqrt{M}}, \quad \overline{C} = \frac{(v^* + m\overline{D})(t_\mathrm{f} - t_0)}{4\sqrt{\varepsilon}}. \tag{B.15}$$

Given $v^* > m\overline{D}$, the energy consumption (B.4) is bounded by class-$\mathcal{K}$ functions of $\sum_{j=1}^{m} D_j^2\omega_j^2$, which can be used for a robust energy-optimal design; see (5.22).

APPENDIX C

Receding horizon optimal control (RHOC) design

In this Appendix we provide some details about the receding horizon optimal control (RHOC) approach utilized in Section 5.3.4.

C.1 Longitudinal model

We model the longitudinal dynamics as

$$\begin{aligned} \dot{s}(t) &= v(t), \\ \dot{v}(t) &= -f\big(v(t)\big) + u(t), \end{aligned} \tag{C.1}$$

that is indeed analogous to (5.1). The dissipation $f(v)$ is still given by (5.2) but here the feedback structure of the controller u is not predetermined. Moreover, the delays are omitted as we assume that a predictor can accurately predict the current state (and even the future states) of the vehicles.

C.2 Fuel consumption map and input constraints

Fuel consumption rates are typically given as a function of the engine speed ω_{e} and engine torque T_{e}, that is, $q(\omega_{\mathrm{e}}, T_{\mathrm{e}})$. Given a well defined gear shift logic one may obtain the fuel consumption as a function of the speed v and the control input u, i.e., $q(v, u)$ [109]. Here we utilize the Willans approximation

$$q(v,u) = \begin{cases} p_2 v\, u + p_1 v + p_0, & \text{if} \quad u \geq 0, \\ p_1 v + p_0, , & \text{if} \quad u < 0, \end{cases} \tag{C.2}$$

to get analytical approximation of the fuel consumption rate [76]. In particular we have p_2=1.8284 [gs^2/m^2], p_1=0.0209 [g/m], $p_0 = -0.1868$ [g/s] for the truck.

The distinction between the two cases in (C.2) is made since for $u < 0$ the engine torque is set to zero and the brakes are applied. To bypass this nonsmoothness, we define the control inputs u_d and u_b such that

$$u = u_\mathrm{d} + u_\mathrm{b}, \tag{C.3}$$

with the constraints

$$u_\mathrm{d} \geq 0, \quad u_\mathrm{b} \leq 0, \quad u_\mathrm{d} u_\mathrm{b} = 0. \tag{C.4}$$

Indeed, u_d is related to driving torque, while u_b is related to braking torque. Then (C.2) can be rewritten as

$$q(v, u_\mathrm{d}) = p_2 v\, u_\mathrm{d} + p_1 v + p_0. \tag{C.5}$$

Due to the torque limitations of the engine and the brakes the control input u also saturates at u_min and u_max; cf. Figure 5.1(b). Here we also take into account the power limitation of the engine, i.e., we have

$$u_\mathrm{min} \leq u \leq \min \left\{ u_\mathrm{max}, \frac{P_\mathrm{max}}{m_\mathrm{eff} v} \right\}, \tag{C.6}$$

which is visualized in Figure C.1(a). Note that while in Section 5.2 the power limit was not included in the CCC design, it was still enforced by the high-fidelity simulation platform.

Finally, since RHOC algorithms are typically designed and implemented in discrete-time they may lead to "jerky" trajectories. To avoid this issue, we also pose the constraint

$$\Delta \underline{u} \leq \dot{u}_\mathrm{d} + \dot{u}_\mathrm{b} \leq \Delta \bar{u}. \tag{C.7}$$

C.3 State Constraints

Corresponding to saturation function (5.6), we set the speed constraint

$$0 \leq v \leq v_\mathrm{max}, \tag{C.8}$$

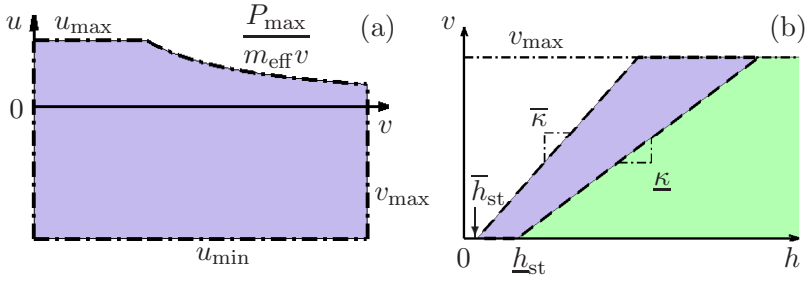

Figure C.1: (a) The working region (C.6,C.8) indicated by blue shading in the (v, u)-plane. (b) The constrained region (C.8,C.9) indicated by blue shading in (h, v)-plane. The relaxed upper bound (C.10) extends this by adding the green shading.

that is visualized in Figure C.1. Moreover, to generate a car-following behavior similar to that of the CCC controller, we introduce the state constraints

$$\overline{\kappa}\left(h - \overline{h}_{\text{st}}\right) \geq v, \quad \underline{\kappa}\left(h - \underline{h}_{\text{st}}\right) \leq v, \tag{C.9}$$

using the headway h and the speed v. The parameters are selected so that $\underline{\kappa} \leq \kappa \leq \overline{\kappa}$ and $\underline{h}_{\text{st}} \leq h_{\text{st}} \leq \overline{h}_{\text{st}}$ to make sure that the blue shaded domain shown in Figure C.1(b) includes the curve shown in Figure 5.1(c).

It can be shown that with powerful enough propulsion capability, one can have (C.9) recursively feasible for a finite horizon T. However, with limited power this may not be the case, in particular, when the acceleration capability of the preceding vehicle is larger than that of the truck. To avoid this problem we relax the upper bound in (C.9) by adding the slack variable η, that is, we set

$$\overline{\kappa}\left(h - \overline{h}_{\text{st}}\right) \geq v, \quad \underline{\kappa}\left(h - \eta - \underline{h}_{\text{st}}\right) \leq v, \tag{C.10}$$

which extend the shaded domain in Figure C.1(b) with the green part. Note that we do not relax the lower bound as that is safety critical constraint.

C.4 Implementation

Using the model and constraints listed we set up the following optimal control problem:

$$\min_{u_{\text{d}}, u_{\text{b}}} J = \mu\, \eta^2 + \int_{t_k}^{t_k+T} q(u_{\text{d}}, v)\, \mathrm{d}t, \tag{C.11}$$

subject to

$$
\begin{aligned}
&\begin{bmatrix} \dot{s} \\ \dot{v} \end{bmatrix} = \begin{bmatrix} v \\ -f(v) + u_{\mathrm{d}} + u_{\mathrm{b}} \end{bmatrix}, \\
&u_{\mathrm{d}} \geq 0, \\
&u_{\mathrm{b}} \leq 0, \\
&u_{\min} \leq u_{\mathrm{b}} + u_{\mathrm{d}} \leq \min\left\{ u_{\max}, \frac{P_{\max}}{m_{\mathrm{eff}} v} \right\}, \\
&\Delta \underline{u} \leq \dot{u}_{\mathrm{d}} + \dot{u}_{\mathrm{b}} \leq \Delta \bar{u}, \\
&0 \leq v \leq v_{\max}, \\
&\overline{\kappa} \left(h - \overline{h}_{\mathrm{st}} \right) \geq v, \\
&\underline{\kappa} \left(h - \eta - \underline{h}_{\mathrm{st}} \right) \leq v, \\
&\eta \geq 0,
\end{aligned}
\tag{C.12}
$$

and we solve this at each $t_k = k\Delta T$, $k = 0, 1, \ldots$. Here μ is the weight on slack variable, $q(u_{\mathrm{d}}, v)$ is given by (C.5) and $f(v)$ is given by (5.2). The time horizon T and the sampling period ΔT are chosen such that $T = N\Delta T$ for some $N \in \mathbb{N}$. When solving the optimal control problem the differentials are discretized using explicit Euler method with time step ΔT. Then at each t_k, the first step of the solution is applied over the interval $[t_k, t_k + \Delta T)$ using a zero-order hold, that is,

$$
u(t) = u_{\mathrm{d}}(t_k) + u_{\mathrm{b}}(t_k), \quad t \in [t_k, t_k + \Delta T). \tag{C.13}
$$

is commanded in the high-fidelity simulations

We remark that the constraint (C.7) together with fuel consumption formula (C.5) implicitly enforces the constraint $u_{\mathrm{d}} u_{\mathrm{b}} = 0$ in (C.6); see [47]. That is why $u_{\mathrm{d}} u_{\mathrm{b}} = 0$ is not listed in (C.12) reducing the complexity of the optimal control. Finally, the parameters used in the RHOC are summarized in Table C.1. Indeed, that the values of $u_{\max}$ and $u_{\min}$ are the same as in the data-based CCC design while we set $\underline{h}_{\mathrm{st}} = h_{\mathrm{st}} = \overline{h}_{\mathrm{st}}$ and $\underline{\kappa} < \kappa < \overline{\kappa}$.

μ	100 $[\mathrm{kg/m^2}]$	ΔT	0.1 [s]
$\overline{h}_{\mathrm{st}}$	5 [m]	$\underline{h}_{\mathrm{st}}$	5 [m]
$u_{\max}$	1 $[\mathrm{m/s^2}]$	$u_{\min}$	-4 $[\mathrm{m/s^2}]$
$\Delta \overline{u}$	4 $[\mathrm{m/s^3}]$	$\Delta \underline{u}$	-4 $[\mathrm{m/s^3}]$
$\underline{\kappa}$	0.4 [1/s]	$\overline{\kappa}$	1 [1/s]

Table C.1: Control parameters for RHOC design.

BIBLIOGRAPHY

[1] Navistar, "MAXXFORCE 11 and 13 LITER ENGINES," Tech. rep., Navistar Inc., 2011.

[2] U.S. Department of Transportation and U.S. Department of Commerce, "2012 Commodity Flow Survey United States," Tech. rep., 2015.

[3] Davis, S. C., Diegel, S. W., and Boundy, R. G., "Transportation energy data book: Edition 35," Tech. rep., U.S. Department of Energy, 2016.

[4] Torrey, W. and D., M., "An Analysis of the Operational Costs of Trucking: 2016 Update," Tech. rep., American Transportation Research Institute, 2016.

[5] U.S. Department of Energy, "Vehicle Technologies Office: Fact sheet on Adoption of New Fuel-Efficient Technologies from SuperTruck," June 2016.

[6] U.S. Department of Energy, "Energy Department Announces $137 Million Investment in Commercial and Passenger Vehicle Efficiency," August 2016.

[7] Saltsman, B., "Impacts of Connectivity and Automation on Vehicle Operations," Global Symposium on Connected Vehicle and Infrastructure http://umtri.umich.edu/content/2014.EnergyWS.Saltsman.pdf, 2014.

[8] Strömberg, H., Karlsson, I. C. M., and Rexfelt, O., "Eco-driving: Drivers' understanding of the concept and implications for future interventions," *Transport Policy*, Vol. 39, No. December 2007, 2015, pp. 48–54.

[9] Beusen, B., Broekx, S., Denys, T., Beckx, C., Degraeuwe, B., Gijsbers, M., Scheepers, K., Govaerts, L., Torfs, R., and Panis, L. I., "Using on-board logging devices to study the longer-term impact of an eco-driving course," *Transportation research part D: transport and environment*, Vol. 14, No. 7, 2009, pp. 514–520.

[10] Zarkadoula, M., Zoidis, G., and Tritopoulou, E., "Training urban bus drivers to promote smart driving: A note on a Greek eco-driving pilot program," *Transportation Research Part D: Transport and Environment*, Vol. 12, No. 6, 2007, pp. 449–451.

[11] Sciarretta, A., De Nunzio, G., and Ojeda, L., "Optimal Ecodriving Control: Energy-Efficient Driving of Road Vehicles as an Optimal Control Problem," *IEEE Control Systems Megazine*, Vol. 35, No. 5, Oct 2015, pp. 71–90.

[12] Gilbert, E. G., "Vehicle cruise: Improved fuel economy by periodic control," *Automatica*, Vol. 12, No. 2, mar 1976, pp. 159–166.

[13] Schwarzkopf, A. B. and Leipnik, R. B., "Control of highway vehicles for minimum fuel consumption over varying terrain," *Transportation Research*, Vol. 11, No. 4, 1977, pp. 279–286.

[14] Hellström, E., *Look-ahead Control of Heavy Vehicles*, Ph.D. thesis, Linköping University, Sweden, 2010.

[15] Fröberg, A., Hellström, E., and Nielsen, L., "Explicit fuel optimal speed profiles for heavy trucks on a set of topographic road profiles," *SAE Technical Paper*, 2006, pp. 2006–01–1071.

[16] He, C. R., Maurer, H., and Orosz, G., "Fuel Consumption Optimization of Heavy-Duty Vehicles With Grade, Wind, and Traffic Information," *Journal of Computational and Nonlinear Dynamics*, Vol. 11, No. 6, 2016, pp. 061011.

[17] Jiménez, F., López-Covarrubias, J. L., Cabrera, W., and Aparicio, F., "Real-time speed profile calculation for fuel saving considering unforeseen situations and travel time," *IET Intelligent Transport Systems*, Vol. 7, No. 1, 2013, pp. 10–19.

[18] Jiménez, F. and Cabrera-Montiel, W., "System for Road Vehicle Energy Optimization Using Real Time Road and Traffic Information," *Energies*, Vol. 7, No. 6, 2014, pp. 3576–3598.

[19] Xu, S., Li, S. E., Deng, K., Li, S., and Cheng, B., "A Unified Pseudospectral Computational Framework for Optimal Control of Road Vehicles," *IEEE/ASME Transactions on Mechatronics*, Vol. 20, No. 4, 2014, pp. 1–12.

[20] Kamal, M. A. S., Mukai, M., Murata, J., and Kawabe, T., "Ecological vehicle control on roads with up-down slopes," *IEEE Transactions on Intelligent Transportation Systems*, Vol. 12, No. 3, 2011, pp. 783–794.

[21] Ozatay, E., Onori, S., Wollaeger, J., Ozguner, U., Rizzoni, G., Filev, D., Michelini, J., and Di Cairano, S., "Cloud-Based Velocity Profile Optimization for Everyday Driving: A Dynamic-Programming-Based Solution," *IEEE Transactions on Intelligent Transportation Systems*, Vol. 15, No. 6, 2014, pp. 1–15.

[22] McDonough, K. K., *Developments in Stochastic Fuel Efficient Cruise Control and Constrained Control with Applications to Aircraft*, Ph.D. thesis, University of Michigan, 2015.

[23] Cheng, X., Yang, L., and Shen, X., "D2D for Intelligent Transportation Systems: A Feasibility Study," *IEEE Transactions on Intelligent Transportation Systems*, Vol. 16, No. 4, Aug 2015, pp. 1784–1793.

[24] Peng, H., "Connected and Automated Vehicles: The Roles Of Dynamics And Control," *Mechanical Engineering*, Vol. 138, No. 12, 2016, pp. S4.

[25] Caveney, D., "Cooperative vehicular safety applications," *IEEE Control Systems Magazine*, Vol. 30, No. 4, 2010, pp. 38–53.

[26] "Dedicated Short Range Communications (DSRC) Service," https://www.fcc.gov/wireless/bureau-divisions/mobility-division/dedicated-short-range-communications-dsrc-service, 2016.

[27] "IEEE802.11p ahead of LTE-V2V for safety applications," https://www.auto-talks.com/wp-content/uploads/2017/09/Whitepaper-LTE-V2V-USletter-05.pdf, 2018.

[28] Shah, S. A. A., Ahmed, E., Imran, M., and Zeadally, S., "5G for Vehicular Communications," *IEEE Communications Magazine*, Vol. 56, No. 1, Jan 2018, pp. 111–117.

[29] "Commsignia," http://www.commsignia.com, 2018.

[30] Ploeg, J., Shladover, S., Nijmeijer, H., and van de Wouw, N., "Introduction to the Special Issue on the 2011 Grand Cooperative Driving Challenge," *IEEE Transactions on Intelligent Transportation Systems*, Vol. 13, No. 3, 2012, pp. 989–993.

[31] Wang, M., Daamen, W., Hoogendoorn, S. P., and van Arem, B., "Rolling horizon control framework for driver assistance systems. Part I: Mathematical formulation and non-cooperative systems," *Transportation Research Part C*, Vol. 40, 2014, pp. 271–289.

[32] Wang, M., Daamen, W., Hoogendoorn, S. P., and van Arem, B., "Rolling horizon control framework for driver assistance systems. Part II: Cooperative sensing and cooperative control," *Transportation Research Part C*, Vol. 40, 2014, pp. 290–311.

[33] Lu, X.-Y. and Shladover, S., "Integrated ACC and CACC development for Heavy-Duty Truck partial automation," *Proceeding of 2017 American Control Conference*, May 2017, pp. 4938–4945.

[34] Englund, C., Chen, L., Ploeg, J., Semsar-Kazerooni, E., Voronov, A., Bengtsson, H. H., and Didoff, J., "The Grand Cooperative Driving Challenge 2016: boosting the introduction of cooperative automated vehicles," *IEEE Wireless Communications*, Vol. 23, No. 4, August 2016, pp. 146–152.

[35] Alam, A., *Fuel-Efficient Heavy Duty Vehicle Platooning*, Ph.D. thesis, Kungliga Tekniska Högskolan, 2014.

[36] Turri, V., Besselink, B., and Johansson, K. H., "Cooperative Look-Ahead Control for Fuel-Efficient and Safe Heavy-Duty Vehicle Platooning," *IEEE Transactions on Control Systems Technology*, Vol. 25, No. 1, 2017, pp. 12–28.

[37] Rajeswaran, A., Lowrey, K., Todorov, E. V., and Kakade, S. M., "Towards generalization and simplicity in continuous control," *Advances in Neural Information Processing Systems 30*, edited by I. Guyon, U. V. Luxburg, S. Bengio, H. Wallach, R. Fergus, S. Vishwanathan, and R. Garnett, Curran Associates, Inc., 2017, pp. 6550–6561.

[38] Kohut, N., Hedrick, K., and Borrelli, F., "Integrating traffic data and model predictive control to improve fuel economy," *12th IFAC Symposium on Control in Transportation Systems*, 2009, pp. 155–160.

[39] Kamal, M. S., Mukai, M., Murata, J., and Kawabe, T., "Model predictive control of vehicles on urban roads for improved fuel economy," *IEEE Transactions on Control Systems Technology*, Vol. 21, No. 3, 2013, pp. 831–841.

[40] Li, S. E., Jia, Z., Li, K., and Cheng, B., "Fast Online Computation of a Model Predictive Controller and Its Application to Fuel Economy–Oriented Adaptive Cruise Control," *IEEE Transactions on Intelligent Transportation Systems*, Vol. 16, No. 3, 2015, pp. 1199–1209.

[41] Jing, J., Özatay, E., Kurt, A., Michelini, J., Dimitre, P. F., and Özgüner, Ü., "Design of a Fuel Economy Oriented Vehicle Longitudinal Speed Controller with Optimal Gear Sequence," *Proceedings of the IEEE Conference on Decision and Control*, 2016, pp. 1595–1601.

[42] Li, S. E., Guo, Q., Xu, S., Duan, J., Li, S., Li, C., and Su, K., "Performance Enhanced Predictive Control for Adaptive Cruise Control System Considering Road Elevation Information," *IEEE Transactions on Intelligent Vehicles*, Vol. 2, No. 3, 2017, pp. 150–160.

[43] Sun, C., Hu, X., Moura, S. J., and Sun, F., "Velocity predictors for predictive energy management in hybrid electric vehicles," *IEEE Transactions on Control Systems Technology*, Vol. 23, No. 3, 2015, pp. 1197–1204.

[44] Orosz, G., "Connected cruise control: modelling, delay effects, and nonlinear behaviour," *Vehicle System Dynamics*, Vol. 54, No. 8, 2016, pp. 1147–1176.

[45] Ge, J. I. and Orosz, G., "Connected cruise control among human-driver vehicles: experiment based parameter estimation and optimal control design," *Transportation Research Part C*, Vol. 91, 2018, pp. 445–459.

[46] Ge, J. I., Avedisov, S. S., He, C. R., Qin, W. B., Sadeghpour, M., and Orosz, G., "Experimental validation of connected automated vehicle design among human-driven vehicles impacts on traffic safety and effciency," *Transportation Research Part C*, Vol. 91, 2018, pp. 335–352.

[47] He, C. R. and Orosz, G., "Saving fuel using wireless vehicle-to-vehicle communication," *Proceedings of the American Control Conference*, 2017, pp. 4946–4951.

[48] Li, N. I., He, C. R., and Orosz, G., "Sequential Parametric Optimization For Connected Cruise Control With Application to Fuel Economy Optimization," *55rd IEEE Conference on Decision and Control*, 2016, pp. 227–232.

[49] He, C. R., Ge, J. I., and Orosz, G., "Data-based fuel-economy optimization of connected automated trucks in traffic," *Proceeding of American Control Conference*, 2018, pp. 5576–5581.

[50] Ulsoy, A. G., Peng, H., and Çakmakci, M., *Automotive Control Systems*, Cambridge University Press, 2012.

[51] Heywood, J. B., *Internal combustion engine fundamentals*, McGraw-Hill, New Y-ork, 2002.

[52] Zhang, L., Sun, J., and Orosz, G., "Hierarchical design of connected cruise control in the presence of information delays and uncertain vehicle dynamics," *IEEE Transactions on Control System Technology*, , No. 26, 2018, pp. 139–150.

[53] Bai, S., Maguire, J., and Peng, H., *Dynamic Analysis and Control System Design of Automatic Transmissions*, SAE International, 2013.

[54] Kim, D., Peng, H., Bai, S., and Maguire, J. M., "Control of integrated powertrain with electronic throttle and automatic transmission," *IEEE Transactions on Control Systems Technology*, Vol. 15, No. 3, 2007, pp. 474–482.

[55] Ngo, V. D., Navarrete, J. A. C., Hofman, T., Steinbuch, M., and Serrarens, A., "Optimal gear shift strategies for fuel economy and driveability," *Proceedings of the Institution of Mechanical Engineers, Part D*, Vol. 277, 2013, pp. 1398–1413.

[56] Fofana, A., Haas, O., Ersanilli, V., Burnham, K., Mahtani, J., Woolley, C., and Vithanage, K., "Multi-Objective Genetic Algorithm for an automatic transmission gear shift map," *IFAC-PapersOnLine*, Vol. 49, 2016.

[57] Qin, G., Ge, A., and Lee, J.-J., "Knowledge-based gear-position decision," *IEEE Transactions on Intelligent Transportation Systems*, Vol. 5, No. 2, 2004, pp. 121–125.

[58] Tan, J., Yin, X., Lei, Y., and Ge, A., "Research on a Neural Network Model Based Automatic Shift Schedule with Dynamic 3-Parameters," *SAE Technical Paper*, SAE International, 04 2005.

[59] Li, G. and Hu, J., "Modeling and analysis of shift schedule for automatic transmission vehicle based on fuzzy neural network," *8th World Congress on Intelligent Control and Automation (WCICA)*, IEEE, 2010, pp. 4839–4844.

[60] Liu, Y. G., Qin, D. T., Lei, Z. Z., and Ding, R., "Intelligent Correction of Shift Schedule for Dual Clutch Transmissions Based on Different Driving Conditions," *Applied Mechanics and Materials*, Vol. 121-126, 2011, pp. 3982–3987.

[61] Lin, H. and Antsaklis, P. J., "Stability and stabilizability of switched linear systems: a survey of recent results," *IEEE Transactions on Automatic control*, Vol. 54, No. 2, 2009, pp. 308–322.

[62] Branicky, M. S., "Multiple Lyapunov functions and other analysis tools for switched and hybrid systems," *IEEE Transactions on Automatic Control*, Vol. 43, No. 4, 1998, pp. 475–482.

[63] Bernardo, M., Budd, C., Champneys, A. R., and Kowalczyk, P., *Piecewise-smooth dynamical systems: theory and applications*, Vol. 163 of *Applied Mathematical Sciences*, Springer, 2008.

[64] Liu, J., Liu, X., and Xie, W.-C., "On the $(h_0\,, h)$-stabilization of switched nonlinear systems via state-dependent switching rule," *Applied Mathematics and Computation*, Vol. 217, No. 5, 2010, pp. 2067–2083.

[65] Jin, Y., Fu, J., Zhang, Y., and Jing, Y., "Reliable control of a class of switched cascade nonlinear systems with its application to flight control," *Nonlinear Analysis: Hybrid Systems*, Vol. 11, 2014, pp. 11–21.

[66] Liu, J., Ozay, N., Topcu, U., and Murray, R. M., "Synthesis of reactive switching protocols from temporal logic specifications," *IEEE Transactions on Automatic Control*, Vol. 58, No. 7, 2013, pp. 1771–1785.

[67] Aström, K. J. and Murray, R. M., *Feedback systems: an introduction for scientists and engineers*, Princeton University Press, 2010.

[68] Hartl, R. F., Sethi, S. P., and Vickson, R. G., "A survey of the maximum principles for optimal control problems with state constraints," *SIAM Review*, Vol. 37, No. 2, 1995, pp. 181–218.

[69] Vinter, R., *Optimal Control (Systems & Control: Foundations & Applications)*, Springer Science & Business Media, 2000.

[70] Clarke, F. and De Pinho, M., "Optimal control problems with mixed constraints," *SIAM Journal on Control and Optimization*, Vol. 48, No. 7, 2010, pp. 4500–4524.

[71] Maurer, H., Büskens, C., Kim, J.-H., and Kaya, Y., "Optimization methods for the verification of second order sufficient conditions for bang-bang controls," *Optimal Control Methods and Applications*, Vol. 26, 2005, pp. 129–156.

[72] Maurer, H. and Pickenhain, S., "Second-order sufficient conditions for control problems with mixed control-state constraints," *Journal of Optimization Theory and Applications*, Vol. 86, No. 3, 1995, pp. 649–667.

[73] Graichen, K. and Petit, N., "Constructive methods for initialization and handling mixed state-input constraints in optimal control," *Journal of Guidance, Control, and Dynamics*, Vol. 31, No. 5, 2008, pp. 1334–1343.

[74] Wyczalkowski, M. and Szeri, A. J., "Optimization of acoustic scattering from dual-frequency driven microbubbles at the difference frequency," *The Journal of the Acoustical Society of America*, Vol. 113, No. 6, 2003, pp. 3073–3079.

[75] Ozatay, E., Özgüner, Ü., Onori, S., and Rizzoni, G., "Analytical Solution to the Minimum Fuel Consumption Optimization Problem with the Existence of a Traffic Light," *5th Annual Dynamic Systems and Control Conference and 11th Motion and Vibration Conference*, 2012, pp. 837–846.

[76] Guzzella, L. and Onder, C. H., *Introduction to Modelling and Control of Internal Combustion Engine Systems*, Springer, 2004.

[77] Osmolovskii, N. and Maurer, H., *Applications to regular and bang-bang control, Second-Order Necessary and Sufficient Optimality Conditions in Calculus of Variations and Optimal Control*, Vol. DC 24, SIAM Publications, Philadelphia, 2012.

[78] Orosz, G., Wilson, R. E., and Stépán, G., "Traffic jams: dynamics and control," *Philosophical Transactions of the Royal Society of London A: Mathematical, Physical and Engineering Sciences*, Vol. 368, No. 1928, 2010, pp. 4455–4479.

[79] Hestenes, M. R., *Calculus of Variations and Optimal Control Theory*, John Wiley, 1966.

[80] Krener, A. J., "The high order maximal principle and its application to singular extremals," *SIAM Journal on Control and Optimization*, Vol. 15, No. 2, 1977, pp. 256–293.

[81] Stoer, J., Bulirsch, R., Bartels, R., Gautschi, W., and Witzgall, C., *Introduction to Numerical Analysis*, Vol. 2, Springer, 1993.

[82] Wächter, A. and Biegler, L. T., "On the implementation of an interior-point filter line-search algorithm for large-scale nonlinear programming," *Mathematical Programming*, Vol. 106, No. 1, 2006, pp. 25–57.

[83] Gay, D. M. and Kernighan, B., "AMPL: A Modeling Language for Mathematical Programming," *Duxbury Press/Brooks/Cole*, Vol. 2, 2002.

[84] Allgower, E. E. L. and Georg, K., *Introduction to Numerical Continuation Methods*, Vol. 45 of *Classics in Applied Mathematics*, SIAM, 2003.

[85] Rao, A. V., "A survey of numerical methods for optimal control," *Advances in the Astronautical Sciences*, Vol. 135, No. 1, 2009, pp. 497–528.

[86] He, C. R. and Orosz, G., "Fuel Consumption Optimization of Heavy-Duty Vehicles: An Analytical Approach," *Proceedings of the ASME Dynamic Systems and Control Conference*, No. DSCC2014-6362, 2014, p. V002T20A006.

[87] He, C. R., Maurer, H., and Orosz, G., "Fuel Consumption Optimization of Heavy-Duty Vehicles With Grade, Wind, and Traffic Information," *Journal of Computational and Nonlinear Dynamics*, Vol. 11, No. 6, 2016, pp. 061011.

[88] Wang, M., Daamen, W., Hoogendoorn, S. P., and van Arem, B., "Cooperative car-following control: Distributed algorithm and impact on moving jam features," *IEEE Transactions on Intelligent Transportation Systems*, Vol. 17, No. 5, 2016, pp. 1459–1471.

[89] Dey, K. C., Yan, L., Wang, X., Wang, Y., Shen, H., Chowdhury, M., Yu, L., Qiu, C., and Soundararaj, V., "A review of communication, driver characteristics, and controls aspects of cooperative adaptive cruise control (CACC)," *IEEE Transactions on Intelligent Transportation Systems*, Vol. 17, No. 2, 2016, pp. 491–509.

[90] Turri, V., Besselink, B., and Johansson, K. H., "Cooperative look-ahead control for fuel-efficient and safe heavy-duty vehicle platooning," *IEEE Transactions on Control Systems Technology*, Vol. 25, No. 1, 2017, pp. 12–28.

[91] Shladover, S. E., Nowakowski, C., Lu, X.-Y., and Ferlis, R., "Cooperative Adaptive Cruise Control Definitions and Operating Concepts," *Transportation Research Record: Journal of the Transportation Research Board*, Vol. 2489, 2015, pp. 145–152.

[92] Asadi, B. and Vahidi, A., "Predictive cruise control: Utilizing upcoming traffic signal information for improving fuel economy and reducing trip time," *IEEE Transactions on Control Systems Technology*, Vol. 19, No. 3, 2011, pp. 707–714.

[93] Lefèvre, S., Carvalho, A., and Borrelli, F., "A learning-based freamework for velocity control in autonomous driving," *IEEE Transactions on Automation Science and Engineering*, Vol. 13, No. 1, 2016, pp. 32–42.

[94] Shao, Y. and Sun, Z., "Robust eco-cooperative adaptive cruise control with gear shifting," *Proceedings of the American Control Conference*, 2017, pp. 4958–4963.

[95] Ge, J. I. and Orosz, G., "Optimal Control of Connected Vehicle Systems With Communication Delay and Driver Reaction Time," *IEEE Transactions on Intelligent Transportation Systems*, Vol. 18, No. 8, 2017, pp. 2056–2070.

[96] Zhang, L. and Orosz, G., "Motif-based design for forward-looking delayed networks with applications to connected vehicle systems," *IEEE Transactions on Intelligent Transportation Systems*, Vol. 17, No. 6, 2016, pp. 1638–1651.

[97] Wächter, A. and Biegler, L. T., "On the implementation of an interior-point filter line-search algorithm for large-scale nonlinear programming," *Mathematical Programming*, Vol. 106, No. 1, 2006, pp. 25–57.

[98] Jing, J., Filev, D., Kurt, A., Özatay, E., Michelini, J., and Özgüner, Ü., "Vehicle speed prediction using a cooperative method of fuzzy Markov model and auto-regressive model," *Proceedings of the IEEE Intelligent Vehicles Symposium*, 2017, pp. 881–886.

[99] Zhang, L. and Orosz, G., "Consensus and disturbance attenuation in multi-agent chains with nonlinear control and time delays (published online)," *International Journal of Robust and Nonlinear Control*, Vol. 27, No. 5, 2017, pp. 781–803.

[100] Mareczek, J., Buss, M., and Spong, M. W., "Invariance control for a class of cascade nonlinear systems," *IEEE Transactions on Automatic Control*, Vol. 47, No. 4, 2002, pp. 636–640.

[101] Garone, E., Di Cairano, S., and Kolmanovsky, I., "Reference and command governors for systems with constraints: A survey on theory and applications," *Automatica*, , No. 75, 2017, pp. 306–328.

[102] Ames, A. D., Xu, X., Grizzle, J. W., and Tabuada, P., "Control barrier function based quadratic programs for safety critical systems," *IEEE Transactions on Automatic Control*, Vol. 62, No. 8, 2017, pp. 3861–3876.

[103] Xu, X., Grizzle, J. W., Tabuada, P., and Ames, A. D., "Correctness guarantees for the composition of lane keeping and adaptive cruise control," *IEEE Transactions on Automation Science and Engineering*, 2017, pp. published online.

[104] Ge, J. I. and Orosz, G., "Dynamics of connected vehicle systems with delayed acceleration feedback," *Transportation Research Part C, Emerging Technologies*, Vol. 46, 2014, pp. 46–64.

[105] Sepulchre, R., Jankovic, M., and Kokotovic, P. V., *Constructive nonlinear control*, Springer Science & Business Media, 1997.

[106] Roose, D. and Szalai, R., "Continuation and bifurcation analysis of delay differential equations," *Numerical Continuation Methods for Dynamical Systems*, edited by B. Krauskopf, H. Osinga, and J. Galán-Vioque, Springer, 2007, pp. 359–399.

[107] Mittelmann, H. D., "A pseudo-arclength continuation method for nonlinear eigenvalue problems," *SIAM Journal on Numerical Analysis*, Vol. 23, No. 5, 1986, pp. 1007–1016.

[108] Jorge, N. and Wright, S. J., *Numerical optimization*, Vol. 2 of *Operations Research and Financial Engineering*, Springer, 1999.

[109] He, C. R., Qin, W. B., Ozay, N., and Orosz, G., "Optimal Gear Shift Schedule Design for Autonomous Vehicles: Hybrid System Based Analytical Approach," *IEEE Transactions on Control Systems Technology*, Vol. 26, 2018, pp. 2078 – 2090.